![KIT logo – Karlsruhe Institute of Technology]

Patrick Müller

Molecular Photoswitches for STED-inspired Laser Lithography

Molecular Photoswitches for STED-inspired Laser Lithography

Zur Erlangung des akademischen Grades eines

Doktors der Naturwissenschaften

von der Fakultät für Physik des
Karlsruher Instituts für Technologie (KIT)

genehmigte

Dissertation

von

Patrick Müller, M. Sc.
geboren in Oberkirch

Tag der mündlichen Prüfung: 18.01.2019
Referent: Prof. Dr. Martin Wegener
Korreferent: PD Dr. Andreas-Neil Unterreiner

Contents

Publications

Scientific Journals

Parts of this thesis have already been published in scientific journals:

- P. Mueller, M. M. Zieger, B. Richter, A. S. Quick, J. Fischer, J. B. Mueller, L. Zhou, G. U. Nienhaus, M. Bastmeyer, C. Barner-Kowollik, and M. Wegener, "Molecular Switch for Sub-Diffraction Laser Lithography by Photoenol Intermediate-State Cis–Trans Isomerization", *ACS Nano* **11**, 6396–6403 (2017)

- P. Müller, R. Müller, L. Hammer, C. Barner-Kowollik, M. Wegener, and E. Blasco, "STED-Inspired Laser Lithography Based on Photoswitchable Spirothiopyran Moieties", *Chem. Mater.* (2018)
  DOI: 10.1021/acs.chemmater.8b04696

Conference Presentations

Parts of this thesis have been presented at scientific conferences (only own presentations):

- P. Mueller, B. Richter, A. S. Quick, J. Fischer, J. B. Mueller, L. Zhou, G. U. Nienhaus, M. Bastmeyer, C. Barner-Kowollik, and M. Wegener, "Photoenol Laser Lithography Using Intermediate-State Cis-Trans Isomerization for Writing Inhibition", CLEO 2016, San José, CA, USA, June 2016

- P. Mueller, L. Hammer, R. Mueller, E. Blasco, C. Barner-Kowollik, and M. Wegener, "STED-inspired Laser Lithography Based on Spirothiopyran Chromophores", CLEO 2018, San José, CA, USA, May 2018

ADDITIONAL PUBLICATIONS

Additional related work has already been published or presented:

- P. Mueller, M. Thiel, and M. Wegener, "3D Direct Laser Writing Using a 405 nm Diode Laser", *Opt. Lett.* **39**, 6847–6850 (2014)

- P. Mueller, M. Thiel, and M. Wegener, "3D Direct Laser Writing Using a 405 nm Diode Laser", SPIE Photonics West, San Francisco, CA, USA, February 2015

- M. Kaupp, K. Hiltebrandt, V. Trouillet, P. Mueller, A. S. Quick, M. Wegener, and C. Barner-Kowollik, "Wavelength selective polymer network formation of end-functional star polymers", *Chem. Comm.* **52**, 1975–1978 (2016)

- L. Fruk, A. Kerbs, P. Mueller, M. Kaupp, I. Ahmed, A. S. Quick, D. Abt, M. Wegener, C. M. Niemeyer, and C. Barner-Kowollik, "Photo-Induced Click Chemistry for DNA Surface Structuring via Direct Laser Writing", *Chem. Eur. J.* **23**, 4990–4994 (2017)

- M. M. Zieger, P. Mueller, A. S. Quick, M. Wegener, and C. Barner-Kowollik, "Cleaving Direct-Laser-Written Microstructures on Demand", *Angew. Chem. Int. Ed.* **56**, 5625–5629 (2017)

- C. Barner-Kowollik, M. Bastmeyer, E. Blasco, G. Delaittre, P. Müller, B. Richter, and M. Wegener, "3D Laser Micro- and Nanoprinting: Challenges for Chemistry", *Angew. Chem. Int. Ed.* **56**, 15828–15845 (2017)

- M. M. Zieger, P. Müller, E. Blasco, C. Petit, V. Hahn, L. Michalek, H. Mutlu, M. Wegener, and C. Barner-Kowollik, "A Subtractive Photoresist Platform for Micro- and Macroscopic 3D Printed Structures", *Adv. Funct. Mater.* **28**, 1801405 (2018)

Abbreviations

1/2/3D	one/two/three-dimensional
AFM	atomic force microscopy
AMOL	absorbance-modulation optical lithography
AOM	acousto-optic modulator
APD	avalanche photodiode
cw	continuous-wave
DETC	7-diethylamino-3-thenoylcoumarin
DLW	direct laser writing (*i. e.* 3D laser lithography)
DMF	dimethylformamide
DMSO	dimethylsulfoxide
ESA	excited-state absorption
FWHM	full width at half maximum
ISC	intersystem crossing
ITX	isopropyl thioxanthone
LED	light-emitting diode
MC	merocyanine
MGCB	malachite green carbinol base
NA	numerical aperture
NMR	nuclear magnetic resonance
***o*-MBA**	*ortho*-methylbenzaldehyde
PAG	photoacid generator
PDMS	polydimethylsiloxane
PEGMEMA	poly(ethylene glycol) methyl ether methacrylate
SEM	scanning electron microscopy
SI-ATRP	surface-initiated atom transfer radical polymerization
SP	spiropyran
STED	stimulated-emission depletion
STP	spirothiopyran
UV	ultraviolet

1 Chapter 1
INTRODUCTION

On May 16, 2018, the UNESCO celebrated the first International Day of Light to raise awareness of the importance of light science and technology and their impact on the global society. Although the human being is equipped with a natural light sensor, it is not easy for us to perceive the extent to which light-based technologies have penetrated so many aspects of our lives and have led to countless advances in medicine, communications, energy, and culture.

Sparked by the invention of the laser in the 1960s, light has also been employed for processing of materials in an ever growing field of applications. Today, laser are used for welding, cutting, drilling, and surface treatment and have become important tools for industrial manufacturing. Moreover, the advent of 3D printing using lasers might totally change the way we think about materials processing in the future.

As laser beams can be focused very tightly, laser-based processing techniques are often used for tasks that require very high precision. The perhaps most impressive example for that is the progress of the semiconductor industry. For decades, constantly improving the technology of optical lithography has been enabling cost-effective mass production of high-precision microelectronic devices with ever smaller structure sizes. Following the famous law of Gordon Moore [1], fabrication of microchips by optical lithography has fueled the development of computers and information technology.

For many scientific applications, however, planar lithography techniques are not sufficient anymore. Instead, recent advances in nanotechnology require the possibility to create three-dimensional (3D) structures on the micro- and nanoscale. 3D laser lithography, also known as Direct Laser

Writing, has proved to meet that demand [2, 3]. In this technique, a tightly focused laser beam is scanned through a transparent photoresist, inducing a cross-linking reaction confined to the focal volume. In that way, almost arbitrary structures can be 3D printed with feature sizes and resolutions in the sub-micrometer range. Since its invention about 20 years ago, the technique has been improved and extended, and has found numerous applications across many fields in science.

However, light cannot be focused to an *arbitrarily* small spot. Instead, being a consequence of the wave nature of light, attainable feature sizes and resolutions are fundamentally limited by diffraction. Not only lithography, but all optical techniques are subject to this so-called diffraction limit that was first formulated with regard to optical microscopy by Ernst Abbe in 1873 [4]. Only recently, this limitation could be overcome by using concepts of modern physics. Stimulated-emission depletion (STED) microscopy extends regular confocal microscopy by introducing a second laser beam with a special focus shape that deactivates a portion of the excited fluorophores and thereby confines fluorescence to a smaller volume [5]. By increasing the power of the deactivation laser, the size of this volume can in principle be reduced as needed. The inventor of this technique, Stefan Hell, was awarded with the Nobel Prize for Chemistry in 2014.

The STED concept has also been transferred to optical lithography, in particular to 3D laser lithography [6]. Therefore, the wavelength of light does not impose a fundamental limit anymore, but ultimately only the size of the molecules in the photoresist. In practice, however, the implementation of a STED-inspired scheme is a considerable materials challenge. The photoresist material has to fulfill several criteria. The most important one is that the cross-linking reaction induced by one wavelength of light can be suppressed by a second (different) wavelength. In other words, the reactivity of the material has to be switchable by light.

The aim of this thesis is the investigation of two novel *molecular photo-switches* suitable for STED-inspired laser lithography. The first photoswitch is based on intermediate-state photoenols generated from methylbenzaldehydes. The second one is based on the photochromic compound spirothiopyran. In both cases, the switching behavior is provided by photoisomerization processes.

Outline of This Thesis

In Chapter 2, I describe the fundamentals of 3D laser lithography necessary for understanding the ensuing discussions. I discuss the requirements that an adoption of the STED concept sets onto photoresist materials and review previous approaches found in literature. Chapter 3 covers the experimental methods used throughout this thesis, such as the lithography setup and the sample preparation workflows. In Chapter 4, I present the molecular photoswitch based on intermediate-state photoenols. The underlying chemistry, experiments on sub-diffraction surface functionalization, and approaches towards a photoresist capable of 3D structuring are described. In Chapter 5, the molecular photoswitch based on spirothiopyran is introduced. After reviewing the chemistry, I describe experiments on surface-functionalization. Moreover, I present a photoresist that supports 3D structures and allows for enhanced feature sizes and resolution by employing depletion. After describing the two photoswitches individually, they are compared in Chapter 6. I describe differences and common limitations and point out ways for future improvements. Furthermore, I address future related fields of research. Finally, I summarize and conclude my thesis in Chapter 7.

2

FUNDAMENTALS
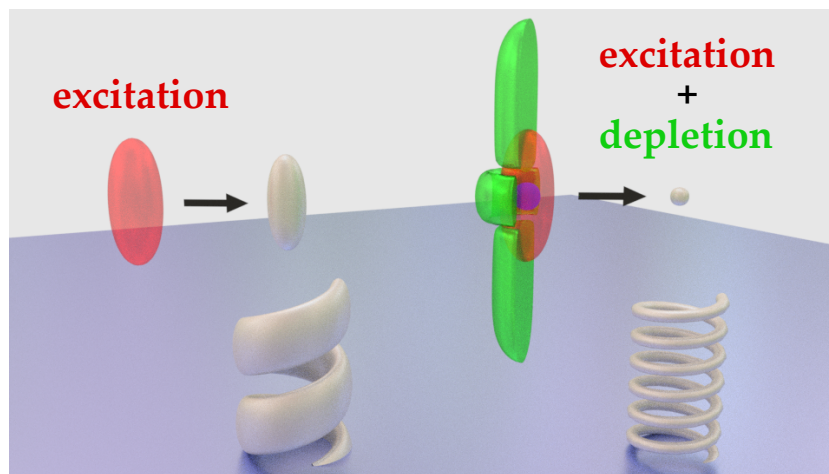
An artist's impression of the resolution increase achieved using STED-inspired direct laser writing.

In this chapter, I give an introduction to 3D laser lithography and highlight a few common aspects of typically employed photoresists. The resolution criteria and limitations on resolution by optical diffraction are explained. The principle of STED microscopy is presented that allows to overcome these limitations. I show that this principle can be transferred to laser lithography and thereby introduce the concept of a molecular photoswitch. Finally, several previous approaches towards implementing a STED-inspired scheme for lithography are reviewed.

2.1 3D LASER LITHOGRAPHY

3D laser lithography, also known as *Direct Laser Writing* (DLW)[1] or two-photon polymerization, is a versatile technique that allows fabrication of almost arbitrary 2D and 3D structures, realizing 3D printing on the micro- and nanoscale [2, 3]. A laser beam is tightly focused into a photosensitive material, the photoresist, where a physical or chemical reaction takes place in the center of the laser focus, locally altering the solubility of the material. The laser focus thereby acts as a "writing tip". By moving the laser beam relatively to the sample, arbitrary 3D structures can be written in a serial manner. In case of negative-tone photoresists, the exposed parts are solidified, typically by a network-forming chemical reaction. The unexposed parts of the photoresist are removed in a development step (Figure 2.1). The elementary writing volume obtained by a single point exposure is called voxel. For positive-tone photoresists, the laser light induces a solubility increase such that the exposed parts are dissolved during development and the unexposed parts remain.

In contrast to industrial UV lithography, DLW is a very flexible maskless technology as the patterns are defined only by software. Thus, it is very suitable for prototyping or individual fabrication with changing designs, where high throughput is not a crucial requirement. While 2D laser writing systems based on continuous-wave UV lasers had already been commercialized in the 1980s, 3D laser lithography was invented in the late 1990s [7] with the advent of cost-efficient commercial femtosecond-pulsed laser sources. Using such ultrashort laser pulses is key for stepping from 2D to 3D structuring as their high peak intensities allow excitation of the photoresists by two- or multi-photon absorption. As I show below, such a nonlinear process is necessary to allow for true 3D fabrication.

Typically, femtosecond-pulsed laser sources such as tunable titanium-sapphire oscillators or frequency-doubled erbium-doped fiber lasers are used, emitting near-infrared pulses with pulse lengths around 100–150 fs. The requirement of femtosecond pulses can be lifted for certain combinations of materials and wavelengths, such that pico- or nanosecond-pulsed laser

---

[1] Throughout this thesis, I use the terms 3D laser lithography and DLW synonymously.
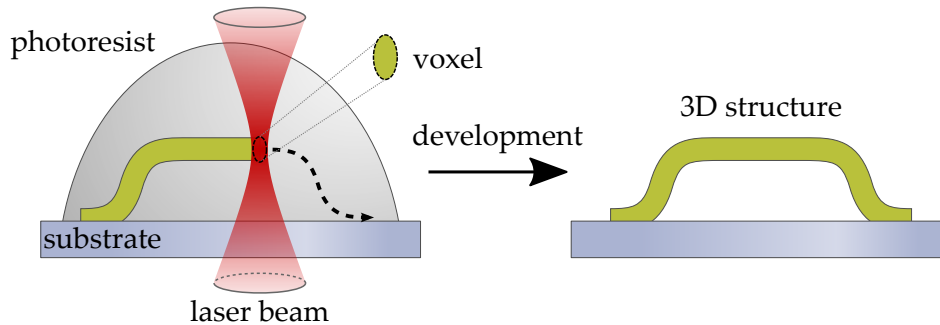
Figure 2.1: The principle of Direct Laser Writing. A focused laser beam is scanned through a liquid negative-tone photoresist, solidifying the material by multi-photon-induced cross-linking at the coordinates of the desired structure. The unexposed resist is removed during development, while the written 3D structure remains. The elementary writing volume is called voxel.

sources or even continuous-wave (cw) lasers have been employed for DLW (see Section 2.1.2) [8–13]. Objective lenses with high numerical apertures, often oil-immersion lenses, are used to achieve tight focusing conditions. Constraints to maximum structure height given by the oil-immersion setup can be lifted by dip-in DLW, where the objective lens is dipped into the photoresist which thereby also serves as immersion medium [14]. For beam scanning, piezo-actuated stages offer high precision at the cost of low speeds limited to the range of $100\,\mu m\,s^{-1}$. The use of beam scanners based on galvanometric mirrors enabled in-plane fabrication speeds up to meters per second [15]. Throughput is still low compared to other techniques because the small exposed volume requires many passes of the laser beam to fill a considerable area. A further increase in speed can be achieved by parallelized writing using multiple laser foci generated by microlens arrays [16] or by spatial light modulators [15, 17].

In the last two decades, DLW has developed from a lab curiosity into an established fabrication method that has been commercialized by several companies. While most users of this technique are still found in science and research, applications in industry are in reach [18].

2.1.1 MATERIALS AND APPLICATIONS

The most common workhorse materials are negative-tone photoresists based on multifunctional acrylate monomers containing a small amount of photoinitiator. Upon multi-photon excitation, the initiator molecules decay into radicals that initiate free-radical polymerization leading to formation of a polymer network. The employed photoinitiators are usually sensitive to UV light at wavelengths of 400 nm or below and were originally developed for UV curing of resists for conventional g-line or i-line photolithography. It is not guaranteed that the one-photon absorption spectra of such initiators can be translated to two-photon absorption just by multiplying the wavelength by two, however in practice, their π-conjugated systems can be efficiently excited by multi-photon absorption at near-infrared wavelengths [19]. Recently, studies have been performed on tailoring photoinitiator molecules to yield higher two-photon cross sections, in part sparked by parallel efforts in the development of dyes for two-photon microscopy [20, 21]. An increased sensitivity reduces the exposure dose required for polymerization, thus enabling higher writing speeds [22].

DLW has found a multitude of applications in various different fields, a few of which I describe in the following. In the field of nanophotonics, three-dimensional photonic crystals [27, 28], chiral materials [29, 30], or optical metamaterials [31] have been realized. To achieve high refractive indices at optical wavelengths, polymer structures can be coated by [32, 33], or inverted into semiconductors or metals [34, 35]. DLW has been employed for fabrication of microoptical elements [36] and allows to write complex optical systems onto the tips of optical fibers [23]. Here, the high degree of freedom in the structural design facilitates fabrication of microscale free-form optical elements for imaging (Figure 2.2 a)) [37], light-guiding applications [38, 39], or photonic wirebonding for optical interconnects (Figure 2.2 b)) [24]. Hybrid inorganic-organic photoresists such as Ormocomp (micro resist technology) or SZ2080 (FORTH) provide almost glass-like optical properties [40, 41]. To lift the restriction of low throughput, direct-laser-written structures have been employed as masters for molding replication processes [42]. Apart from optical applications, the possibility of 3D printing almost arbitrary structures opened up many new fields. Metamaterials with tailored mechan-
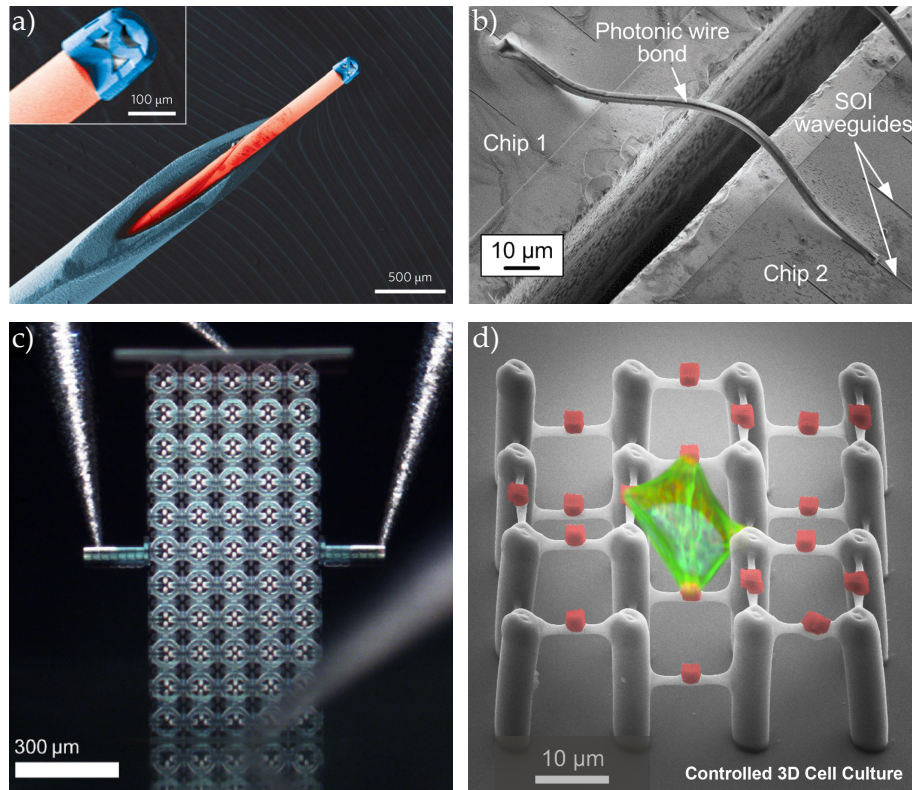
Figure 2.2: Images of a few sample applications of DLW. a) Colored electron micrograph of a microscopic multi-lens objective written onto the tip of an optical fiber (adapted from [23] with permission). b) Electron micrograph showing a photonic wirebond for optical interconnects between waveguides on different substrates (adapted from [24] with permission). c) Light microscope image of a 3D metamaterial that exhibits a sign-reversed Hall coefficient (adapted from [25] with permission). d) Composite picture of live cell attached to a two-component polymer cell scaffold for 3D-controlled cell culture (adapted from [26] with permission).

ical [14, 43, 44], magnetic (Figure 2.2 c)) [25], or thermodynamic [45] response functions have been realized, exhibiting extraordinary material properties. There, the large ratio between writing field size (on the millimeter scale) and minimum feature size (on the sub-micrometer scale) offered by 3D laser lithography has been the key to recent advances. Using DLW, it was possible to integrate 3D structures into microfluidic channels for creating sieves, valves, or pumps on the microscale [46] or create externally driven

micromachines [47]. Here, the epoxy photoresist SU-8 (Microchem) has proved to yield high-aspect ratio structures.

While most of these applications were realized by using standard photoresists and, in some cases, additional material deposition steps, applications in life sciences require more intricate photoresist materials. Employing direct-laser-written scaffolds for cell cultivation has allowed to precisely define the geometry of the extracellular environment and has been used to study growth, adhesion, or migration of cells (Figure 2.2 d)) [48–51]. However, cells require the photoresists not only to be biocompatible but also to offer characteristic distributions of biomolecules. This is usually realized by either post-functionalization of cell scaffolds made of standard acrylate resists [52, 53], employing hydrogels [54], or directly using the protein itself as a photoresist [55]. Many new material systems have recently been developed to offer more flexibility with regard to post-functionalization or biomodification [56].

Along these lines, the development of functional photoresists for 3D laser lithography recently has become a very active field of research. In order to achieve a conductive photoresist supporting 3D structuring, different routes have been explored, *e. g.*, simultaneous photoreduction of a metal salt and polymerization of a photoresist as a support structure [57, 58]. Other approaches rely on including conductive nanoparticles such as carbon nanotubes into the photoresist [59, 60], or aim for achieving semiconducting conjugated polymer networks by DLW [61]. Nevertheless, an ideal and universally applicable photoresist with practically useful values of conductivity is still elusive. Recent efforts towards cleavable photoresists have achieved materials that can be cleaved by different chemical stimuli, some of which are even potentially biocompatible, enabling removable support structures or cell scaffolds [62–64]. The inclusion of liquid crystal elastomers into the DLW process allows to incorporate liquid crystal layers into 3D structures enabling light-triggered actuation of micrograbbers [65] or multilayer liquid crystal phase modulators [66].

2.1.2 THRESHOLDING BEHAVIOR AND NONLINEARITY

The exposure dose profile $D(\vec{r})$ is a measure for the energy per area that is deposited in the photoresist during exposure and is proportional to the time integral over the laser beam intensity I,

$$D(\vec{r}) \propto \int_{t_{\text{exp}}} I^N(\vec{r}, t) \, \mathrm{d}t \, , \tag{2.1}$$

with the exposure time t_{exp} and the order of nonlinearity N of the process. Strictly speaking, only the electric field $\vec{E}$ is relevant for absorption processes of dipole transitions and thus the squared modulus of the electric field, $|\vec{E}|^2$ should be used here instead of I. However, as $I \propto |\vec{E}|^2$, I mostly stick to the term intensity for sake of simplicity. Before I look into the nonlinearity, first some general aspects connected to the writing process need to be described.

In negative-tone photoresists, the exposure dose usually relates linearly to the cross-link density. Regardless of the nature of the microscopic chemical reactions that lead to cross-linking, photoresists effectively accumulate the exposure doses that they have seen. This is often paraphrased as the photoresist possessing a "memory" [67]. For DLW, this means that subsequent exposures of neighboring areas are not independent but contribute to each other as the tails of the intensity distributions of the laser foci are added to the dose as well.[2] The consequence of this behavior are so-called proximity effects, *i. e.*, lines written closely to other structures become wider or small gaps intended to be between two structures become closed [69]. The microscopic origin depends on the employed material system. For acrylate photoresists, the exposure dose defines a spatial distribution of radicals that initiate polymerization. Partly polymerized material can be further extended or incorporated into existing networks by polymerization initiated by subsequent exposures. For photoresist based on cationic polymerization, *e. g.* SU-8, the accumulated exposure dose profile translates into a spatial distribution of photoacids that initiate polymerization when the resist is heated after lithography.

---

[2] This behavior is present in planar mask lithography, too, limiting the achievable resolution. Here, double-exposure techniques provide remedy although at the cost of higher complexity [68].

With increasing locally accumulated exposure dose, the cross-link density increases and eventually a continuous network is formed. At some material-specific degree of cross-linking, at the gelation point, the network is rendered insoluble with respect to the development step of the DLW process. The corresponding exposure dose is called threshold dose D_{thr} as only parts of the photoresist that have accumulated a dose $D \geq D_{\text{thr}}$ remain after development while the rest is washed away. In DLW, structures are often written at a constant scan speed which can be thought of a constant exposure time per voxel given by the quotient of beam width and scan speed. Thus, the threshold dose usually translates to a fixed writing threshold intensity or power.

Nonlinearity

As already mentioned above, fabrication of truly 3D structures requires a nonlinear process, *i. e.,* the value of N in Equation 2.1 needs to be larger than 1 [70]. Intuitively, N can be understood as the number of photons that need to be absorbed in a microscopic absorption process leading to cross-linking, *e. g.,* $N = 2$ for two-photon absorption. For demonstration, we consider writing a large plane perpendicular to the optical axis z by scanning the whole plane with the laser beam (Figure 2.3 a)). If we assume constant exposure time and temporally constant intensity, the accumulated exposure dose of a single point in the photoresist at an axial position z is given by the integral

$$D(z) \propto \int\limits_{-\infty}^{\infty} \int\limits_{-\infty}^{\infty} I^N(x, y, z)\, \mathrm{d}x\, \mathrm{d}y \; . \tag{2.2}$$

We compare two such points at different axial positions, z_1 at the beam waist and z_2 at some distance. The different beam diameters[3] at these points lead to different intensities I_1 and I_2 as the laser power is distributed over different areas A_1 and A_2. We assume that the absorption coefficient of the photoresist is small and thus the laser power is constant along the optical axis. For sake of simplicity, we approximate the lateral intensity distribution

---

[3] Theoretically, the electric field spans an infinite space. In laser physics, the beam diameter is usually defined as the $1/e^2$-width of the intensity distribution.
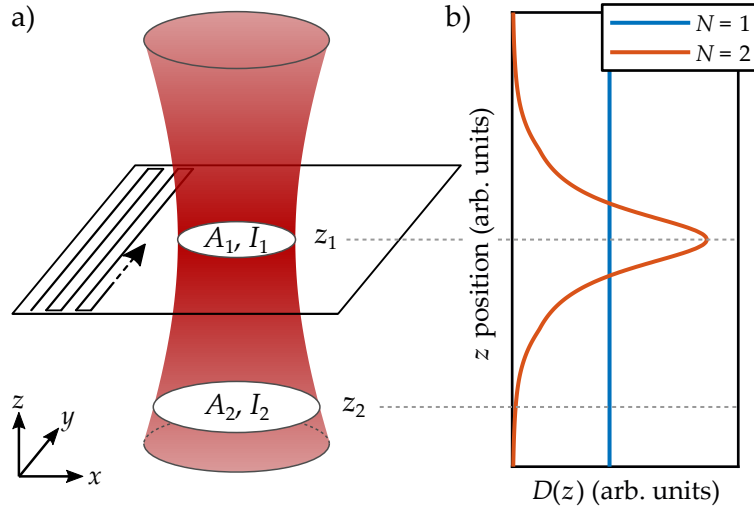
Figure 2.3: a) Exposing a plane with a focused laser beam leads to dose accumulation in all axial planes. b) Two points in the planes at $z = z_1$ and $z = z_2$, respectively, acquire different doses $D(z)$ depending on the order of nonlinearity N.

with a rectangular function.[4] As an example, we arbitrarily choose z_2 such that $A_2 = 2 \cdot A_1$ and thus $I_2 = \frac{1}{2}I_1$. Solving the integral yields

$$D(z_1) \propto I_1^N \cdot A_1 \tag{2.3}$$

$$D(z_2) \propto I_2^N \cdot A_2 = \left(\frac{1}{2}I_1\right)^N \cdot 2A_1 = \left(\frac{1}{2}\right)^{N-1} \cdot D(z_1) . \tag{2.4}$$

Clearly, in case of a linear process with $N = 1$, both points accumulate the same dose, *i.e.*, achieve the same degree of cross-linking. This means that not only the exposed plane at the beam waist is written but the whole volume below and above the plane is cross-linked as well. This way, no 3D structuring can be achieved. In case of $N > 1$, the plane at z_1 receives a larger dose. This allows for spatial confinement of the cross-linked volume if the laser power is chosen such that the threshold dose is only exceeded in the vicinity of z_1. Figure 2.3 b) demonstrates this for the case of $N = 2$.

As already indicated above, the value of N is often determined by the absorption mechanism. For one- or two-photon absorption, one finds $N = 1$

---

[4] A more realistic treatment can be found in [71].

or $N = 2$, respectively. The nonlinearity of a photopolymerization process can be determined experimentally by different methods [12, 72, 73], one of which is also used in this thesis (see Sections 4.3.2 and 5.4.1). In experiments, one often finds non-integer numbers that can be interpreted as mixtures of several processes with different nonlinearities [72]. Apart from absorption processes, photoionization of initiator molecules can occur under certain conditions and exhibits higher nonlinearities.

In this picture, it is interesting to look at the small but rising number of publications that report on 3D laser lithography using cw laser sources, some of which stem from our group [8, 9, 11, 12]. Clearly, the comparatively low peak intensities of cw lasers should not allow for efficient two-photon absorption if reasonable two-photon absorption cross-sections are assumed. Instead, it has been assumed that the underlying process is one-photon absorption with very low extinction coefficients such that most of the light still reaches the focal position inside the photoresist material. In this case, $N = 1$ in the framework presented above, *i.e.*, $D(\vec{r}) \propto I(\vec{r})$. The nonlinearity is introduced during the process of polymerization that follows after initiation, such that the cross-linking density ρ depends nonlinearly on the dose, $\rho(\vec{r}) \propto D^N(\vec{r})$. However, a detailed analysis or spectroscopic proofs have not been provided yet. It is also unclear how such chemical nonlinearities influence cases where very clear two-photon processes are found. While the nonlinearity is crucial for fabrication of 3D structures, it can have very different origins.

2.1.3 RESOLUTION CRITERIA

Important figures of merit for the performance of a lithography process are the achievable feature size and the resolution. As these two quantities are often (wrongly) equated in literature, I would like to clarify their meaning. The minimally achievable feature size is given by the spatial extent of the smallest structure that can be fabricated. It corresponds to the size of a single voxel written closely to the threshold. In practice, often the minimal linewidth is specified as it can be measured more reliably than single voxels and is more relevant for practical purposes. Theoretically, the feature size would not be limited at all if the photoresist exhibited an infinitely sharp thresholding
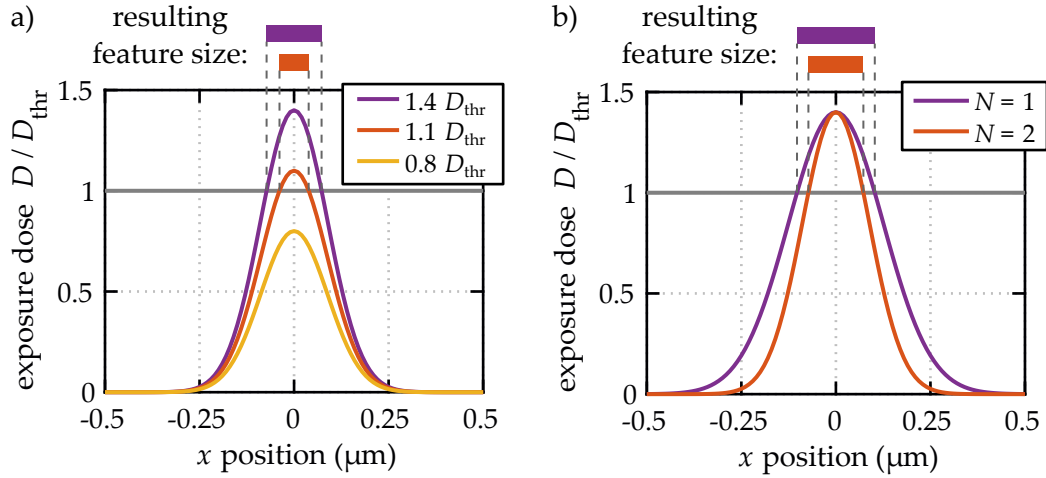
Figure 2.4: Calculations of achievable feature sizes using a focused Gaussian-distributed laser beam with a FWHM of 295 nm at the beam waist. The exposure dose profile D is related to the intensity distribution I by $D(x) \propto I^N(x)$. a) The feature size can be reduced by lowering the laser intensity such that the peak exposure dose approaches the threshold dose D_{thr} (here $N = 2$). b) A comparison between a linear process with $N = 1$ and a nonlinear process with $N = 2$ shows the feature size reduction with increasing nonlinearity.

behavior. In that case, the feature size could be reduced arbitrarily by setting the laser power closer to the threshold value (Figure 2.4). However, in real systems, finite feature sizes are found. Microscopically, this can be traced back to, *e. g.*, diffusion effects [74], or statistical fluctuations [75, 76]. Typical values reported for DLW differ as different measurement methods and geometries are employed. While record lateral linewidths in the sub-20 nm range have been reported for rather artificial setups [77], a more conservative range of 50–70 nm has typically been observed in functional 3D structures, *e. g.*, photonic crystals [15]. It should be noted that the use of a nonlinear process with $N > 1$ leads to reduced feature sizes compared to one-photon absorption at the same wavelength. The reason is that the spatial intensity distribution $I(\vec{r})$ is taken to the power of N, reducing its width by a factor of $\sqrt{N}$ (Figure 2.4 b).

The notion of resolution specifies how closely to each other two such features can be written. In contrast to feature size, this quantity is limited

by diffraction. Here, it is instructive to first look at the resolution limit in classical light microscopy as it was formulated by Ernst Abbe [4]. Abbe considered a periodic grating with grating period a embedded in a medium of refractive index n and illuminated in transmission by light of wavelength λ (Figure 2.5). The grating diffracts the incident light into different diffraction orders denoted by $m \in \mathbb{Z}$ under angles given by $\sin\theta = m\lambda/a$. In case of illumination parallel to the optical axis, the zeroth order is thereby emitted along the optical axis and all higher orders at increasing angles. In order to resolve the grating, it is necessary to collect at least the zeroth and one of the first orders inside the opening half angle α of the optical system, posing a limit to the smallest resolvable grating period a_x. In the extreme case, the two first orders just enter at the edge of the entrance pupil. From the drawing in Figure 2.5, it can be derived that the angular separation between $m = 1$ and $m = -1$ corresponds to a spatial frequency bandwidth of $\Delta k_{xy} = |\vec{k}_1 - \vec{k}_{-1}| = 2k\sin\alpha$ with the wave vector $k = 2\pi n/\lambda$. This leads to the famous Abbe condition

$$a_x = \frac{2\pi}{\Delta k_{xy}} = \frac{\lambda}{2n\sin\alpha} = \frac{\lambda}{2NA} \, , \tag{2.5}$$

with the numerical aperture $NA = n\sin\alpha$. For the axial resolution limit, very similar reasoning yields

$$a_z = \frac{\lambda}{\Delta k_z} = \frac{\lambda}{n - \sqrt{n^2 - NA^2}} \, . \tag{2.6}$$

Translated to lithography, these critical distances a_{xy} and a_z correspond to the minimum distance possible between two features in case of parallel exposure of the whole sample.[5] A first consequence from these relations is that the axial resolution is always at least a factor of 2 below the lateral resolution if only one objective lens is used (implying $\alpha = 90° \Rightarrow NA = n$). For typical values used in this thesis, $NA = 1.4$ and $n = 1.5$, the ratio becomes 2.91. As this fundamental resolution limit is a consequence of diffraction of light it is also referred to as the *diffraction limit*.

---

[5] In industrial deep-UV lithography, employing tilted illumination allowed to improve by a factor of 2 by only using the zeroth and one first order [78].
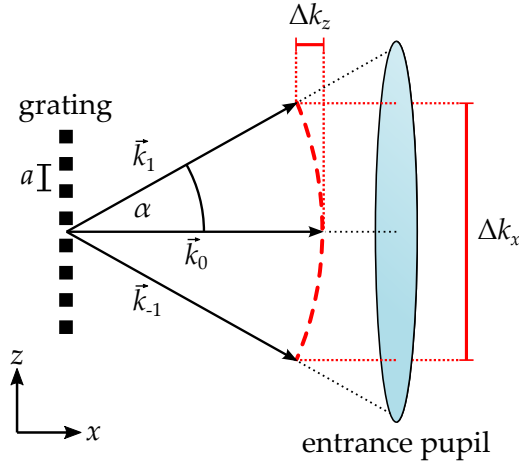
Figure 2.5: Scheme for the derivation of Abbe's resolution formulas. A grating with period a diffracts the transmitted light into different orders with wave vectors $\vec{k}_{0/\pm 1}$ that are collected by the entrance pupil of an optical system. The lateral and axial spatial frequency bandwidths $\Delta k_{x/z}$ of the collected light can be determined geometrically.

In 3D laser lithography, a natural choice for a definition of resolution is Sparrow's criterion which was originally applied for astronomical spectroscopes [79]. The idea here is that two features can still be resolved as long as they are separated by a local exposure dose minimum. We consider two consecutive point exposures separated by some distance a as shown in Figure 2.6. In case of high-*NA* focusing, the intensity distribution has to be calculated numerically, *e. g.*, with the method described in Section A.1. However, we can reasonably approximate the intensity profile with a Gaussian distribution. If a nonlinear process with $N > 1$ is employed the intensity distribution has to be taken to the power of N. For the model calculation, we assume a focused laser beam with a FWHM of 295 nm at the beam waist (corresponding to the laser focus achieved for $\lambda = 700$ nm, also compare to Figure 3.5) and $N = 2$. Because of the dose accumulation behavior of the photoresist described above, the total exposure dose is given by the sum of the two intensity profiles. The power can be adjusted such that the dose in the local minimum is just below the threshold dose while being above at the two maxima. In that case, we obtain two separated features as exemplary shown for $a = 220$ nm in panels a) and c). If we reduce a

further, the minimum disappears eventually and the two features can not be resolved anymore. The critical distance at which this transition occurs determines the resolution according to Sparrow. In the depicted case in panels b) and d), the critical distance is $a = 177\,\text{nm}$. As Fischer and Wegener have demonstrated [6], the numerical determination of the resolution limit according to Sparrow's criterion can be approximated by modifying Abbe's formula (see Equation 2.5) as follows,

$$a_x = \frac{\lambda}{\sqrt{N} \cdot 2NA} \quad \text{and}$$

$$a_z = \frac{\lambda}{\sqrt{N}\left(n - \sqrt{n^2 - NA^2}\right)} \; . \tag{2.7}$$

The additional factor $1/\sqrt{N}$ thereby accounts for the improvement achieved for higher nonlinearities. In the case of $N = 1$, the original formula is recovered. Some example calculations for the setup ($NA = 1.4$, $n = 1.5$, $N = 2$) and the main wavelengths used in this thesis are given in Table 2.1

Table 2.1: Theoretically achievable resolutions for the setup and wavelengths used in this thesis.

λ (nm)	a_x (nm)	a_z (nm)	AR[1]
700	177	515	2.91
820	207	603	2.91

[1] Aspect ratio of the voxel, a_z/a_x

Note that the situation is very different in systems that do not exhibit a thresholding mechanism. Here, the added exposure dose profile will directly be translated into the photoresist without digitization. The resolution criteria still apply but the achievable resolution only reflects in a modulation or corrugation of the chemical reaction induced by the laser light and not in separation of features. An example is the surface functionalization approach presented in Section 4.2.

There are several possibilities to improve the resolution. Increasing the order of nonlinearity N is not straight-forward in practice as absorption processes of lower order have to be suppressed. Increasing the numerical
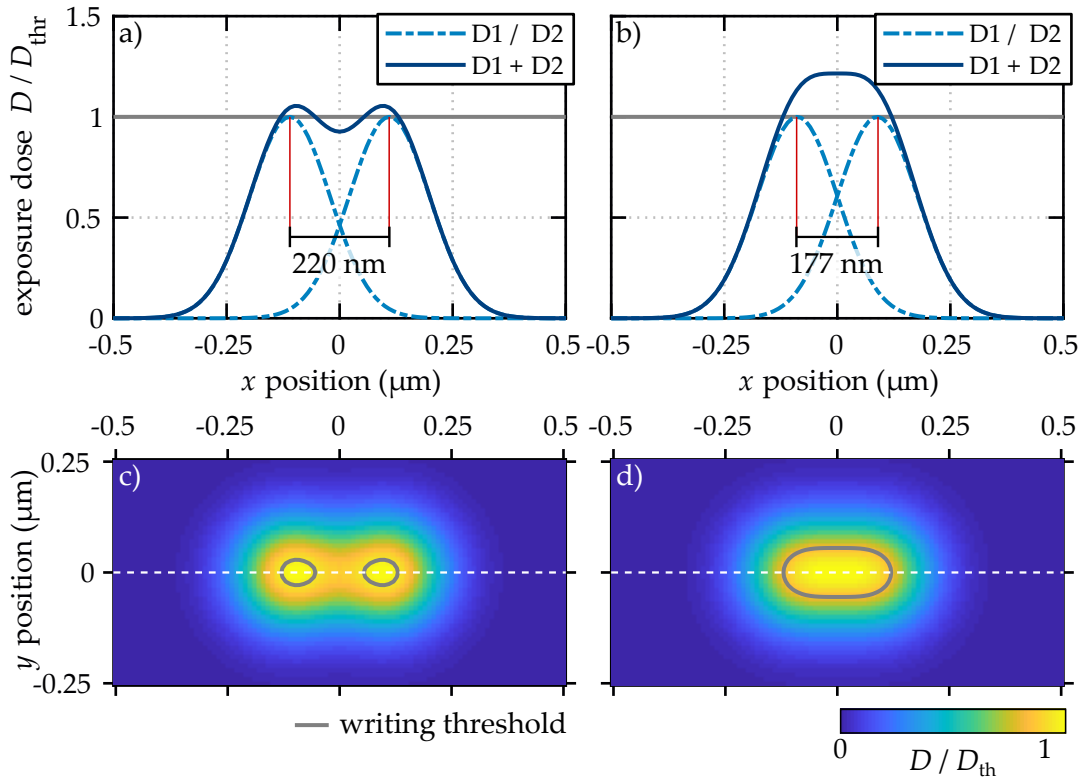
Figure 2.6: Visualization of Sparrow's resolution criterion for a focused laser beam with $\lambda = 700\,\text{nm}$ in DLW. a) Exposure doses of two subsequent point exposures at a distance of 220 nm add up. As the threshold dose is not exceeded at the position of the local minimum, two separate features are written. b) At the critical separation of 177 nm, the diffraction limit according to Equation 2.7, the local minimum has disappeared and the two features have merged. Panels c) and d) show false color plots of the exposure dose in two dimensions. The laser intensity profiles are approximated as Gaussian distributions and a nonlinear process with $N = 2$ is assumed.

aperture NA is limited by geometry and material constraints. At $NA = 1.4$, the opening angle of the objective lens is already 69°. While relying on commercial objective lenses, a considerable increase can only be achieved by employing 4π-illumination systems at the cost of increased complexity and decreased flexibility. Another way to improve the resolution is the reduction of the excitation wavelength λ. In industrial mask-based lithography, decreasing the wavelength was the main driver of the huge advances in

miniaturization of electronics in the last decades [78]. A number of publications demonstrated that this route is viable for DLW, too [9, 12, 15]. However, the required instrumentation poses some limitations. Commercial high-*NA* objective lenses are necessary to achieve a useful axial confinement but are usually not transparent below 350 nm. 3D structuring close to the resolution limit at deep-UV wavelengths is therefore still elusive. Further, generating femtosecond laser pulses at such low wavelengths involves higher-order nonlinear processes, *e. g.* third-harmonic generation, which increases equipment costs and lowers the available laser powers. Therefore, it is desirable to find a way to increase the resolution while staying in the visible wavelength range.

2.2 Overcoming The Diffraction Limit

For more than a century, the diffraction limit was widely accepted as a theoretical limit for optical microscopy. The development of improved far-field imaging techniques such as confocal laser scanning microscopy, multi-photon microscopy, or structured illumination microscopy allowed to stretch this limit by up to a factor of 2 [80].

The diffraction limit could be broken with the advent of near-field imaging techniques such as total internal reflection fluorescence microscopy or scanning near-field optical microscopy. These methods are conceptually not limited by diffraction as they probe the sample with evanescent fields. However, those techniques are limited to very thin samples or surfaces, making them not universally applicable.

Only in the last 25 years, truly diffraction-unlimited far-field microscopy techniques have emerged that have earned their inventors the Nobel prize for chemistry in 2014. These techniques can be divided into two branches. One is formed by stochastic localization microscopy, originally referred to as STORM [81] or PALM [82], that relies on randomly switching a part of the dye molecules on the sample from a non-fluorescent "off" state into a fluorescent "on" state. The fluorescence image is recorded and all dyes are switched back into the off state before a new random subset of the dyes is switched on, and so forth. During post-processing, the location of individual emitting molecules can be retrieved from calculating the centroids of the

blurred spots in the fluorescence image. The precision of this localization procedure can be arbitrarily improved by increasing the number of imaging cycles. The second branch comprises stimulated-emission depletion (STED) microscopy which I describe in detail in the next section.

2.2.1 THE PRINCIPLE OF STED MICROSCOPY

STED microscopy was first proposed by Hell and Wichmann in 1994 [5] and soon extended and improved [83], until sub-diffraction resolution was demonstrated experimentally [84]. Ever since, the technique has found numerous applications, especially in the field of life sciences. In regular laser scanning confocal microscopy, fluorophores are excited from their ground state S_0 into their first excited singlet state S_1 (Figure 2.7 a)). The fluorophores decay back into S_0 emitting fluorescence photons. As the excitation take place everywhere within the focal volume of the excitation laser, the resolution of the resulting fluorescence image is diffraction-limited. The idea of STED microscopy involves a second laser beam with a wavelength fitting to the energy gap between S_1 and a higher vibronic sideband of the S_0 manifold, S_0^*. The second laser beam will cause the molecules in S_1 to transit into S_0^* by stimulated emission. Thus, the population of fluorophores in the S_1 state is decreased, hence this second laser beam is called *depletion* beam. The molecules thereby cannot contribute to the fluorescence signal which can be spectrally separated from the stimulated emission signal. Thus, the fluorescence is effectively suppressed, *i. e., switched off,* by the depletion laser light. The depletion laser is employed in a special focus shape that features a point, line, or plane where the $\vec{E}$-field has a zero crossing, *i. e.,* the intensity touches zero. This special point is overlaid with the intensity maximum of the excitation laser beam (Figure 2.7 b)). By increasing the depletion laser power, the fluorescence can be suppressed everywhere in the vicinity of this special point, confining the volume in which fluorescence takes place. As the two foci are scanned over the sample, an image with sub-diffraction resolution can be obtained. Obviously, it is important that the switching of the fluorophores is reversible, as each molecule needs to be excited and depleted many times while the laser beams scans over its position.
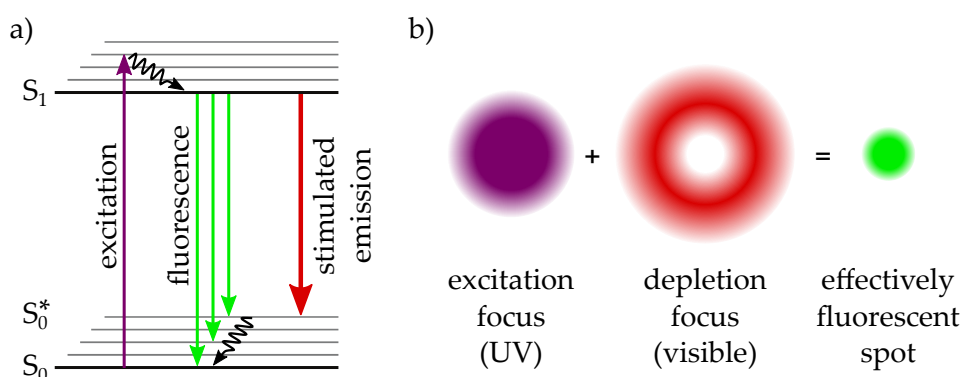
Figure 2.7: a) Jablonski diagram for a fluorescent dye molecule in STED microscopy. The dye is excited into the S_1 manifold by absorption of UV light, leading to fluorescence back into S_0. By stimulated emission induced by visible light, the S_1 can be depopulated, suppressing fluorescence. b) Combination of a Gaussian excitation focus and a depletion focus featuring a point of zero intensity in its center, the effectively fluorescent spot can be reduced.

The Molecular Photoswitch

While the originally proposed approach relies on stimulated emission for suppressing the fluorescence, the scheme was soon extended to other mechanisms [85]. For example, switching off the fluorescence by the depletion laser light could also be realized by bringing fluorophores into metastable dark triplet states [86] or photoisomerization between bistable fluorescent dyes [87, 88] or proteins [89–92]. Common to all these approaches is that the on-off transition is reversible, saturable and induced by a one-photon process [93]. Any mechanism fulfilling these criteria is referred to as a *molecular photoswitch*. In literature, this more general concept is sometimes referred to as reversible saturable optical linear fluorescence transition (RESOLFT), however not unambiguously. For the sake of simplicity, I refer to all of these mechanisms by the term *STED-inspired* microscopy in the following although the underlying mechanism does not necessarily have to involve stimulated-emission depletion.

In order to quantitatively assess the potential resolution increase, the concept is generalized [83, 94]. We assume the molecular photoswitch possesses two states, a non-fluorescent state A and a fluorescent state B.

$$\overset{k_{AB}(x)}{\underset{k_{BA}(x)}{\rightleftarrows}}$$

(A) (dark)   (B) (fluorescent)
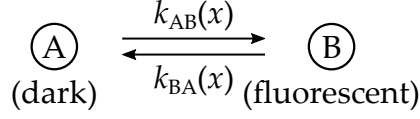
The transition $A \rightarrow B$ proceeds with a spatially varying rate $k_{AB}(x) = \alpha I_{exc}(x)$, proportional to the excitation laser intensity distribution $I_{exc}(x)$. The reverse transition $B \rightarrow A$ is driven by the depletion laser with intensity distribution $I_{depl}(x)$ and proceeds with a rate $k_{BA}(x) = \beta I_{depl}(x)$. α and β denote proportionality factors. An initial excitation pulse brings a part of the molecules into state B such that the population $N_B(x) \propto I_{exc}(x)$. After that, a depletion pulse of duration τ follows, leading to an exponential decrease of $N_B(x)$ by a factor of $\eta(x) = \exp(-I_{depl}(x)/I_S)$, with the saturation intensity $I_S = (\beta\tau)^{-1}$. The fluorescence probability is proportional to the remaining population of B, $N_B(x) \propto I_{exc}(x) \cdot \eta(x)$. For the excitation intensity, we assume a Gaussian distribution of width σ, $I_{exc}(x) = I_{exc}\exp(-x^2/(2\sigma^2))$. In the vicinity of the minimum, the depletion beam shape can be approximated with a parabola, $I_{depl}(x) = I_{depl}ax^2$, where a denotes the steepness of the minimum. For the fluorescence probability, we find again a Gaussian distribution

$$N_B(x) \propto \exp\left(-\frac{x^2}{2\sigma'^2}\right) , \tag{2.8}$$

with a modified width

$$\sigma' = \frac{\sigma}{\sqrt{1 + 2a\sigma^2 I_{depl}/I_S}} . \tag{2.9}$$

Thus, for high depletion powers $I_{depl} \gg I_S$, the fluorescence is confined to a volume proportional to $1/\sqrt{aI_{depl}}$. The improvement in resolution obtained by the STED scheme can be formulated in terms of a modified version of Abbe's resolution criterion (Equation 2.5) [95],

$$a_x \simeq \frac{\lambda}{2NA\sqrt{1 + I_{depl}/I_S}} . \tag{2.10}$$

As the depletion laser power can in theory be arbitrarily increased, the resolution is not limited by diffraction anymore but ultimately only by the size of the fluorescent molecules. Experimentally, the highest lateral

resolution achieved so far with STED-inspired microscopy was 6 nm at an excitation wavelength of 532 nm and a depletion wavelength of 775 nm [96]. The reasoning above subtly assumed that excitation and depletion light is delivered in pulses. This is not a crucial requirement and in fact, STED-inspired microscopy with cw lasers for both excitation and depletion has been demonstrated [80, 97]. The scaling laws derived herein still apply.

Creating Depletion Foci for STED Microscopy

Apart from the molecular photoswitch, the second important aspect of STED-inspired microscopy is the generation of the depletion laser foci. Depending on the desired dimensionality of the depletion focus, *i.e.*, whether a fluorescence confinement should occur in one, two, or three dimensions, several options are available [80]. The underlying principle is the same for all approaches and involves destructive interference of different parts of the focused laser beam in order to create a point, line, or plane of zero intensity. Therefore, the wavefront of the laser beam needs to be modulated accordingly.

Most commonly, transmission phase masks are used for this purpose. By the thickness of the material and its refractive index, an optical path difference between light propagating through air and through the phase mask material can be introduced, defining a locally varying phase shift on the wavefront. Different geometries and the corresponding laser foci are depicted in Figure 2.8. The foci are calculated for a wavelength of 640 nm and $NA = 1.4$ by the method described in Section A.1. If one half-space of the laser beam is phase shifted by π a plane of zero intensity is created in the center of the focus (panel a)). This allows a one-dimensional resolution improvement along the direction perpendicular to the plane. Such a half-space phase mask is used within the experimental work of this thesis and its properties are discussed in more detail in Section 3.2.2. For two-dimensional fluorescence confinement, the depletion beam can be equally split into two beams that are both led through half-space phase masks that are rotated by 90° with respect to each other. Upon recombination of the beams and focusing, a intensity distribution with the shape of a rectangular ring can be achieved [98]. A more elegant way comprises the use of a vortex phase mask which has a helically increasing thickness modulating the phase
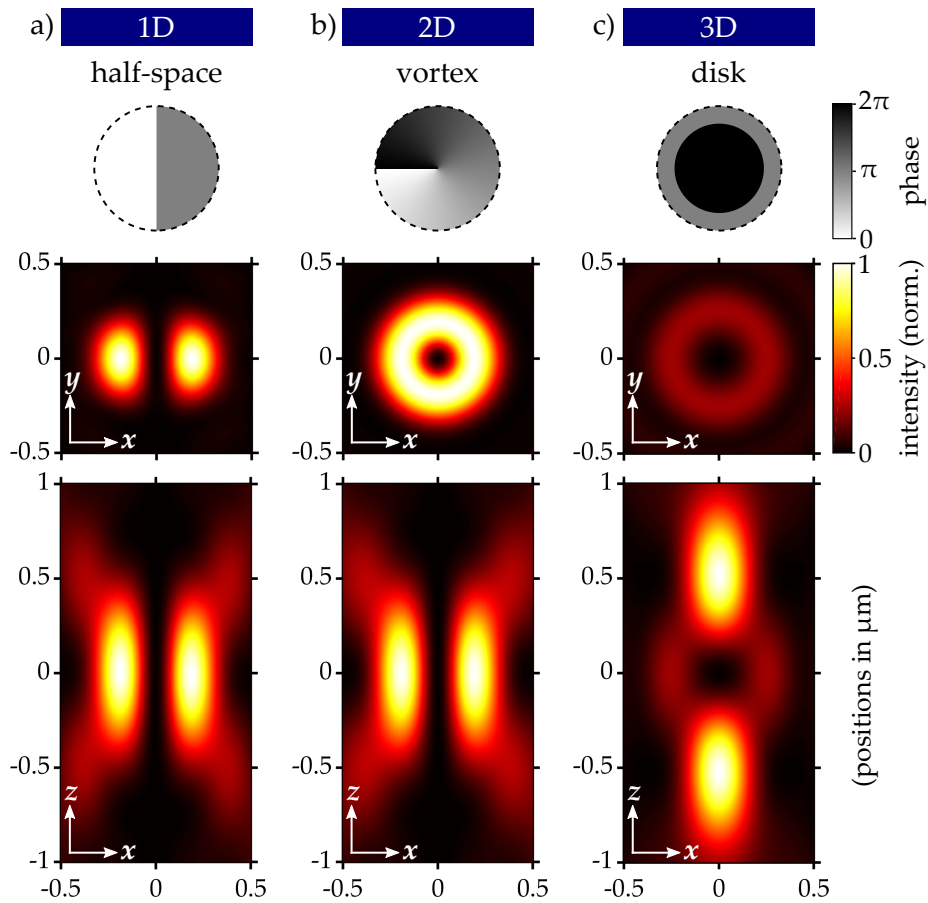
Figure 2.8: a) A 1D confinement can be achieved by using a half-space phase mask. b) A vortex phase mask leads to a donut-shaped intensity distribution in the focus with a line of zero intensity along the optical axis. c) Using a disk phase mask leads to the so-called bottle-beam focus with a point of zero intensity, allowing for 3D confinement. Laser foci are calculated assuming a wavelength of 640 nm and $NA = 1.4$.

from 0 to 2π around the beam center (panel b)). The result is a donut-shaped intensity distribution with a line of zero intensity along the optical axis in its center. In order to create a three-dimensional confinement, the so-called bottle beam focus is generated by a phase mask consisting of a central circle that imposes a phase shift of π onto the central part of the beam (panel c)). The size needs to be correctly matched to the diameters of the beam and the objective lens pupil such that 50 % of the intensity pass through the mask.

In case of an overfilled objective lens pupil, the disk diameter is $1/\sqrt{2}$ of the pupil diameter. However, the intensity in the donut-shaped ring in the lateral plane is low compared to the axial maxima. Therefore, this phase mask has been combined with aforementioned vortex phase mask, again by splitting into two depletion beams [94].

Spatial light modulators based on polarization-sensitive liquid crystals are usually operating in reflection and offer a freely programmable phase pattern (within the limits of pixelation). Thus, it is possible to not only realize different phase patterns with just a single device but also dynamically adapt the phase pattern. This allows fine-tuning and correction of aberrations of wavefronts. Furthermore, adaptive optics can enable imaging deeper into scattering tissue [80]. Other approaches aim for increasing the stability of the beam alignment by passing aligned excitation and depletion beams through specially designed optical elements that only modulate the depletion beam and leave the excitation beam unaltered, *e. g.*, dual ramp phase filters [99] or segmented birefringent waveplates [100].

2.2.2 FROM MICROSCOPY TO LITHOGRAPHY

Soon after the development of STED microscopy, it was proposed to transfer the concept to laser lithography [93]. Out of all different lithography techniques, DLW is a natural choice because of its similarity to STED microscopy with regard to the illumination scheme and the required optical setup. Thus, the concept of STED microscopy can be adopted without significant changes. Importantly, the resolution increase in STED microscopy does not require any post-processing of the image data (although *e. g.* deconvolution is used in practice). It is obtained purely by means of optics and should therefore be achievable in lithography, too. The first experimental demonstrations STED-inspired lithography have been pioneered by the Fourkas group and the McLeod group in 2009 [101, 102]. During the last decade, new suitable photoresist materials have been identified and the technique found its first applications [6, 67, 103, 104]. Especially in the field of nanophotonics, the obtained resolution increase allowed to scale many structures down to exhibit extraordinary optical properties in the visible wavelength range. However, the technique is still at an early stage. Interestingly, several reports

on STED-inspired lithography do not rely on stimulated emission for writing inhibition but exploit different microscopic mechanisms that exhibit a similar effective behavior. Therefore, before going into details on the mechanisms and experimental results, I would like to review the requirements that STED-inspired lithography imposes on photoresist materials.

A Molecular Photoswitch for STED-Inspired Lithography

In order to be suitable for lithographic applications, the scheme of a molecular photoswitch introduced above for microscopy needs to be adapted. The off and on states of the chromophore no longer correspond to fluorescence but to a change in chemical reactivity upon which a reaction can occur that, in case of a negative-tone photoresist, leads to formation of a cross-link. The chromophores, *i. e.*, the molecules in the photoresists interacting with light, should feature an unreactive state A (off) and a reactive state B (on) which can transit into each other by absorption of different colors of light. The transition $A \rightarrow B$ is assumed to proceed with a rate k_{AB} that is a function of the excitation intensity I_{exc}, *e. g.*, $k_{AB} \propto I_{exc}^N$, with the nonlinearity N (see Section 2.1.2). For the reverse transition rate k_{BA}, we assume linear dependence on the depletion intensity, $k_{BA} = \beta I_{depl}$, where β is a proportionality constant. The state B is metastable and eventually, after its lifetime τ has passed, induces a chemical cross-linking reaction during which the chromophore is usually consumed. This is modeled by the irreversible conversion into a third state C that proceeds with a rate k_{BC}, independent of intensity or location.

$$
\underset{\text{(unreactive)}}{\text{A}} \;\; \overset{k_{AB}(x)}{\underset{k_{BA}(x)}{\rightleftharpoons}} \;\; \underset{\text{(reactive)}}{\text{B}} \;\; \overset{k_{BC}}{\longrightarrow} \;\; \underset{\text{(cross-linked)}}{\text{C}}
$$
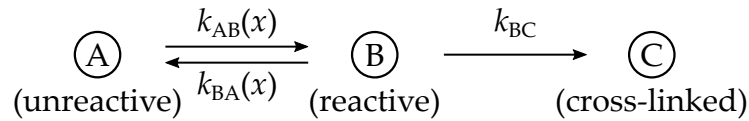
Note that the molecular photoswitch does not necessarily have to be realized by a single molecule but should rather be thought of as a local property of the photoresist. As I will show in Section 2.3, there are examples in literature where the switching behavior is distributed over different molecules. The exposure dose D that the photoresist acquires is proportional to the number of molecules that end up in state C. Therefore, the dose is proportional to the probability that a single molecule reaches C, which is a product of the

probabilities for the transitions $A \to B$ and $B \to C$,

$$D \propto p_{AB} \cdot p_{BC} \, . \tag{2.11}$$

The probability p_{AB} can be assumed to be proportional to the excitation intensity I_{exc}. The probability p_{BC} is given by the ratio k_{BC}/k_{BX}, where k_{BX} and the combined rate of all transitions originating from state B. For simplicity, we assume that all transitions besides the described ones possess a negligible rate.[6] Thus, $k_{BX} = k_{BA} + k_{BC}$. Without any depletion laser, *i. e.*, in regular single-beam DLW, $p_{BC} = 1$ and we obtain an exposure dose D_0. If the depletion laser is switched on,

$$p_{BC} = \frac{k_{BC}}{k_{BA} + k_{BC}} = \frac{1}{1 + k_{BA}/k_{BC}} = \frac{1}{1 + \gamma I_{depl}} \, , \tag{2.12}$$

with the proportionality constant $\gamma = \beta/k_{BC}$. Thus, the depletion effect leads to an lowered effective exposure dose

$$D_{eff} = D_0 \cdot \frac{1}{1 + \gamma I_{depl}} \, . \tag{2.13}$$

We can plug in assumptions for the intensity distributions to find the asymptotic behavior for large depletion powers. Close to the point of zero intensity in the depletion beam, the excitation beam profile can be assumed to be constant, while the depletion beam profile can be described as a parabolic minimum, $I_{depl}(x) = I_{depl}ax^2$. From the condition that a certain threshold exposure dose has to be exceeded for writing, one finds that the width Δx of the written volume follows

$$\Delta x \propto \frac{1}{\sqrt{a I_{depl}}} \, . \tag{2.14}$$

The same scaling law for large depletion powers has already been found for STED microscopy (compare Equation 2.9). For visualization, the expected scaling of feature size and resolution is depicted in Figure 2.9 for laser foci employed in the experimental part of this thesis. A nonlinearity of $N = 2$

---

[6] In case of photoinitiators, fluorescence or non-radiative decays of the excited singlet state can offer such an alternative transition.

is assumed. Panels a) and b) show the dependence of the feature size of an individual point exposure on the depletion laser power. The feature size quickly decreases with rising depletion power as a result of the deviation from the Gaussian intensity distribution. The critical distance according to Sparrow's criterion is determined by placing two such point exposures next to each other and iteratively decreasing the distance until, at the critical distance, the local minimum in the combined exposure dose profile disappears (see Section 2.1.3). As argued above, the individual exposure doses can simply be added because of the "memory" of the photoresist. Panel c) shows the dose profiles for zero and a finite depletion power. In the first case, the critical distance is 177 nm, as already determined in Figure 2.6. For a depletion laser power of $3\gamma^{-1}$, the resolvable distance is considerably reduced to 58 nm. As depicted in panels b) and d), the curves for both figures merit become flatter with increasing depletion laser power.

Time Constants Matter

As a rule of thumb, one can expect a 10-fold increase in resolution for a 100-fold increase in depletion power due to the inverse square root scaling. With the same increase, possible parasitic writing by one- or two-photon absorption of the depletion laser beam due to residual absorption would increase by a factor of 100 or 10000, respectively. In other words, the rate k_{AB} can have a contribution proportional to the depletion intensity (or powers thereof) as well. To avoid such unwanted parasitic writing processes, it is highly desirable that the lifetime of the B state, $\tau = k_{BC}^{-1}$ is very long. In this way, only low depletion laser powers are necessary to achieve efficient photoswitching.

On the other hand, very large lifetimes impose limits on the feasible writing speed [6]. If a donut-shaped depletion focus is used to write thin lines, the time window for depletion τ for one voxel needs to be closed before the adjacent voxel can be exposed. Otherwise the crest of the tailing part of the depletion focus would decrease the exposure dose again. Therefore, the ideal lifetime range is a trade-off. For example, if voxel sizes of $d = 10$ nm are aimed for and $\tau = 1$ ms, the writing speed v is limited to $v \leq d/\tau = 10\,\mu\mathrm{m\,s}^{-1}$. For comparison, the fastest commercially available systems for regular 3D laser lithography offer writing speeds up to $10\,\mathrm{cm\,s}^{-1}$,
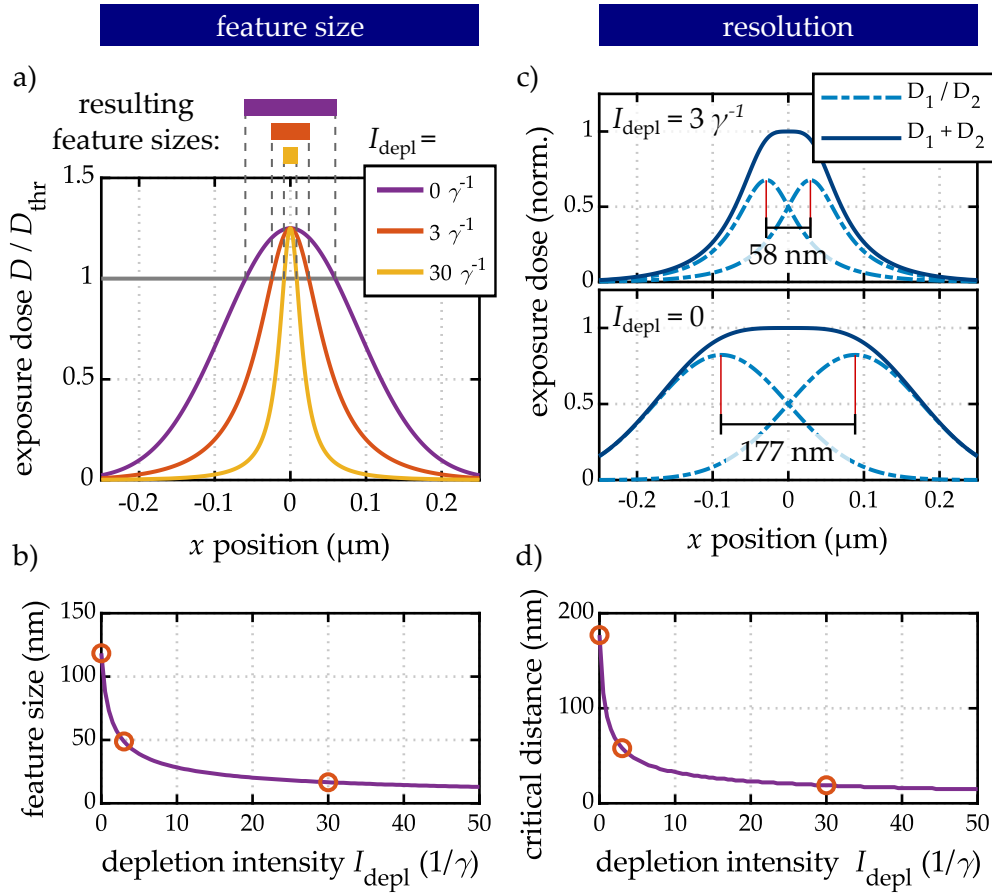
Figure 2.9: Anticipated scaling of feature size and resolution in STED-inspired DLW. Calculations are based on excitation ($\lambda = 700\,\text{nm}$) and depletion ($\lambda = 440\,\text{nm}$) foci used in the experimental part of this thesis (see Figure 3.5) and assume a nonlinearity of $N = 2$. a) With increasing depletion laser power the dose profile deviates from the originally Gaussian shape and reduces in width. The feature size is determined by the width of the above-threshold part of the profile. b) Plot of feature size versus depletion intensity. c) The resolution according to Sparrow's criterion is determined numerically by the critical distance between two consecutive point exposures for which the local minimum in the dose profile disappears. d) Dependency of the critical distance on the depletion intensity.

at feature sizes of $\approx 100\,\text{nm}$, with further increases expected in the near future. However, for real-world applications, very high fabrication precision requiring sub-diffraction resolution is often only needed in some parts of the structures while the bulk can be written with only the excitation beam. Therefore, lower writing speeds for highest precision can be tolerated to some extent.

2.3 DEPLETION MECHANISMS

The technical and optical aspects necessary for STED-inspired lithography can be directly transferred from STED microscopy, *e. g.*, the depletion foci can be generated in the same way. The main challenge in adopting a STED-inspired scheme for lithography is to identify suitable materials that offer a molecular photoswitch that allows for optically induced writing inhibition [105]. In literature, several approaches have been reported that are based on acrylate photoresists that cross-link *via* free-radical polymerization, *i. e.*, the standard photoresists used in DLW. In the following, I briefly review these approaches. For a more extensive treatment, refer to reviews in literature [6, 103] or textbook chapters [67, 104].

2.3.1 DEPLETION BY STIMULATED EMISSION

In standard DLW photoresists, a photoinitiator molecule is excited from the ground state S_0 into the first excited singlet state S_1 by multi-photon absorption (Figure 2.10 a)). After typically 0.1–4 ns [5], it is likely to undergo intersystem crossing into the lowest triplet state T_1. The triplet lifetime varies between different species and ranges from 0.1 ns [106] up to microseconds [107]. From there, the molecule cleaves into radicals that subsequently initiate free-radical polymerization of acrylic monomers. This scheme is very similar to the activation of fluorophores in microscopy (Figure 2.7) and therefore would suggest that one generally can suppress radical generation by stimulated emission. However, many typically employed photoinitiators do not work in this regard [101, 105]. The reason is that these photoinitiators have unfavorably short S_1 lifetimes of around 100 ps [101] which makes

depletion by stimulated emission very inefficient. This cannot simply be countered by increasing the depletion laser power because increased parasitic effects avert effective inhibition [6]. So far, only one family of photoinitiators, 7-diethylamino-3-thenoylcoumarines (DETC), has been reported to support deactivation by stimulated emission. Here, the S_1 lifetime in acrylic monomer is about 1 ns as determined by pump-probe experiments [106]. DETC can be excited *via* multi-photon absorption at 800 nm and can be depleted by stimulated emission at 532 nm [106, 108].
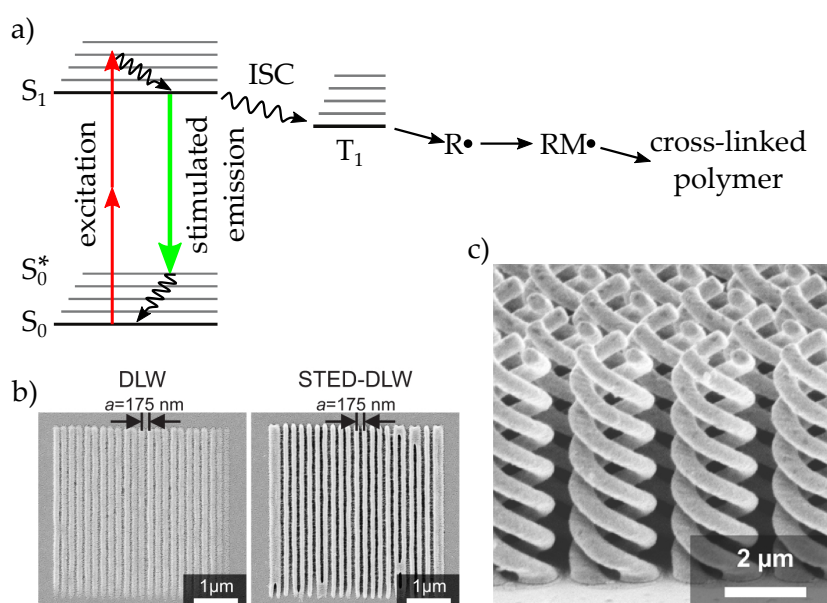
Figure 2.10: a) Jablonski scheme showing the typical initiation and cross-linking process of a radical photoinitiator. By using stimulated emission, the S_1 manifold can be depleted before intersystem crossing (ISC) into the triplet state occurs (adapted from [6] with permission). b) Lateral resolution improvement achieved by STED DLW in comparison to regular DLW (adapted from [109] with permission). c) Gold triple helices fabricated by inverting shell structures written by STED DLW (adpated from [110] with permission).

Using DETC-based photoresists, 3D structures were fabricated with resolution below the diffraction limit in both lateral and axial directions (Figure 2.10 b)) [109, 111]. Current state-of-the-art lateral feature size and resolution are 55 nm and 120 nm, respectively [111]. In the same work, the

smallest axial feature size measured on a suspended line was 53 nm. Apart from demonstration experiments, a number of applications has been enabled by STED lithography based on DETC, many in the field of nanophotonics. Woodpile photonic crystal structures were fabricated with lateral rod distances down to 175 nm (corresponding to an axial resolution of 375 nm) exhibiting pronounced optical stop bands in the visible spectrum [109]. By a double-inversion process, such structures were transferred into titania, yielding photonic crystals with a complete 3D bandgap in the visible wavelength range [35]. Further, carpet invisibility cloaks [112] and different helical metamaterials were fabricated (Figure 2.10 c)) [110, 113, 114]. In all these publications, the results were mainly enabled by the improvement in axial resolution gained by STED lithography. Recently, functional photoresist formulations based on DETC that allow for sub-diffraction structuring was demonstrated. By including metal oxo clusters [115] or acrylate monomers carrying functional moieties into the photoresist [116], orthogonal post-functionalization of composite sub-diffraction-sized 3D structures has been enabled, *e. g.*, for applications in biomedical research. Other approaches aim for post-modification of structures made of pure acrylate [117] or parallel reduction of metal salts [118].

At high depletion laser powers, parasitic writing by the depletion laser poses a limitation to the performance of DETC-based photoresists. Unfortunately, reducing the pulse repetition rate or adding coinitiators to the photoresist does not provide a remedy [119].

2.3.2 DEPLETION BY EXCITED-STATE ABSORPTION

For some photointiators, the pathway towards radical generation can be interrupted by excited-state absorption from the lowest triplet state T_1 into higher triplet states (Figure 2.11 a)). From there, the molecules undergo reverse intersystem crossing leading to non-radiative decay back into the S_0 ground state or formation of a non-reactive species, evading radical formation. This mechanism was used in one of the first experimental demonstrations of STED-inspired DLW, based on malachite green carbinol base (MGCB) as photoinitiator [101]. Pulsed two-photon excitation and one-photon depletion were both at 800 nm. Using a bottle-beam depletion focus, the

voxel aspect ratio was decreased to from > 3 to 0.5 and the smallest lateral feature size was measured to be 40 nm (Figure 2.11 c)). Other authors used the photoinitiator isopropyl thioxanthone (ITX) and proved sub-diffraction patterning using a depletion wavelength of 532 nm (Figure 2.11 b)) [105]. Originally, it was assumed that depletion for ITX takes place *via* stimulated emission, however later studies of transient absorption spectra showed that excited-state absorption is prevalent [108]. Interestingly, the triplet state of the photoinitiator DETC can also be depleted by excited-state absorption at 642 nm, although the details of the deactivation mechanism are not clear yet [107, 120].

MGCB exhibits very long triplet lifetimes on the order of milliseconds and does therefore not allow high writing speeds in combination with 2D or 3D confinement. ITX performs better in this regard with triplet lifetimes on the order of microseconds [107]. Recently, an ITX-based photoresist suitable for STED-inspired DLW was doped with fluorescent dyes, allowing for inspection of the resulting nanoscopic structures with STED microscopy [121].

2.3.3 PHOTOINHIBITOR LITHOGRAPHY

In contrast to the approaches presented above, here, the photoinitiator is not affected by the depletion laser at all. Instead, inhibitor molecules are added to the photoresist that can be activated by one-photon absorption of the depletion laser light (Figure 2.12 a)). Once activated, these molecules cleave into weakly reactive radicals leading to chain termination or scavenging of radicals. Thus, the polymerization process is inhibited. In literature, first one-photon absorption was reported for the excitation of the photoinitiator [102, 122]. Later, two-photon excitation with pulsed laser sources was employed [123]. The photoinhibitor that has been used in most reports is tetraethylthiuram disulfide. Using this technique, feature sizes down to 40 nm were reported for isolated dots and linewidths down to 130 nm for individual isolated lines (Figure 2.12 b)) [122]. If written in the vicinity of large previously exposed structures, linewidths were reduced down to 10 nm and still resolved in a distance of 52 nm [123]. However, these extreme results have to be taken with a grain of salt as useful applications have not been demonstrated yet. Furthermore, in the regime of sub-threshold
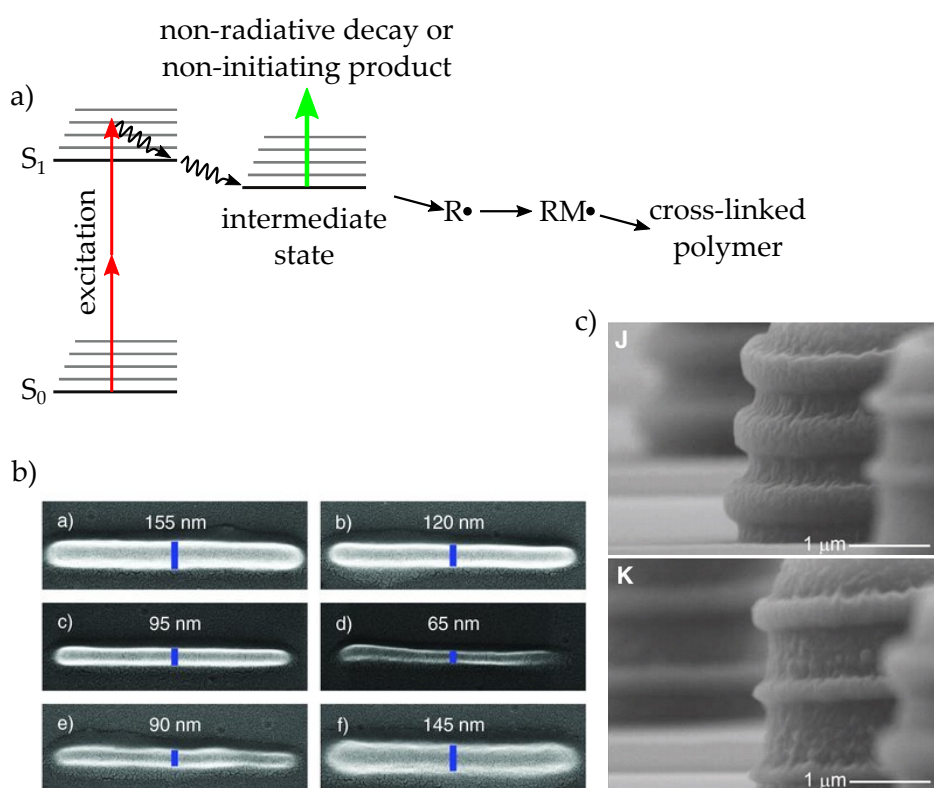
Figure 2.11: a) Scheme showing the depletion of intermediate states by excited-state absorption, suppressing polymerization (adapted from [6] with permission). b) Linewidth enhancement achieved by STED-inspired DLW using the photoinitiator ITX. Subpanel depletion laser powers range from 0 to 80 mW a)–d) and up to 270 mW e)–f) (adapted from [105] with permission). c) Towers with rings fabricated without (J) and with (K) the depletion laser switched on demonstrate the axial feature size improvement using the photoinitiator MGCB (adpated from [101] with permission.)

exposures in the vicinity of existing structures, similar results were reported for regular DLW without any depletion beam [77]. A conceptual draw-back of this approach is the irreversible consumption of the photoinhibitor molecules. Especially when writing dense patterns, the depletion effect could be less efficient if the density of photoinhibitor molecules decreases. Further, diffusion of molecules and radicals might pose major limitations to this technique [124]. Nevertheless, the achieved resolution increase allowed for fabrication of gyroid structures mimicking naturally grown patterns in
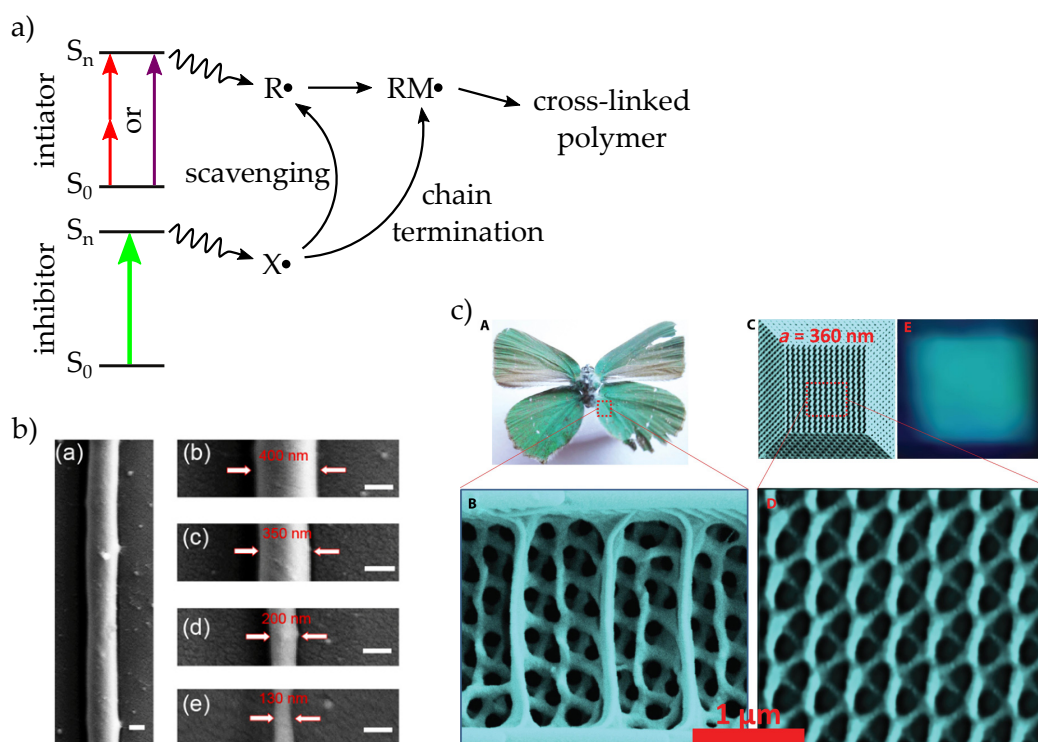
Figure 2.12: a) Scheme of Photoinhibitor lithography. Photoactivated inhibitor generates radicals that interrupt the radical polymerization (adapted from [6] with permission). b) Linewidth enhancement achieved by using this technique. Depletion laser powers range from 0 to $2\,\mu W$ in subpanels (b)–(e) (adapted from [122] with permission). c) Gyroid structures fabricated by photoinhibitor lithography replicate structures found in butterfly wings (adpated from [125] with permission).

the wings of butterflies (Figure 2.12 c)) [125].

2.3.4 OTHER APPROACHES FOR SUPER-RESOLUTION LITHOGRAPHY

Apart from STED-inspired approaches, a number of different schemes have been proposed and realized to achieve sub-diffraction resolution in optical lithography. These concepts rely on manipulating the optical near field close to the photoresist and are limited to planar structuring. For example, Menon and coworkers introduced absorbance-modulation optical lithogra-

phy (AMOL) [126]. Here, a thin film of a photochromic material is deposited on top of a photoresist layer. The photochromic material is initially opaque and switches into a transparent state and under exposure to a wavelength λ_1 which is also used to expose the photoresist underneath. By a second wavelength λ_2, the material is driven back into the opaque state. Similar to the concept of STED microscopy, overlaying a intensity peak of λ_1 with a minimum between two peaks of λ_2 leads to a lateral confinement of the transmittance window for λ_1. This concept has been demonstrated experimentally for interference lithography, where feature sizes of 30 nm have been achieved [127]. Sub-diffraction resolution can thereby be achieved by consecutive exposure steps with spatially shifted wave patterns [128]. The development of AMOL has been mainly driven by the original inventors and has led to a number of advances [129]. For example, it was possible to leave the photoresist layer away by using the photochromic layer itself as the photoresist [130]. However, AMOL is conceptually limited to planar surfaces.

A different avenue was opened up by developments in transformation optics in metamaterials that allowed to achieve extraordinary material properties such as negative indices of refraction. Sparked by the theoretical proposal of the *perfect lens* [131], various designs for such hyperlenses or metalenses have emerged, that can achieve focusing that is not limited by diffraction [132]. Generally, the idea is to create efficient coupling of evanescent modes in the near-field to propagating far-field modes. An application in lithography is prospected and first experimental results have been recently reported [133, 134]. However, the concept is limited to planar structures and is still far from meaningful applications. Further, hyperlenses comprise complex multi-material architectures that need to be fabricated directly on top of the photoresist, which makes the lithography process extremely more complex.

2.3.5 ON THE WORK IN THIS THESIS

In conclusion, the search for efficient molecular photoswitches for STED-inspired laser lithography is not over yet and provides significant challenges to both physics and chemistry [56]. Especially the constraints in terms of

reversibility and time constants rule out many prospective materials. All mechanisms presented in the previous section are based on photoresists that cross-link *via* free-radical polymerization. These photoresists exhibit good writing performance and high resolution and are the well-known workhorse resists in DLW. However, the depletion mechanisms have to compete with the fast dissociation process of the photoinitiator molecules. Further, the voxel size is only in part determined by optics as the polymerization proceeds fast and freely after initiation (see Section 2.1.3).[7]

Instead of free-radical polymerization, direct photocontrol of the individual cross-link formation provides an interesting avenue. If each cross-link is formed upon an individual absorption process, the network formation is expected to follow step-growth dynamics which is slower and reaches higher conversions than radical-induced chain growth [135]. Thus, it can be expected that the cross-linked volume more precisely follows the optically applied exposure dose distribution.

In this thesis, I present two novel materials that can act as molecular photoswitches for STED-inspired laser lithography, namely intermediate-state photoenols generated from methylbenzaldehyde and photochromic spirothiopyran. They can be excited by nonlinear multi-photon absorption and form networks by step-growth cross-linking. In both cases, photoisomerization between a reactive and a non-reactive state constitutes the switching behavior necessary for efficient depletion. During switching, the molecules undergo electronic rearrangement and form chemically distinct intermediates that have comparatively long lifetimes in the range of microseconds, leading to low requirements on depletion laser powers.

---

[7] Photoinhibitor lithography tackles this issue to some extent.

3 Chapter 3
Experimental Methods

A few of the many parts that compose the lithography setup.

In this chapter, I describe the laser lithography setup used for sample fabrication in this thesis. The methods for generation and characterization of the laser foci are explained. Moreover, I describe the general workflows for sample processing and characterization for two different experimental approaches taken in this thesis: surface functionalization and 3D laser lithography.

3.1 LASER LITHOGRAPHY SETUP

For all DLW experiments reported throughout this thesis, a custom-built laser lithography setup was employed. It was originally built by Joachim Fischer and was used in previous work of our group [72, 119, 136]. To match the requirements for the photoresist investigated in this work, the setup was modified. A scheme of the setup is depicted in Figure 3.1.

The main laser source is a tuneable titanium-sapphire oscillator (Chameleon Ultra II, Coherent) delivering pulses with a duration of 150 fs and a repetition rate of 80 MHz, used for excitation of the chromophores in the photoresist. The wavelength was usually tuned to 700 nm for experiments with the photoenol system based on the methylbenzaldehyde chromophore (see Chapter 4) or to 820 nm for experiments with the spirothiopyran chromophore (see Chapter 5). The laser beam is attenuated using a $\lambda/2$-waveplate and a polarizer (not depicted). In order to modulate the laser power, the beam is passed through an acousto-optic modulator (AOM) (MTS40-A3-750.850, AA Opto Electronic). The first diffraction order is used for DLW, while the zeroth order is removed from the optical path. The beam is then expanded by a Kepler telescope to match the beam width with the back aperture of the objective lens. A motorized mirror allows for computer-controlled precise and automated adjustment of the beam angle and thus of the lateral focus position in the focal plane. Depending on the photoswitch material to be investigated, one of two different depletion laser sources can be used:

Photoenol photoswitch. A continuous-wave diode laser at 440 nm (LD-H-D-C-440, Picoquant) at a fixed power is passed through a telescope to reduce the beam diameter and a polarizer. The laser power is modulated by an AOM (MT80-A1,5-400.442, AA Opto Electronic) before the laser is coupled into a polarization-maintaining fiber (PMC 400Si-2.3-NA014-3-APC-300P, Schäfter & Kirchhoff).

Spirothiopyran photoswitch. A continuous-wave diode laser at 640 nm (iBeam smart PT 640, Toptica) is used. It allows for external analog modulation of the laser output power. The laser features a fixed laser coupling into a polarization-maintaining fiber.
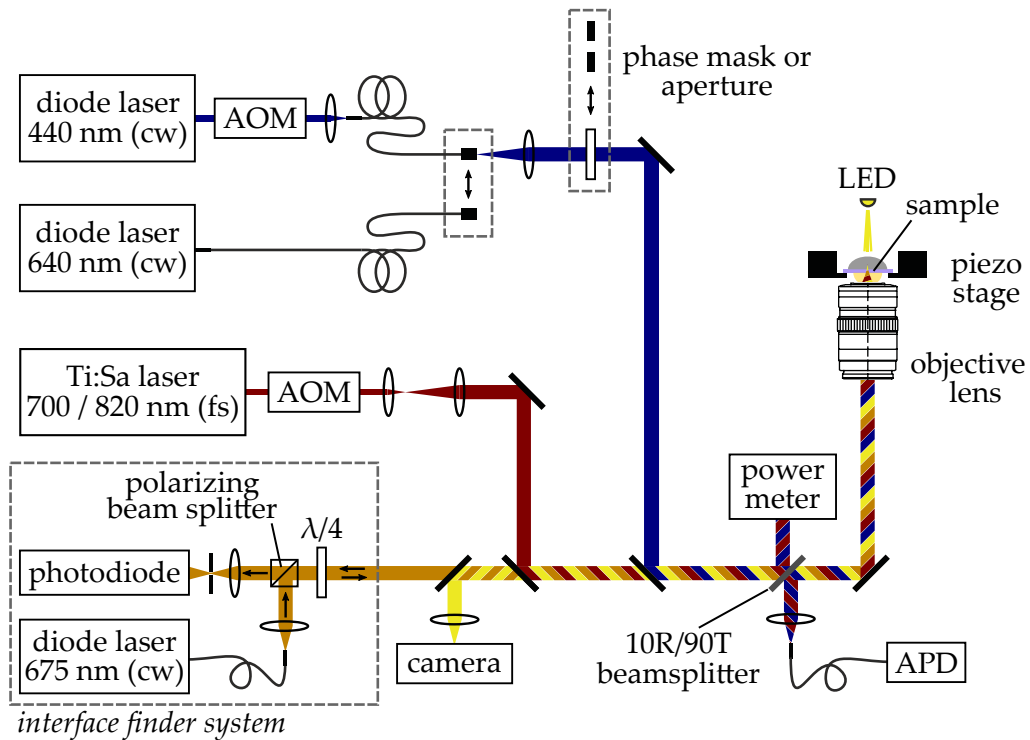
Figure 3.1: Scheme of the employed setup for laser lithography. As depletion laser source, either a 440 nm diode laser is used for lithography using photoenol-based materials (depicted case) or a 640 nm diode laser is used for the spirothiopyran chromophore. Instead of a phase mask (depicted case), a partially closed aperture can be introduced into the depletion beam.

The depletion laser light is coupled out using a beam collimator (60FC-L-4-M30-01, Schäfter & Kirchhoff) and passes an additional polarizer for polarization clean-up. At this position, the depletion beam wavefront can be altered by introducing a transmission phase mask, that imposes a spatially variant phase shift. This leads to a depletion focus featuring a point, line, or plane of zero intensity. Alternatively, a partially closed aperture can be introduced to widen the depletion beam. The excitation and depletion beams are combined using a dichroic beam splitter (zt 640 rdc, AHF) and both beams pass through a 10R/90T beamsplitter (F21-032SG, AHF). To allow a convenient measurement of the laser powers, the reflected portion of the light is guided to a power meter. The transmitted light is focused by an

oil immersion objective lens with a numerical aperture of $NA = 1.4$ (HCX PL APO 100×/1.4-0.7 OIL CS, Leica) that is aligned upwards in an inverted-microscope fashion. Both laser beams are linearly polarized. The power values specified throughout this thesis correspond to the power entering the objective lens pupil.

A 2D piezo stage (P-734.2CD, Physik Instrumente) holds the sample and allows for its relative lateral movement with respect to the fixed laser beam foci within the scanning range of 100 µm × 100 µm. It is mounted onto a motorized stage (P-M-686, Physik Instrumente) that enables coarse movement. For movement along the optical axis, the objective lens is mounted onto a vertical piezo actuator (P-733.ZCL, Physik Instrumente) with a range of 100 µm. The lateral directions will be denoted by x and y, the axial direction by z. The sample is illuminated by a LED at 660 nm in transmission and can be monitored with a CCD camera (DCC1545-M, Thorlabs). The setup is controlled by a PC using a custom-built software written in Matlab (Mathworks). Two data acquisition interface cards (PCI-MIO-16XE-10 and PCI-6731, National Instruments) provide the necessary digital and analog input and output ports.

A common and sometimes challenging task (especially for novel photoresist mixtures) during lithography experiments is the identification of the interface between substrate and photoresist. To simplify this task, an automatic routine is implemented, where a laser diode at 675 nm (LPS-PM675-FC, Thorlabs) is switched on while the sample is scanned axially. Initially, the emitted light is linearly polarized which leads to reflection on a polarizing beam splitter. After this beam splitter, the light passes through a $\lambda/4$-waveplate creating circularly polarized light that is focused onto the sample. The light is reflected at the glass-photoresist interface, changing the handedness of circular polarization traveling back through the beam path. At the $\lambda/4$-waveplate, the light is converted back into linearly polarized light with polarization now being perpendicular to the original orientation. Thus, the light can pass through the polarizing beam splitter and is focused through a pinhole onto a photodiode. To suppress noise and the influence of ambient light, the diode laser is electronically chopped at 4 kHz and the signal is recorded using a lock-in amplifier (SR830, Stanford Research Systems). The z-position at which the reflectance signal peaks marks the

position at which the laser focus hits the interface.

3.2 Generation and Characterization of Laser Foci

3.2.1 Measurement Method

A very important task in STED-inspired DLW is the adjustment of the two laser foci. Also, it is crucial that both beams are precisely overlaid. An appropriate measurement technique is necessary to be able to characterize the intensity distributions of the laser foci, *i. e.*, their point-spread functions. Therefore, subwavelength-sized gold nanoparticles are scanned through the foci and the back-scattered signal is recorded (Figure 3.2).

For preparation of the measurement sample, a dispersion of gold beads with an average size of 100 nm was dropcasted onto a plasma-activated cover glass. In order to reduce unwanted background signal by Fresnel reflections from the glass-air interface, the sample was covered with a layer of the photoresist Ormocomp (micro resist technology) with a thickness of 20 μm that was cured by UV light. The refractive indices of cured Ormocomp and the glass substrate match very well. To suppress Fresnel reflections from the resist-air interface, a droplet of immersion oil was placed on top.

While scanning the focal volume with a single gold bead, the laser beams are electronically chopped with a frequency of 4 kHz. This is achieved either by modulating the AOMs or, in case of the 640 nm diode laser, by directly modulating the diode current. A part of the backscattered light is reflected when passing the 10R/90T beamsplitter and collected by a lens which couples the light into a multimode fiber with a core diameter of 50 μm. The fiber is connected to an avalanche photodiode (APD) (a-Cube S500-01-FC, Laser Components). The signal is extracted by the lock-in amplifier and recorded with the PC. The point-spread function is reconstructed by software. In order to measure both laser foci in parallel, the two laser beams are both chopped with a duty cycle of 50 % and a relative phase shift of 90°. Thus, both laser foci can be measured in one single pass by using the two channels of the lock-in amplifier. This becomes especially important when overlaying the beams, as small drifts of the gold beads between consecutive scans might
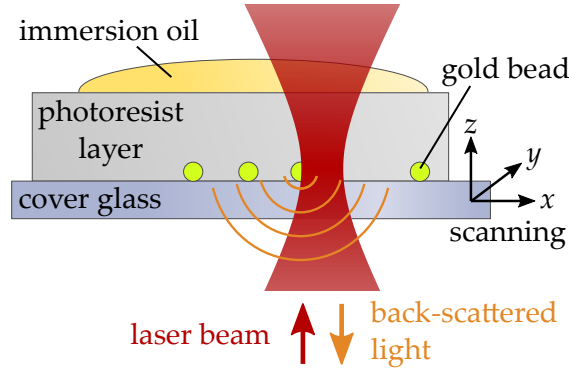
Figure 3.2: Scheme of the laser focus measurement method. A gold bead is scanned through the fixed laser beam. The back-scattered light is collected by the objective lens and recorded on a photodiode. The gold beads are encapsulated in a layer of cured index-matched photoresist to reduce Fresnel reflections from the glass interface. The laser beam and the back-scattered light have the same wavelength but are depicted in different colors for clarity.

impair the results. By using the motorized mirror to shift the excitation beam, the lateral offset between the two foci can be corrected automatically.

3.2.2 HALF-SPACE PHASE MASK

In Section 2.2.1, I have presented several means to create a special depletion focus necessary for STED-inspired lithography. For the experiments conducted in this work, half-space phase masks that work in transmission were used exclusively. These phase masks impose a phase shift of π onto one half-space of the depletion focus (Figure 3.3 a)). Thus, opposite parts of the beam interfere destructively in the center of the focal plane creating a focus that features a plane of zero intensity along one lateral and the axial direction.[1] Figure 3.3 shows results of theoretical calculations of the focal intensity distribution (more precisely $|\vec{E}(\vec{r})|^2$) for this kind of focus. The employed calculation method is explained in detail in Section A.1. The simplicity of this phase mask allows for quick and easy phase mask fabrication

---

[1] The resulting shape is also sometimes referred to as a "hotdog bun".
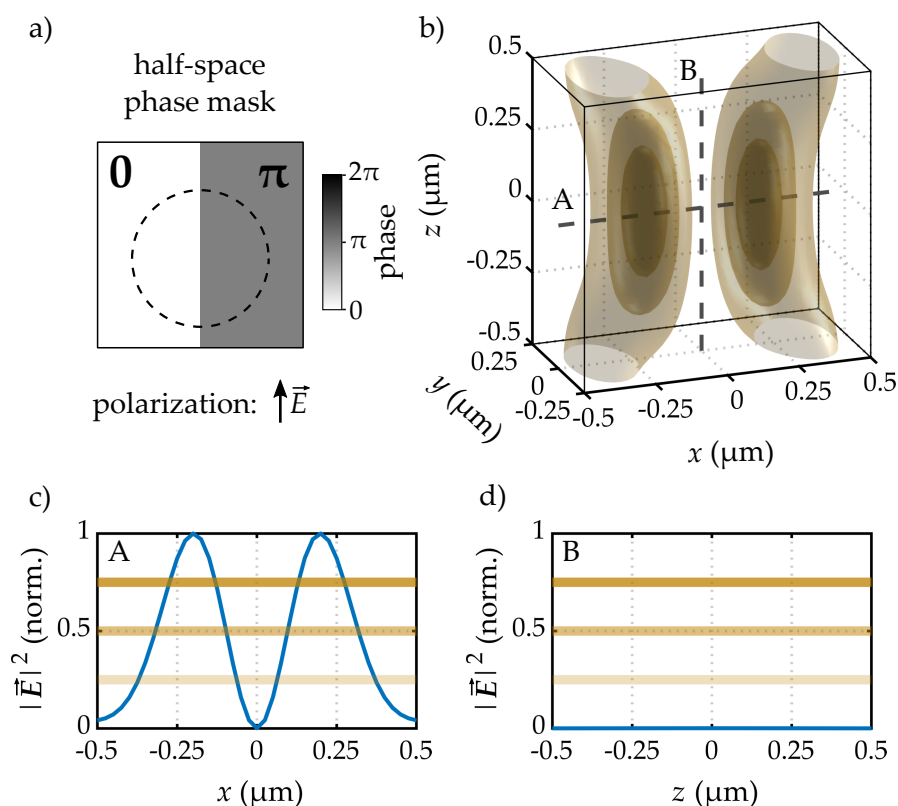
Figure 3.3: a) A transmission phase mask imposes a phase shift of π onto one half-space of the laser beam (beam diameter depicted by dashed line). The edge of the phase mask is parallel to the linear beam polarization. b) Isointensity surfaces of the resulting laser focus calculated for the ideal case depicted for 25 %, 50 %, and 75 % of the peak intensity. c), d) Line cuts denoted by A and B indicate the area of zero intensity in the center of the focus. The calculations assume a wavelength of 640 nm and $NA = 1.4$.

and a convenient beam adjustment that is feasible to be performed on a daily basis. As a trade-off, the depletion is only effective in one lateral direction perpendicular to the plane of zero intensity. While this is a limiting factor for real-world applications, this depletion focus is sufficient to investigate novel photoresist systems and molecular photoswitches as was done in this work. Along the effective direction, feature sizes of less than 20 nm and distances of less than 50 nm have been resolved using such a focus in STED microscopy [95].

Fabrication

The phase masks were fabricated by spin-coating a thin layer of SU-8-5 photoresist (Microchem) onto a plasma-activated cover glass. After prebaking the sample on a hotplate at 90 °C, a mask that covered half of the sample was carefully pressed onto the resist film. The sample was flood-exposed with a UV lamp for 2 min and then post-baked at 90 °C for 1 min. During the post-bake process, the exposed photoresist was cross-linked by cationic polymerization. By developing in mr-Dev 600 (micro resist technology) and blowing with nitrogen, the unexposed resist was removed and the desired phase mask pattern was obtained. The thickness of the final phase mask is determined by the spin speed. To achieve a phase shift of π or $\lambda/2$ in terms of wavelength λ, the thickness d of the phase mask has to fulfill the condition $d = \lambda/(2 \cdot (n-1))$. The refractive index n of the spin-coated film is only known approximately as it depends on the degree of cross-linking and thus on the exact exposure and baking conditions [137]. Therefore, a number of phase masks with varying thicknesses was fabricated and tested in the experimental setup to iteratively optimize the spin-coating parameters towards the ideal thickness.

Alignment

When it comes to alignment of the half-space phase mask, there are a number of degrees of freedom that have different influences on the laser beam focus. Figure 3.4 shows aberrations caused by different types of misalignments which are determined by theoretical calculations. First, the most critical degree of freedom with respect to the intensity minimum is the lateral placement (Figure 3.4 a)). Even a slight shift between the position of the phase mask edge and the center of the collimated Gaussian beam disturbs the destructive interference, leading to a non-zero residual intensity in the center of the focus. In parallel, this leads to a relative shift of the two intensity maxima along the axial direction. Second, the direction of the linear polarization needs to be well aligned in parallel to the edge of the phase mask. Contributions of the orthogonal polarization (or elliptically polarized components) lead to non-zero intensity in the focus center (Figure 3.4 b)). Interestingly, the thickness or the refractive index of the phase mask do
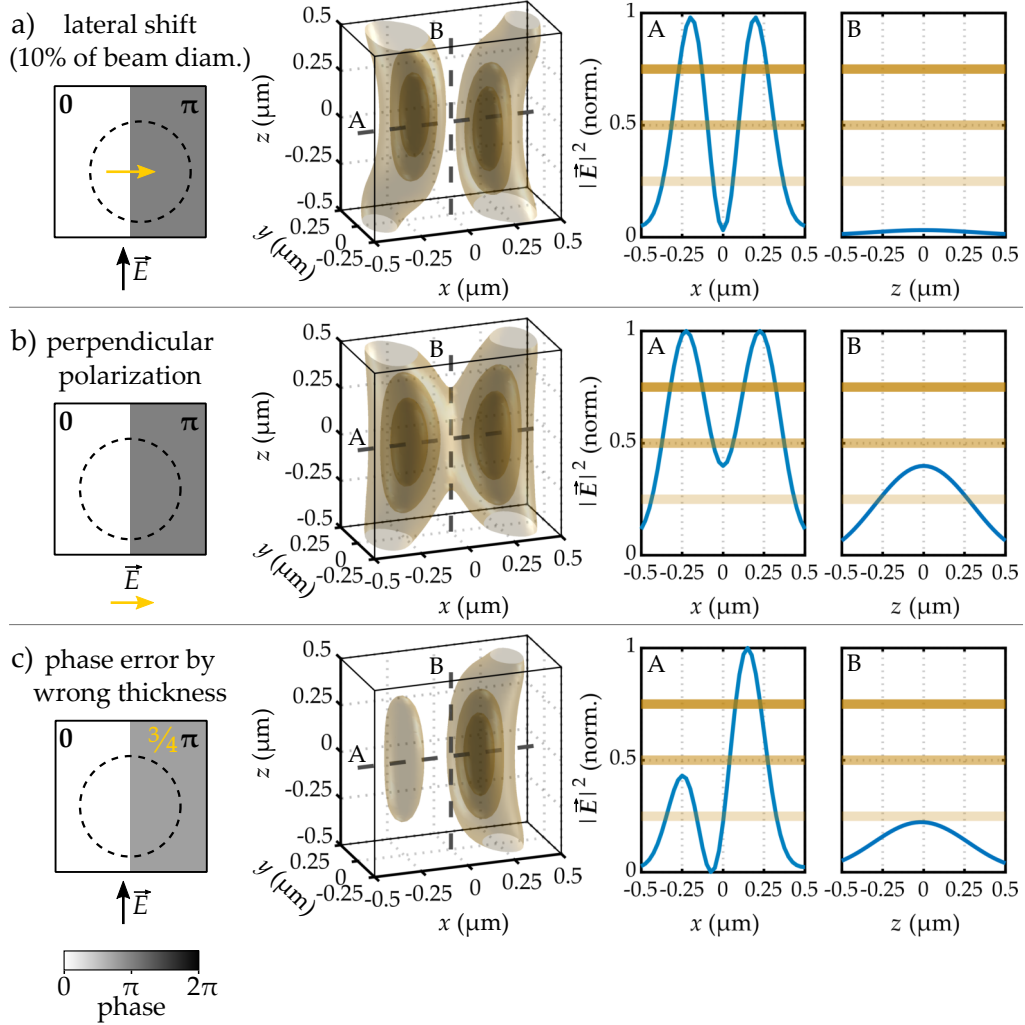
Figure 3.4: Calculations for different cases of phase mask misalignment and the resulting intensity distributions in the focus. a) A lateral shift of the phase mask (10 % of the beam diameter in the depicted example) leads to a distorted focus with finite residual intensity in the minimum. b) If the polarization is oriented perpendicular to the phase mask edge, the residual intensity in the minimum increases considerably. c) An error in phase mask thickness, *i. e.*, phase shift, results in unequal intensity maxima that are still separated by a valley of zero intensity at a laterally shifted position. The calculations assume a wavelength of 640 nm and $NA = 1.4$.

not influence the minimum intensity (Figure 3.4 c)). Instead, a non-ideal optical path difference leads to an asymmetry in the lateral direction. The two intensity maxima end up with unequal peak intensities.

3.2.3 LASER FOCI EMPLOYED IN THIS WORK

Depending on the employed photoswitch material and the purpose of the experiment, different excitation and depletion laser foci were used for the experiments presented this thesis. Generally, the excitation laser was always employed in a diffraction-limited Gaussian focus. For some experiments, the depletion laser was used in a Gaussian mode as well. In that case, it was intentionally widened to match the width of the excitation beam by introducing a partially closed aperture into the depletion beam path (see Section 3.1). This scheme is referred to as *global depletion* and was mainly employed for characterizing the depletion effects observed in the different systems. The aperture was replaced by the half-space phase mask mentioned above for experiments where a linewidth enhancement or a resolution increase was intended to be investigated. The measured foci employed for experiments on the methylbenzaldehyde chromophore (see Chapter 4) with two-photon excitation at 700 nm and depletion at 440 nm are shown in Figure 3.5. In experiments with the spirothiopyran chromophore (see Chapter 5) using two-photon excitation at 820 nm and depletion at 640 nm, the foci depicted in Figure 3.6 were employed.
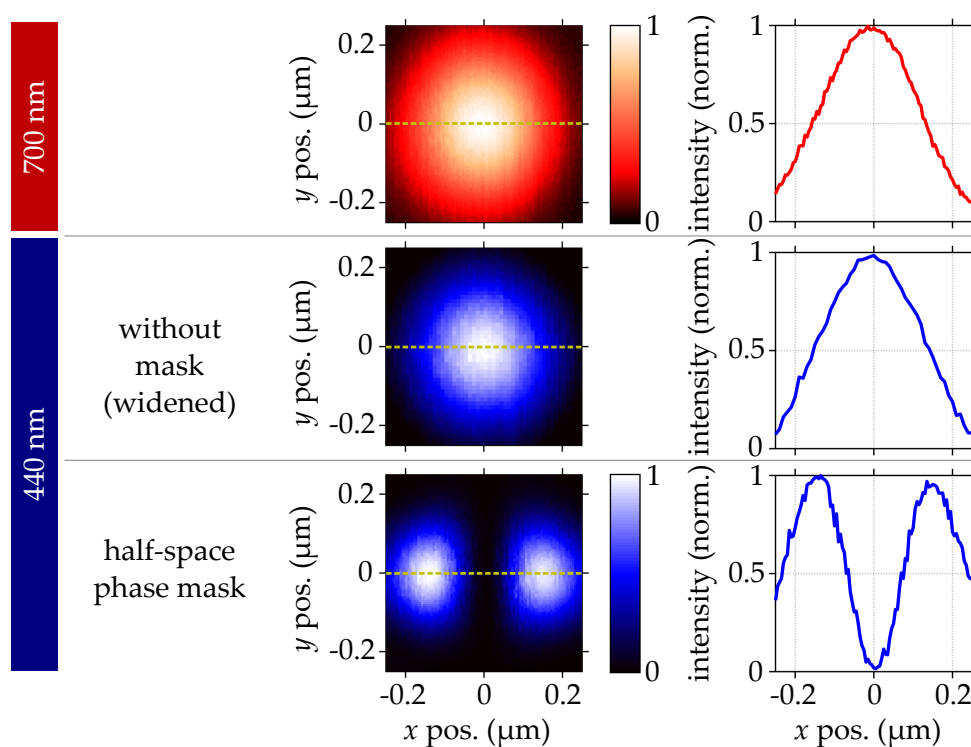
Figure 3.5: False-color plots of the laser focus point-spread functions used for the photoenol system based on the methylbenzaldehyde chromophore, measured by gold bead scattering experiments. Both laser beams can be employed in a Gaussian shape, where the depletion laser at 440 nm is intentionally slightly widened to match the beam width of the excitation laser at 700 nm. The depletion laser can be modified by introducing a half-space phase mask, imposing a line of zero intensity onto the focus. Intensity profiles along the dashed lines are shown on the right, respectively. Adapted from [138].
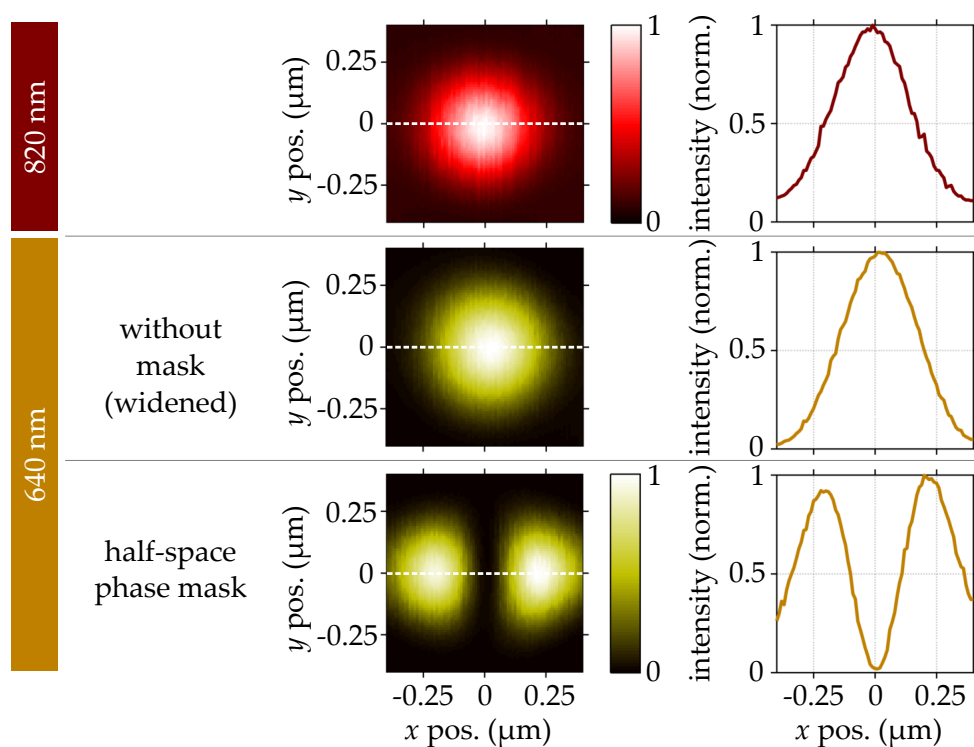
Figure 3.6: False-color plots of the laser focus point-spread functions used for the spirothiopyran chromophore measured by gold bead scattering experiments. Both laser beams can be employed in a Gaussian shape, where the depletion laser at 640 nm is intentionally slightly widened to match the beam width of the excitation laser at 820 nm. The depletion laser can be modified by introducing a half-space phase mask, imposing a line of zero intensity onto the focus. Intensity profiles along the dashed lines are shown on the right, respectively. Adapted from [139].

3.3 Sample Processing Workflows

In the experimental part of this thesis, samples were processed according to one of two different workflows. In this section, I describe these workflows in a very general way. Depending on the investigated chromophore, the materials and wavelengths differ and are described in detail in the corresponding chapters.

3.3.1 Surface Functionalization

In this approach, the chromophores, either methylbenzaldehyde or spirothiopyran, were fixed onto a glass surface, while a maleimide species was supplied in solution. By 2D laser lithography, chromophores were excited in areas defined by the exposed patterns and subsequently reacted with maleimides, leading to spatially resolved surface functionalization. The processing steps are depicted in Figure 3.7 and described in the following.

Silanization

A specifically synthesized silane species carrying the photoactive chromophore was covalently bound onto the glass substrate *via* silanization (Figure 3.7 a)). Therefore, a $1 \, \mathrm{mmol \, L^{-1}}$ solution of the silane in anhydrous toluene was prepared. A standard microscopy cover glass ($22 \, \mathrm{mm} \times 22 \, \mathrm{mm}$, $170 \, \mathrm{\mu m}$ thickness) was thoroughly cleaned and activated by oxygen plasma treatment for $15 \, \mathrm{min}$, before being immersed into the silane solution. After $4 \, \mathrm{h}$, the substrate was immersed in toluene for $30 \, \mathrm{min}$, followed by rinsing with acetone, isopropyl alcohol, and deionized water, and drying in a stream of nitrogen.

2D Laser Lithography

The reaction partner for both investigated chromophores was a bromine-carrying maleimide which was dissolved at a concentration of $1 \, \mathrm{mmol \, L^{-1}}$ and added as a droplet resting on top of the sample during the laser lithography step (Figure 3.7 b)). For the photoenol system, dimethylformamide (DMF) was used as solvent, while dimethylsulfoxide (DMSO) was utilized
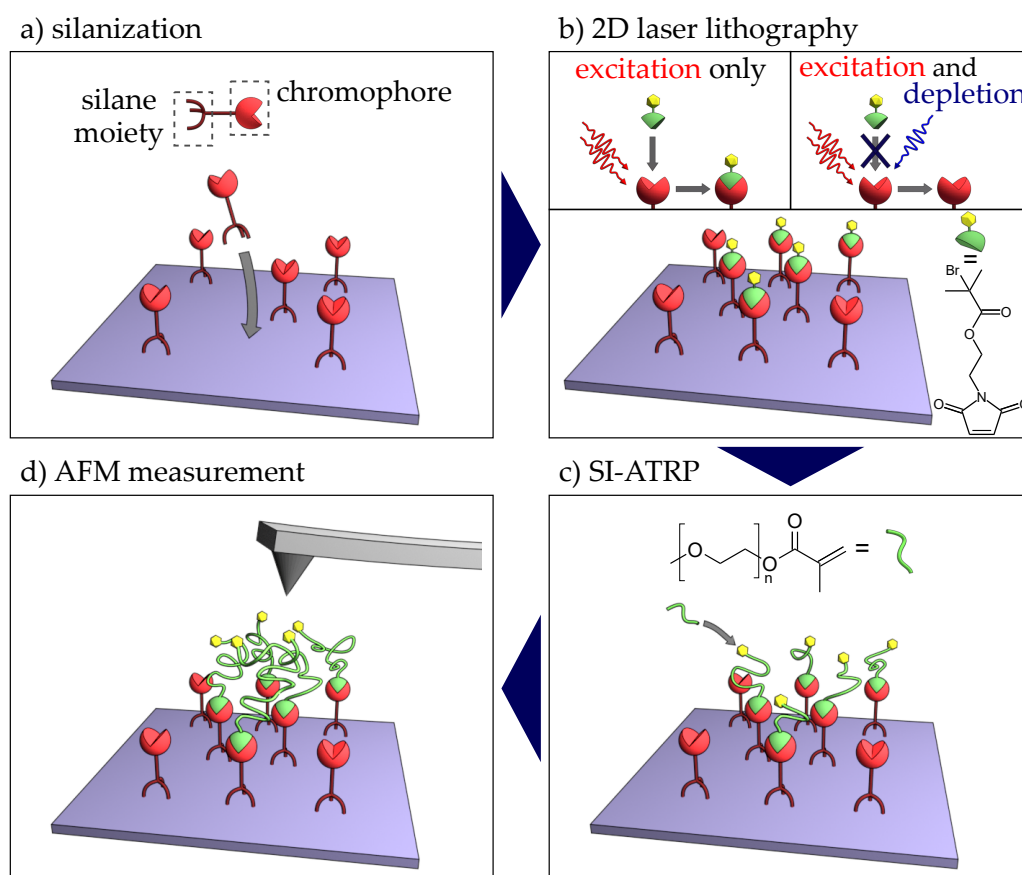
Figure 3.7: Schematic workflow for surface functionalization by STED-inspired lithography. a) A plasma-activated glass sample is silanized by immersion into a solution containing a silane moiety bearing the chromophore. b) The sample is functionalized selectively by laser lithography. In areas solely exposed to the excitation laser, the two-photon-activated chromophores react with bromine-carrying maleimide derivatives. In contrast, the reaction is suppressed in areas that are simultaneously exposed to the depletion light. c) Initiated by the bromine moiety, poly(ethylene glycol) methyl ether methacrylate brushes are grown from the functionalized areas by surface-initiated atom transfer polymerization (SI-ATRP). d) The sample is characterized by atomic-force microscopy (AFM). Adapted from [138].

for the spirothiopyran chromophore. The solution was held in place by a PDMS ring. Writing experiments were performed by scanning the sample through the fixed laser foci while modulating the laser powers to excite the chromophores. The maleimide moieties react with the photoactivated chromophores by either Diels-Alder cycloaddition or thiol-Michael addition (see Sections 4.2 or 5.2). Thus, in the areas that were exposed solely to the excitation laser, bromine was covalently bound to the surface. In areas that saw both excitation and depletion light simultaneously, the reaction was suppressed as a portion of the photoreactive species was deactivated again by the depletion laser. As a result, the substrate surface was functionalized with an area density that spatially varied following the lithographically defined patterns. After fabrication, samples were rinsed with DMF or DMSO, respectively, followed by acetone, isopropyl alcohol, and deionized water, and dried in a stream of nitrogen.

Surface-initiated Atom Transfer Radical Polymerization

After lithography, the bromine groups were used as initiators for growing polymer brushes by surface-initiated atom transfer radical polymerization (SI-ATRP) [140] (Figure 3.7 c)). The polymerization thereby proceeds *via* controlled radical polymerization with a comparatively slow speed as the dynamic equilibrium of the reaction is strongly shifted towards a dormant species. The technique offers precise control over molecular weight, dispersity, and composition of the grown polymer. In this work, SI-ATRP was performed according to a previously reported procedure [141]. The samples were transfered into a reaction vial that was subsequently flushed with nitrogen. A solution was prepared consisting of 2,2'-dipyridine (435 mg), poly(ethylene glycol) methyl ether methacrylate (PEGMEMA, 8.5 g, $M_\mathrm{n} = 300\,\mathrm{g\,mol^{-1}}$, previously deinhibited by passing through a basic alumina column), $CuBr_2$ (12.2 mg), and CuCl (80 mg) in water:methanol (1 : 1 vol%). The solution was degassed by nitrogen bubbling for 1 h and transferred into the reaction vial, starting the polymerization reaction by heating to 60 °C. After 45 min, the samples were removed, thoroughly rinsed with methanol, deionzed water, and DMF, and dried in a stream of nitrogen.

Atomic Force Microscopy (AFM)

By growing polymer brushes by SI-ATRP, the surface functionalization was rendered measurable by atomic force microscopy (AFM) (Figure 3.7 d)). A compact AFM instrument (Easyscan 2, Nanosurf) was equipped with precision cantilevers (PPP-NCLR, Nanosensors) with a tip radius of $<7\,$nm. The device was operated in intermittent contact mode. Feedback loop parameters were individually adapted to optimize the images. The software Gwyddion was used for post-processing the images, *e. g.*, subtracting constant z-offsets and correcting for sample tilt or scan field bow.

In principle, the functional group on the maleimide species can be chosen arbitrarily, enabling different applications of the described surface functionalization technique (not necessarily involving SI-ATRP and AFM). Some examples are described in Section 4.2.2. However, for investigating diffraction-unlimited laser lithography, the procedure described above proved to be most insightful. While surface functionalization is limited to creating 2D structures on the substrate surface, there are two advantages concerning the characterization of the depletion mechanism: First, the chromophores are fixed on the surface which eliminates diffusion effects blurring the results. Secondly, the photo-induced linkage is separated from the polymerization (or more general, network formation). Therefore, it is possible to obtain a clearer view on the behavior of the chromophore as compared to when both processes take place simultaneously.

3.3.2 WRITING OF NEGATIVE-TONE 3D PHOTORESISTS

This approach resembles the standard process of DLW as described in Section 2.1. Figure 3.8 schematically shows the processing steps. Here, methacrylate copolymers were synthesized that bear the respective chromophore as side groups. Again, details on the materials and the cross-linking mechanisms are given in the corresponding sections. A solution containing the copolymer was prepared, yielding a liquid photoresist. The photoresist was applied onto a cleaned cover glass and inserted into the lithography setup. The desired patterns were serially fabricated by scanning the sample relative to the fixed foci. Volumes that were exposed to the excitation laser
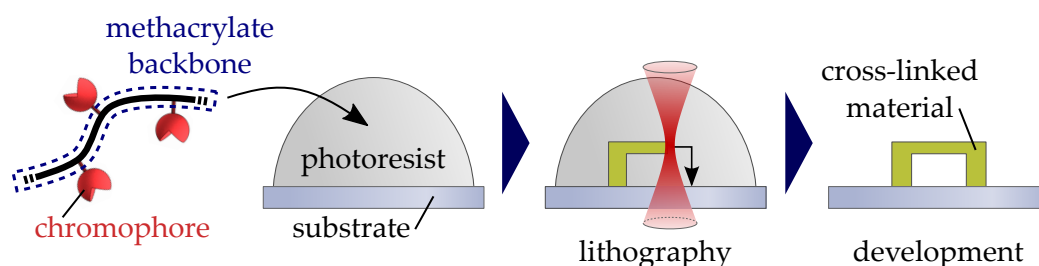
Figure 3.8: Schematic view of the workflow for processing 3D photoresists. Methacrylate copolymers bear the photoactive chromophores to be investigated as side groups. A liquid photoresist is prepared and applied onto a glass substrate. The desired structures are written by laser lithography, where cross-linking by the excitation laser can be suppressed by simultaneous exposure with the depletion laser (not depicted). After exposure, the unexposed, still liquid photoresist is removed in a development step, obtaining the cross-linked structures. Adapted from [139].

underwent cross-linking, *i.e.*, were written. In contrast, cross-linking was suppressed by the depletion effect in volumes that were simultaneously exposed to both excitation and depletion laser. After exposure, the samples were developed in toluene for 2–5 min (depending on the resist viscosity), followed by immersion in isopropyl alcohol for 1 min, and blowing with nitrogen. Written structures were typically inspected by light microscopy or scanning electron microscopy.

Scanning Electron Microscopy (SEM)

Samples were glued onto a sample holder using conductive silver paste. A thin layer of gold with a thickness of typically 5 nm was sputtered onto the samples using a sputter coater (108auto, Cressington). The written structures were inspected with an Ultra Plus SEM (Zeiss), typically using an acceleration voltage of 5 kV and an aperture with a diameter of 20 µm. For quasi-2D structures on the substrate surface, the in-lens detector was employed. The secondary electron detector was used for oblique views on 3D structures.

4

THE PHOTOENOL
MOLECULAR PHOTOSWITCH
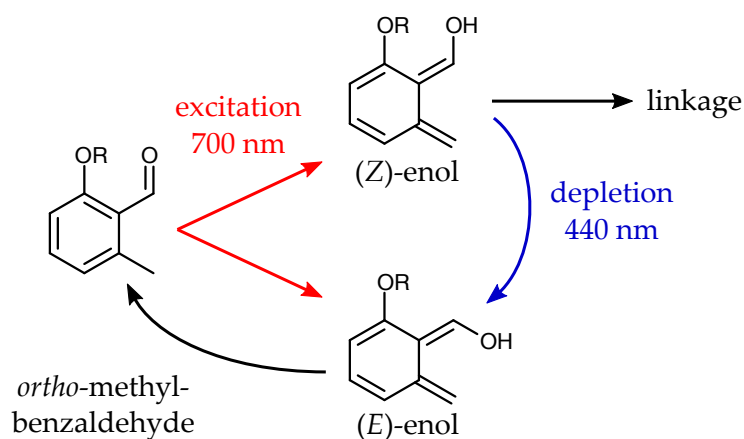
Schematic view of the photoswitch introduced in this chapter.

In this chapter, a molecular photoswitch is introduced that is based on photoisomerization of intermediate-state photoenols. The fundamentals of photoenol chemistry and reaction pathways are reviewed. I describe an approach for spatially resolved surface functionalization that allowed to achieve sub-diffraction resolution and to obtain insights on the photoenol photoswitch. Moreover, I introduce a negative-tone photoresist that is based on methacrylate copolymers and allowed for fabrication of 3D structures. Experiments on writing inhibition by depletion and its limitations are discussed.

4.1 Fundamentals of Photoenol Chemistry

The photochemical generation of highly reactive enol intermediates from *ortho*-alkylphenylketones or -aldehydes, commonly referred to as *photoenolization* [142], has proven to provide a versatile route to light-triggered chemical ligation. *Ortho*-methylbenzaldehyde (*o*-MBA) chromophores have been employed as photoremovable protecting groups, *e. g.* for the photorelease of acids or alcohols [143, 144] and more recently also for readily generating highly reactive *ortho*-quinodimethanes, which found numerous applications in polymer photochemistry [145]. The most utilized reaction pathway here is Diels-Alder trapping, *i. e.*, a $[4 + 2]$ cycloaddition reaction with an activated dienophile, which I describe in more detail below. The system was utilized for the photochemical synthesis of polyimides [146] and block copolymers [147, 148], the formation of conjugated polymer networks [61] as well as spatially resolved surface functionalization [149].

In the context of multi-photon laser lithography, Diels-Alder trapping of photoenols was employed for spatially resolved post-modification of the surface of direct-laser written 3D structures [53] and orthogonal modification of microscopic cell scaffolds [150], allowing for selective cell attachment [151] for studies on manipulations of individual cells. In a different study, DNA arrays bearing *o*-MBA chromophores were patterned onto maleimide-functionalized surfaces, allowing for further encoding of fluorescent markers or proteins [152]. By using different oligonucleotide sequences, orthogonal surface functionalization was demonstrated by exploiting the high degree of selectivity in DNA hybridization. Furthermore, Quick and coworkers introduced a 3D-capable photoresist based on Diels-Alder cross-linking of a small 4-arm molecule carrying *o*-MBA moieties and methacrylate copolymers with maleimide functionalities as side groups [136]. It was possible to further functionalize the fabricated 3D structures in a similar way to the cell scaffolds mentioned above by using unreacted *o*-MBA moieties on the structure for immobilization of maleimides. A similar approach relied on using reversible activation fragmentation chain transfer (RAFT) polymerization for the synthesis of 4-arm star polymers bearing *o*-MBA chromophores [153]. In combination with maleimide-carrying methacrylate copolymer, a photoresist was prepared that allowed for fabrication of 3D structures. Potentially,

the high degree of flexibility in RAFT polymerization allows for tayloring material properties by adapting the backbone of the 4-arm star polymers.

A common observation across all publications using two-photon excitation of *o*-MBA chromophores is the necessity of using light at shorter wavelengths than in standard DLW where typically h- or i-line photoinitiators are used [19]. The reason is that the (one-photon) absorption of the *o*-MBA chromophore only sets in at wavelengths smaller than 350 nm [154, 155]. The one-photon absorption spectrum cannot necessarily be translated into the two-photon absorption spectrum by simply multiplying the wavelength by 2. However, in practice, at least the spectral positions of the absorption peaks largely follow this rule [19].

In the following, I explain in more detail the underlying chemistry leading to generation of photoenols, their reaction pathways and how photoisomerization can constitute a molecular photoswitch for sub-diffraction laser lithography.

4.1.1 PHOTOENOLIZATION OF METHYLBENZALDEHYDES

Ortho-alkylphenylketones or -aldehydes can appear in two different tautomeric forms referred to as keto and enol. At room temperature, the keto form predominates in equilibrium. When exposed to UV light, these molecules undergo light-driven tautomerization leading to the formation of the enol species, therefore also called *photoenols*. Photoenols are intermediates that eventually revert to the keto ground state. In this work, we specifically investigate photoenols generated from *ortho*-methylbenzaldehyde. The process of photoenolization is shown in Figure 4.1. By absorption of UV light, *o*-MBA transits into its excited singlet state followed by intersystem crossing into its triplet state. By 1,5-hydrogen transfer under participation of the methyl group in *ortho* position, a biradical species is formed. After typically some tens of nanoseconds, the radicals recombine with the delocalized π-electrons of the aromatic ring, forming an (photo)enol species under loss of aromaticity. Depending on bond rotations during this process, the photoenol is present in one of the two isomeric configurations, (*E*)-enol (*trans*) or (*Z*)-enol (*cis*).

The lifetimes of the two isomers typically differ by at least two orders
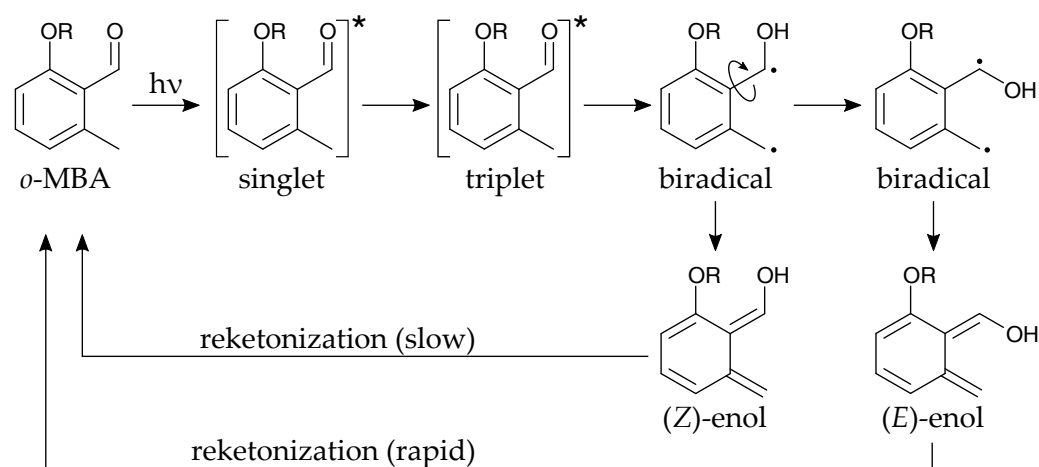
Figure 4.1: UV light excites *ortho*-methylbenzaldehyde into the singlet state, followed by intersystem crossing into the triplet state. By hydrogen transfer a biradical is formed, that eventually leads to formation of (*Z*)-enol or (*E*)-enol, depending on the bond rotation in the biradical state. Both photoenols are intermediates, that revert to the *o*-MBA ground state by reketonization, but their lifetimes differ substantially.

of magnitude, depending on the solvent. For small molecules in benzene, lifetimes of 10 ms (*Z*) and 225 ns (*E*) were reported [156][1]. The generated photoenol species belong to the class of *ortho*-quinodimethanes, a very reactive functional group. Thus, the long-lived (*Z*)-enol is present long enough to undergo chemical reactions with other components. On the other hand, the short-lived (*E*)-enol exclusively reketonizes[2] *via* reverse hydrogen transfer, reforming *o*-MBA [157]. Possible reactions of the intermediate state (*Z*)-enol will be described in the following.

---

[1] Note that the naming convention is independent of the lifetimes but follows from Cahn–Ingold–Prelog priority rules which are applied in this thesis. In our publication on photoenol-based STED-inspired lithography [138], we followed a different convention which explains why the roles of (*E*)-enol and (*Z*)-enol seem to be interchanged in comparison to this thesis.

[2] While, strictly speaking, *reketonization* means reformation of alkylphenyl*ketones*, the term is also applied to alkylphenylaldehydes by literature convention.

electrocyclic ring closure

Diels-Alder cycloaddition

b)

c)

a)

(Z)-enol

d)

o-MBA
reketonization

[4+4] dimerization
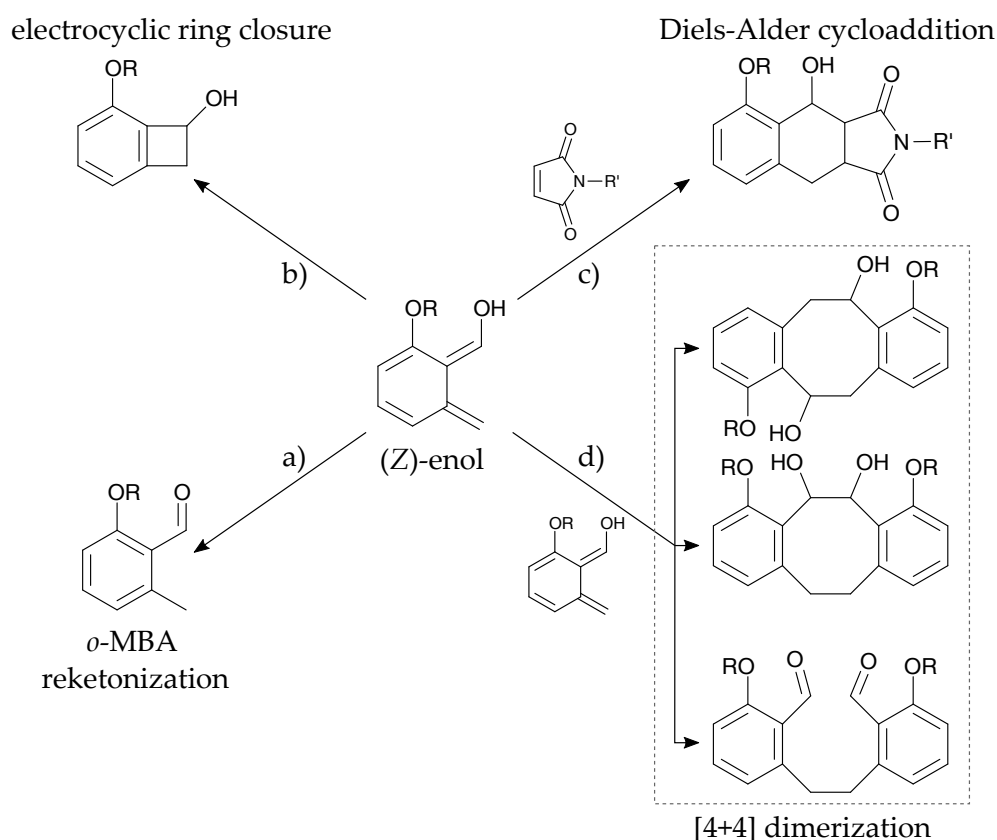
Figure 4.2: Different reaction pathways of (Z)-enols. a) Reketonization reforming the *ortho*-methylbenzaldehyde. b) Electrocyclic ring closure leading to benzocyclobutenol. c) Diels-Alder cycloaddition of a maleimide forming a stable cycloadduct. d) Self-dimerization generating different [4 + 4] cycloadducts.

4.1.2 REACTION PATHWAYS OF INTERMEDIATE-STATE PHOTOENOLS

Typically, *ortho*-quinodimethanes can undergo different chemical reactions which are shown in Figure 4.2 for the case of a (Z)-enol generated from *o*-MBA. One possibility is the reketonization that was already mentioned in the last section. Here, reverse hydrogen transfer of the hydroxyl proton recreates the starting product *o*-MBA (Figure 4.2 a)). Another less likely pathway that does not require a second molecule is electrocyclic ring closure as depicted in Figure 4.2 b) [158]. In the presence of activated dienophile

such as a maleimide, the (Z)-enol can undergo a Diels-Alder cycloaddition resulting in a stable cycloadduct (Figure 4.2 c)). Diels-Alder cycloadditions are very efficient at room temperature, show high reaction yields largely independent of reaction conditions and provide high selectivity, *i.e.*, no byproducts are formed. Furthermore, the reaction products are very stable as the aromaticity of the benzaldehyde ring is restored [159]. Thus, this reaction classifies as a so-called *click* reaction, a versatile class of chemical reactions widely used in material science [160, 161]. The Diels-Alder reaction not only constitutes the underlying mechanism for all of the preceding work on photoenol-based laser lithography described above, but is also employed herein for sub-diffraction surface functionalization in Section 4.2 below. While dienophilic reaction partners are available, the Diels-Alder reaction dominates all other reaction channels for the long-lived (Z)-enol. If such dienophiles are absent but instead (Z)-enols are present at a high concentration, self-dimerization is a likely reaction pathway [142]. Here, different products can be obtained, namely $[4+2]$ or $[4+4]$ cycloadducts. A recent study on small molecules in solution determined the three $[4+4]$ adducts depicted in Figure 4.2 d) to be the main reaction products with a combined yield of approximately 80 % [162]. The 3D photoresist presented in Section 4.3 is based on this cross-linking mechanism.

4.1.3 EFFECTIVE DEPLETION BY *Cis-Trans* ISOMERIZATION

In 1991, Netto-Ferreira and Scaiano reported on *cis-trans* photoisomerization of intermediate-state photoenols from *o*-MBA, *i.e.*, the light-triggered conversion from (Z)-enol to (E)-enol, at a wavelength of 420 nm [163]. This discovery opened up the possibility to adopt the *o*-MBA chromophore for STED-inspired laser lithography. As mentioned above, only the long-lived (Z)-enol can effectively participate in chemical reactions with other molecules by Diels-Alder cycloaddition or dimerization, while the short-lived (E)-enol rapidly transits back into the *o*-MBA ground state. Thus, a light-triggered conversion of (Z)-enol to (E)-enol leads to a suppression of subsequent reactions by depleting the population of (Z)-enols. Therefore, a molecular photoswitch is constituted by the light-triggered switching between *o*-MBA and (Z)-enol, as depicted in Figure 4.3 a). To refer to the scheme of the
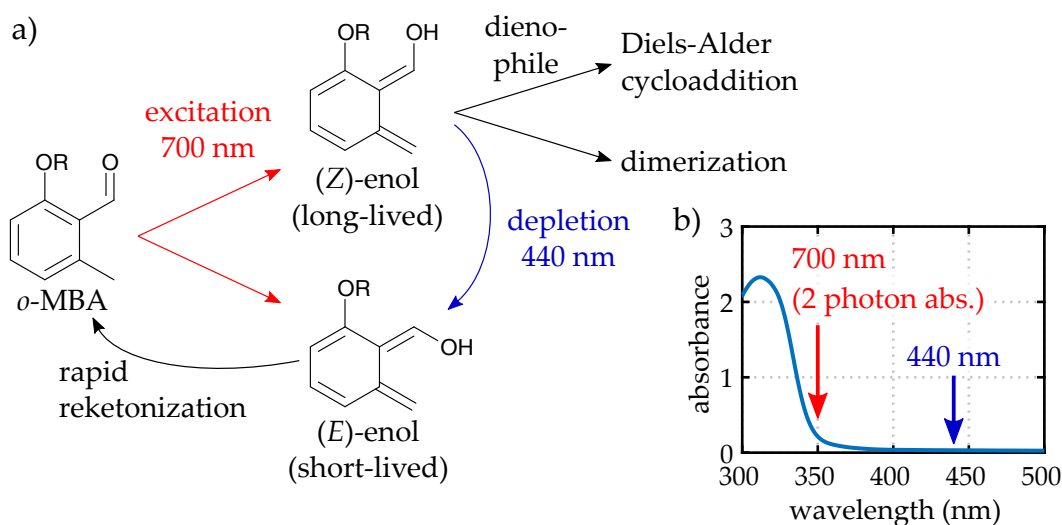
Figure 4.3: a) Principle of the molecular photoswitch employed for STED-inspired laser lithography. (*Z*)-enol generated by two-photon excitation of *ortho*-methylbenzaldehyde (*o*-MBA) at 700 nm can undergo photoisomerization into (*E*)-enol by exposure to light at 440 nm. The short-lived (*E*)-enol then rapidly reketonizes, reforming *o*-MBA. Thereby, the population of (*Z*)-enols is effectively depleted, averting further reactions such as Diels-Alder cycloaddition or dimerization. b) The absorption spectrum of *o*-MBA (copolymer **PE-1** (see Section 4.3), $1 \, \text{mg} \, \text{ml}^{-1}$ in acetonitrile). The employed wavelengths for two-photon excitation and one-photon depletion are indicated.

ideal molecular photoswitch introduced in Section 2.2.2, *o*-MBA represents the ground state A, (*Z*)-enol represents excited intermediate state B and the reaction product, *i. e.*, one of the different cycloadducts, represents state C. Excitation takes place by two-photon absorption of femtosecond laser pulses at a center wavelength of 700 nm. This wavelength is a compromise. Two-photon excitation of *o*-MBA would be more efficient at shorter wavelengths as the corresponding one-photon absorption band peaks at 312 nm (Figure 4.3 b)). However, the tuning range of the employed titanium-sapphire laser is limited. In the past, two-photon excitation at 700 nm proved suitable for the *o*-MBA chromophore [136]. For depletion, a continuous-wave diode laser at 440 nm is employed. This wavelength is well separated from the one-photon absorption band but still efficiently triggers photoisomerization.

Later reports in literature also found evidence for photoisomerization occurring in both directions, *i. e.*, also in the reverse direction from (*E*)-enol to (*Z*)-enol [156]. In that case, the (*Z*)-enol population is still effectively depleted as the concentration of (*E*)-enol can be assumed to be zero due to the rapid reketonization process. Thus, no considerable (*Z*)-enol formation occurs by irradiation with the depletion light. In both cases the concept remains applicable for STED-inspired laser lithography.

This concept was developed within our group and led to a patent application [164]. The authors conducted proof-of-principle experiments using optics with low numerical aperture which were published in the thesis of Alexander Quick [165].

4.2 Sub-Diffraction Surface Functionalization

In this section, I describe experiments on STED-inspired laser lithography that enabled covalent surface functionalization with sub-diffraction resolution. While Diels-Alder cycloaddition of photoenols was already employed for surface functionalization in the past [149], the achieved resolution and feature sizes were considerably above the diffraction limit and not limited by optics [53]. Clearly, a key requirement for conducting high resolution experiments is to render the surface functionalization measurable by a technique that can resolve features beyond the diffraction limit of conventional confocal microscopy. This was achieved herein by growing polymer brushes onto the functionalized areas that can be characterized by AFM. The work presented in this section was presented at a conference [166] and published in a peer-reviewed journal article [138]. As long as not indicated otherwise, I conducted the experimental work presented in this section including sample preparation, processing, and characterization. The co-authors of these publications performed preliminary experiments in preparation for this work and participated in interpretation of the experimental data.

For sample preparation, we followed the experimental procedure described in detail in Section 3.3.1. A triethoxysilane bearing the o-MBA chromophore was prepared by Thomas Paulöhrl and Markus Zieger (ITCP, KIT) following a literature procedure [149] (Figure 4.4 a)). Bromine-carrying maleimide (Figure 4.4 b)) synthesized by Alexander Quick (ITCP, KIT) according to literature [141] was dissolved in DMF at a concentration of $1\,\mathrm{mmol\,L^{-1}}$ and applied onto the sample in the laser lithography step. To relate to the previous section, the R and R′ group in Figure 4.2 c) were chosen to be triethoxysilane and a moiety containing bromine respectively. The lithography setup described in Section 3.1 was configured to $700\,\mathrm{nm}$ excitation and $440\,\mathrm{nm}$ depletion wavelength. A scan speed of $10\,\mathrm{\mu m\,s^{-1}}$ was used for exposure. Thus, the o-MBA chromophores on the substrate were excited by two-photon absorption at $700\,\mathrm{nm}$, leading to photoenol formation. Areas that were exposed with solely the excitation light were covalently functionalized with bromine by Diels-Alder cycloaddition of (Z)-enol and maleimide. The bromine density on the surface followed the exposure dose profile. In areas that saw both excitation and depletion light, the reaction

a)

b)

benzaldehyde-silane   maleimide-bromine
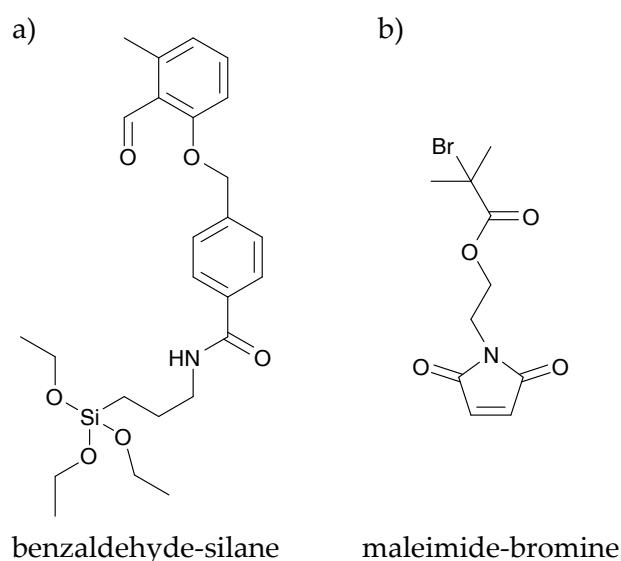
Figure 4.4: a) The *o*-MBA-carrying triethoxysilane species used for coating of the glass surface *via* silanization. b) The maleimide species bearing a bromine group used as polymerization initiator.

was suppressed by the depletion effect. Compared to standard DLW using 3D photoresists, there exists no pronounced threshold behavior, *i. e.*, lower excitation intensities lead to lower functionalization densities without a clear cut-off. In the development step, samples were thoroughly rinsed with DMF, acetone, isopropyl alcohol, and deionzed water to avoid unspecific binding of bromine groups in unexposed regions. PEGMEMA polymer brushes were grown by SI-ATRP using the bromine groups as initiators and characterized by AFM.

Saturation Effects

In first writing experiments using only the excitation beam in a Gaussian mode, sets of polymer brushes were written with increasing laser power. AFM images of the results and derived graphs are depicted in Figure 4.5. The height of surface-grown polymer brushes is reported to relate linearly to the area density of bromine groups, *i. e.*, polymerization initiators, on the surface because the conformation of individual brushes is influenced by the presence of adjacent brushes [167, 168]. This allows to relate the height information
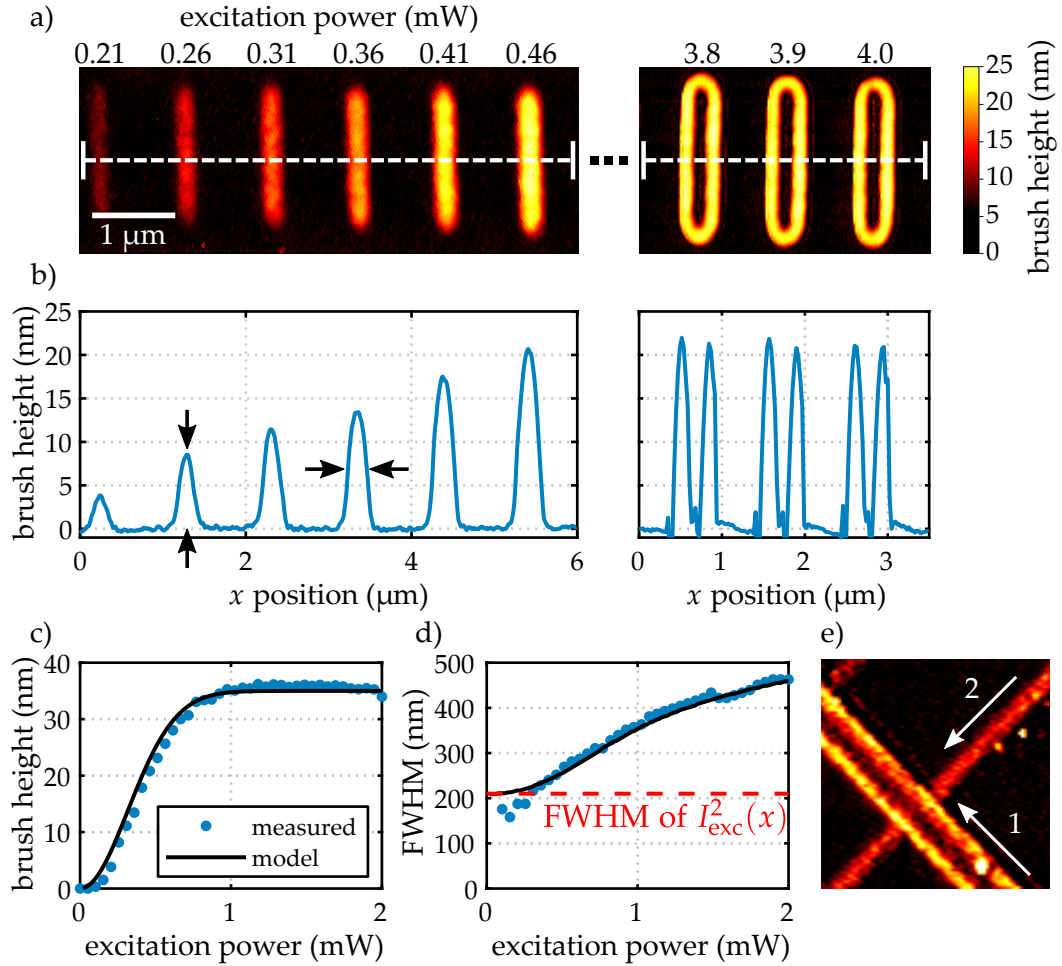
Figure 4.5: a) AFM images of a set of polymer brushes written with increasing excitation laser power. At high powers, the height is decreased again in the center of the lines. b) Line cuts through the data are used to determine height and full width at half maximum (FWHM) for each line. c) For excitation powers below 0.5 mW, the brush height increases with the square of the excitation power before saturation effects arise. d) The FWHM of the brushes exceed the lower limit given by the squared intensity distribution of the excitation laser. The results of a simple rate equation model describing the data is drawn in black in panels c) and d). e) The minimum on a line written with a high laser power (1) can not be filled again by a second pass at a lower power (2). Adapted from [138].

gained in AFM measurements directly to the initiator density and thus to the effective exposure dose of the lithography step. Ideally, in a system without any threshold, one would expect the line shape to follow exactly the intensity distribution of the excitation focus squared, as a two-photon process is present (panel b)). Clearly, a high grafting density of the silane on the glass surface is favorable as this enables a high density of initiators, and thereby also higher polymer brushes. However, the silane grafting density is finite and therefore saturation effects can occur. As shown in Figure 4.5 c), the height of the polymer brushes increases with the square of the excitation laser power until a saturation level is reached, which leads to deviations of the line shape. Therefore, the full width at half maximum (FWHM) of the squared excitation intensity is only a lower limit to the achievable linewidth in the case of depletion being switched off (panel d)). The saturation behavior can be reproduced using a simple rate equation model, that will be explained in more detail below. For higher excitation powers deep in the saturation regime, another limiting factor becomes apparent. The height in the center of the lines decreases again, while the edges keep the height corresponding to the saturation level. This effect is irreversible as it was not possible to write through such an area again afterwards. Instead, the surface remained empty as shown in Figure 4.5 e). We attribute this effect to irreversible destruction of the o-MBA chromophores by the excitation laser.

A Rate Equation Model for 2D Laser Lithography

For modeling our experiments on surface functionalization, we need to develop a basic understanding on how the exposure to the lasers translates into a initiator density profile on the sample surface. Therefore, we employ a simple rate equation model along the lines of the model derived in Section 2.2.2 describing a molecular photoswitch. We need two simplifying assumptions. First, we assume that the population of (E)-enol is zero at any given time due to its short lifetime. Second, we assume that the (Z)-enol population is eventually fully converted into the cycloadduct, *i.e.*, no reketonization or side reactions take place. These assumptions are well satisfied given a high concentration of maleimide species. Therefore, the system can be modeled as an effective two-level system. The ground state population, *i.e.*, the unexcited o-MBA, is denoted by $N_G(x,t)$. The excited state population, *i.e.*, the (Z)-enol,
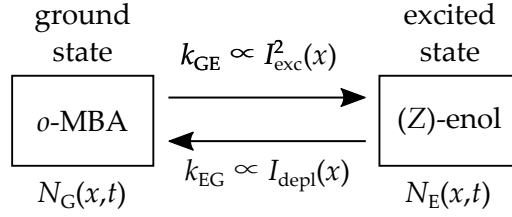
Figure 4.6: Scheme of the two-level rate equation model used for numerical reproduction of the measured data.

is denoted by $N_E(x, t)$. Figure 4.6 shows that the space-dependent transition rate k_{GE} from ground state to the excited state is assumed to be proportional to the squared excitation intensity profile $I_{exc}^2(x)$, as a two-photon process is present. The reverse transition rate k_{EG} is assumed to be proportional to the depletion intensity profile $I_{depl}(x)$. Populations and intensities are normalized to 1. Under the boundary condition $N_E(x, 0) = 0$, *i.e.*, there are initially no excited species, the solution to the resulting system of differential equations is given by

$$N_E(x, t) = \frac{1}{k_{GE} + k_{EG}} \cdot k_{GE} \cdot \left(1 - e^{(k_{EG} + k_{GE})t} \right) . \tag{4.1}$$

The laser focus intensity distributions are modeled by the analytical functions

$$I_{exc}(x) = \exp \left(-\frac{x^2}{2\sigma_{exc}^2} \right) \tag{4.2}$$

and

$$I_{depl}(x) = \exp \left(-\frac{x^2}{2\sigma_{depl}^2} \right) \cdot x^2 , \tag{4.3}$$

where the values of $\sigma_{exc} = 0.1254\,\mu m$ and $\sigma_{depl} = 0.1079\,\mu m$ are obtained from fits to line cuts through the measured foci (Figure 3.5). The term x^2 in Equation 4.3 superimposes a parabolic minimum onto the center of the depletion focus. We assume the initiator profile after exposure to be proportional to $N_E(x)$ which, scaled by a constant factor, yields the polymer brush height profile.
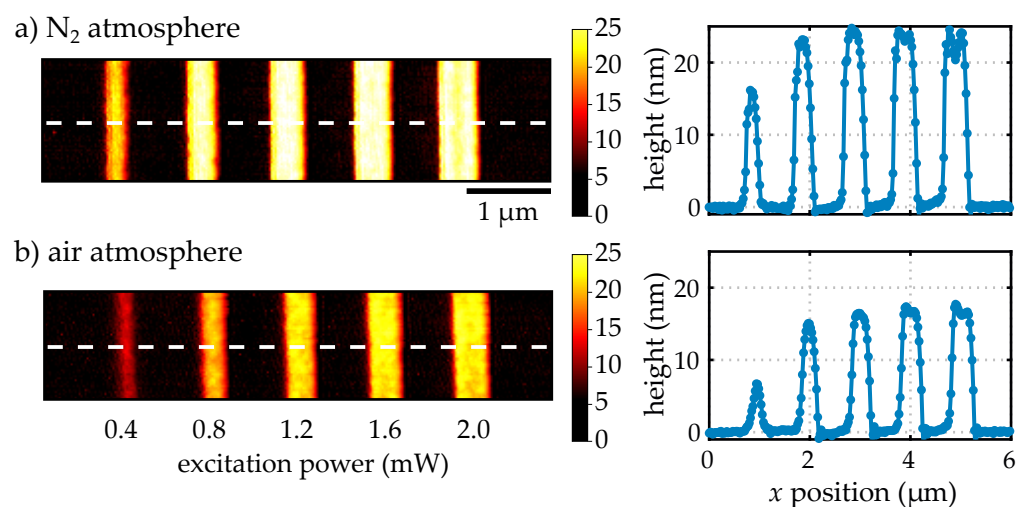
Figure 4.7: AFM measurements for two sets of lines written on the same sample with identical writing conditions, but under different atmospheric environments. Line cuts show that polymer brushes grow up to 135 % higher under nitrogen atmosphere. Adapted from [138].

Influence of Oxygen

Another piece of evidence for the presented mechanism is the influence of the atmospheric environment. Figure 4.7 a) shows a set of lines written with varying excitation power inside a sealed chamber under nitrogen atmosphere. After writing, the chamber was opened to allow ambient air, in particular oxygen, to diffuse into the maleimide solution. Afterwards, another set of lines was written with the same parameters, depicted in part b) of Figure 4.7. Line cuts derived from the AFM measurements indicate that the heights of the lines written under nitrogen atmosphere are higher compared to the nominally identical lines written in ambient air. Below the saturation regime, at a laser power of 0.4 mW, the difference in line height is 135 %. Moreover, the height of the saturation level also differs between the two sets. These effects can be attributed to partial scavenging of the intermediate biradical states present during the course of photoenolization (Figure 4.1) by oxygen [169]. As a result, the affected *o*-MBA molecules are lost irreversibly, leading to lower initiator density and thereby to reduced polymer brush heights.

4.2.1 PROVING THE REVERSIBLE DEPLETION EFFECT

To demonstrate the expected depletion effect, precisely overlaid Gaussian laser beams were employed (see Figure 3.5) and a series of patterns was written as depicted in Figure 4.8. While the excitation laser was activated permanently, the depletion laser was only switched on in the central part. It is clearly visible, that the depletion beam completely suppressed the functionalization. Previously written lines were not affected by the depletion light (dashed area A). Furthermore, by writing through the previously depleted area (dashed area B), it was demonstrated that the depletion effect is predominantly reversible, *i.e.*, that (Z)-enols are converted to (E)-enols and transit back into the *o*-MBA ground state. These findings are necessary prerequisites for STED-inspired lithography systems and are crucial for fabrication of more complex patterns other than single isolated lines. However, line height decreases by 23 % at the second crossing point, indicating a certain amount of irreversible reaction pathways. This contribution became more pronounced for larger excitation and depletion powers as depicted in Figure 4.9. For higher excitation powers, higher depletion powers are needed to achieve a considerable depletion effect and in consequence the irreversible contribution becomes larger. At yet higher excitation and depletion powers, previously written lines were damaged as well, presumably due to similar effects as seen above when writing far in the saturation regime. While these effects pose a limitation to the practicable excitation and depletion powers, the depletion effect worked very well within a certain power range and we restricted our experiments in the following to this range.

Determination of Intermediate-State Time Scales

The effective lifetime of the intermediate (Z)-enol can be assessed by imposing a time-gating scheme onto the excitation and depletion lasers, following a method known in literature [106]. By electronically gating the acousto-optic modulators used for power control of the laser beams, we switched each of them on for a super-pulse of 5 µs within a time windows of 250 µs (corresponding to a modulation frequency of 4 kHz). We varied the time shift Δt between the excitation and depletion super-pulses from -10 µs to 100 µs and wrote a test pattern with varying excitation and depletion power for

AFM measurement:

— excitation beam on
◤◥ depletion beam on
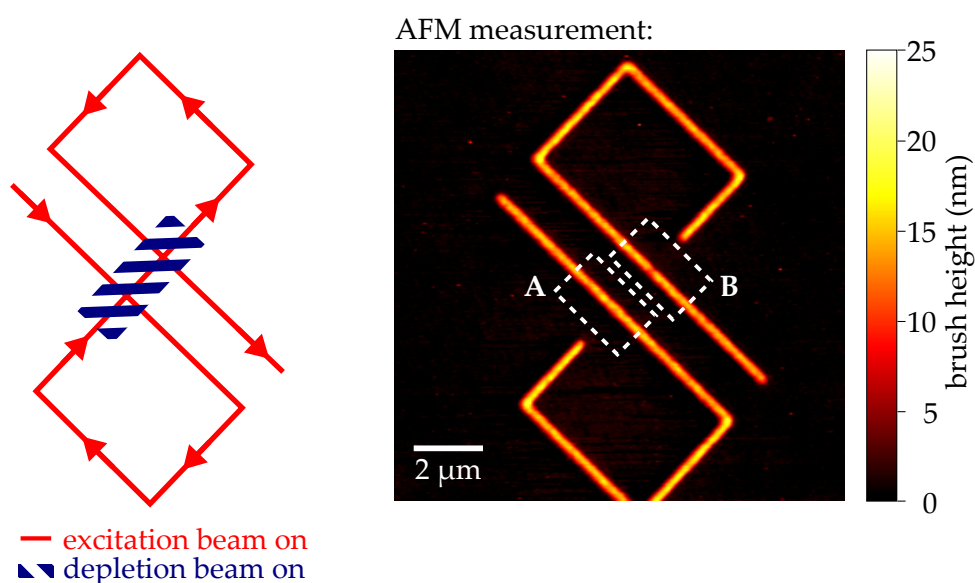
Figure 4.8: A test pattern was written using overlaid Gaussian beams as depicted schematically on the left. The AFM image of the written pattern (right) shows that the depletion light completely suppressed functionalization while leaving previously functionalized parts unaffected (dashed area A). By writing through a previously depleted area, the reversiblity of the depletion effect is demonstrated (dashed area B). Excitation power: 0.33 mW, depletion power: 0.6 mW. Adapted from [138].

each Δt. Figure 4.10 shows AFM images of these patterns and, as a proxy for the strength of the depletion effect, a graph tracking the height of a particular line, *i.e.*, for a fixed pair of excitation and depletion laser power. The results demonstrate that for Δt between $0\,\mu s$ and $5\,\mu s$ the lines at high depletion laser powers were suppressed by a prominent depletion effect. At higher Δt, the depletion effect was gradually reduced until it is barely visible anymore for $\Delta t \geq 25\,\mu s$. At such large time delays, the vast majority of activated E-enol species has already undergone the cycloaddition reaction and is therefore no longer affected by the depletion light. This value fits to reported lifetimes of similar species [143].
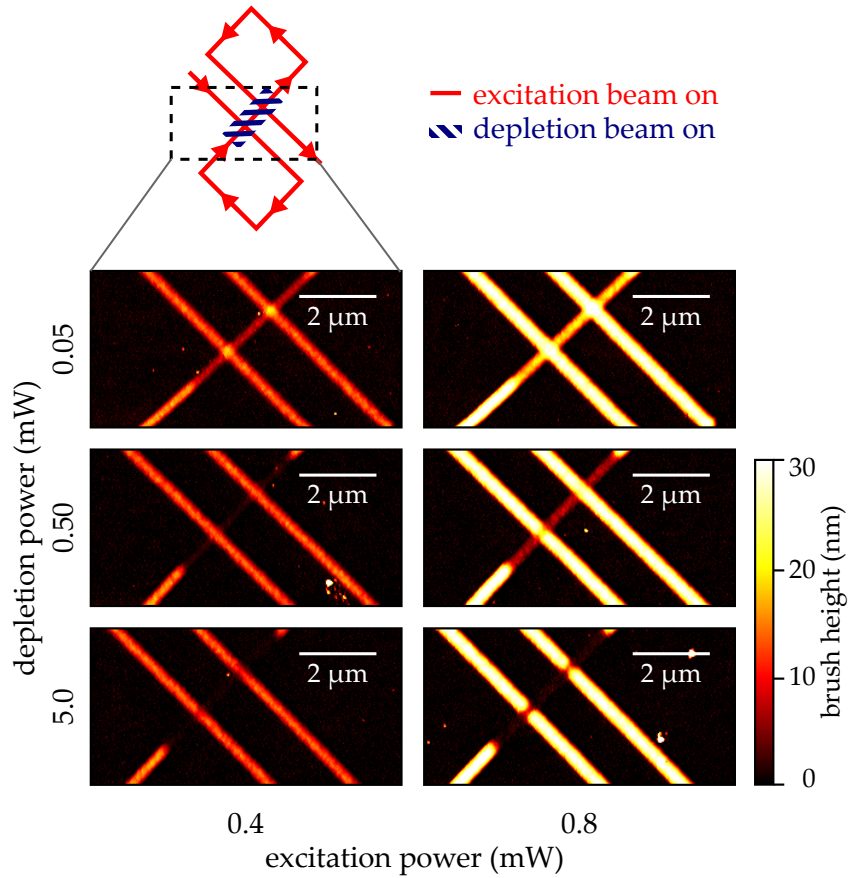
Figure 4.9: AFM images of a set of loop patterns similar to Figure 4.8, but with different excitation and depletion powers. Gaps in the crossing points of the exposure paths reveal irreversible contributions high depletion powers. Adapted from [138].

4.2.2 LATERAL RESOLUTION ENHANCEMENT

In order to investigate the possible resolution enhancement of the mechanism, a depletion laser focus with a plane of zero intensity in its center was employed, as shown in Figure 3.5. To generate such a focus, we introduced a half-space phase mask into the depletion beam path at the position indicated in Figure 3.1. The laser beams were overlaid such that the minimum of the depletion focus was positioned on the maximum of the Gaussian excitation focus. In such a configuration, one can expect to achieve a reduc-
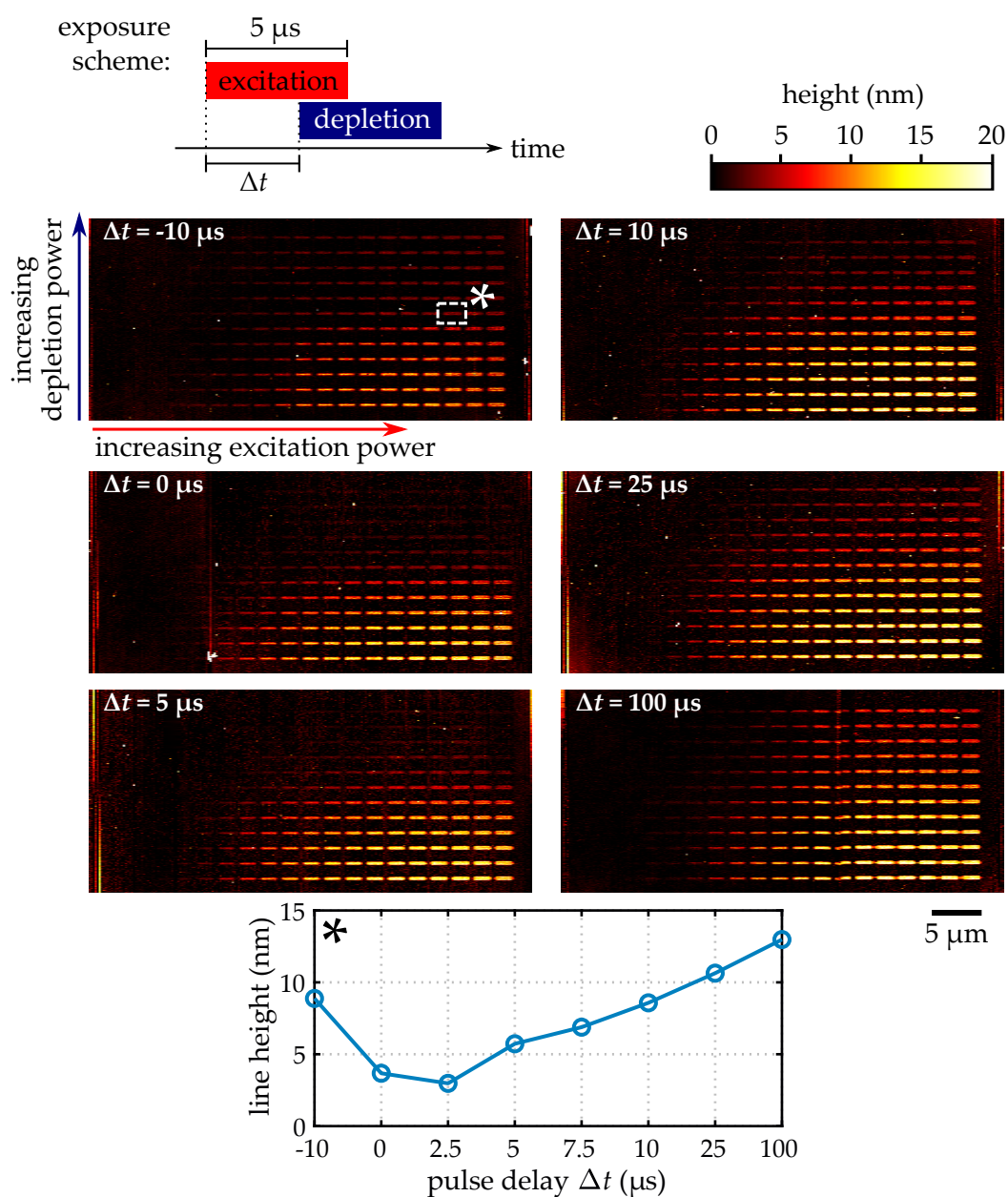
Figure 4.10: AFM images of patterns written for determination of the effective intermediate-state lifetime of (Z)-enol. During exposure, the lasers are electronically super-pulsed as shown in the scheme. In the graph at the bottom, the height of the marked line (*) is plotted over the pulse delay Δt. The depletion effect is most pronounced for Δt between 0 µs and 5 µs. Adapted from [138].

tion in linewidth with increasing depletion laser power, as the Diels-Alder cycloaddition is suppressed in the outskirts of each line.

Feature Size Reduction

Line patterns were written using the excitation laser where the depletion laser was switched on for the central part of each line. The AFM images depicted in Figure 4.11 represent typical results of such writing experiments. The depicted depletion laser powers range from 0.07 mW to 5.95 mW, *i. e.*, span almost two orders of magnitude, while the excitation laser power is fixed at 0.8 mW. Within the reversible depletion regime, very similar results were obtained using different excitation laser powers and appropriately shifted depletion powers. Clearly, the depletion effect leads to a very pronounced linewidth reduction that is accompanied by a parallel reduction of the polymer brush height. Different line profiles are obtained from the AFM data at the indicated positions and averaged along the direction perpendicular to the lines in order to compensate for the typical roughness stemming from the non-uniform polymer growth. The FWHM of an undepleted line at this excitation power is found to be 355 nm. The shape of the corresponding line profile A exhibits a flattened top which can be attributed to the saturation effects mentioned above. Evaluation of the line profiles B to E shows that the lines could be narrowed down to 60 nm FWHM, which is a factor of 3.5 below the FWHM of the squared excitation intensity profile. Over all conducted experiments, this is a typical value. The smallest FWHM found is 54 nm. As I have explained above, the linewidth is expected to be equal to or larger than the squared excitation intensity profile when using only the excitation laser. In that sense, a sub-diffraction linewidth, *i. e.*, feature size, was achieved.

The line profiles in Figure 4.11 also show that the height of the polymer brushes decreases with increasing depletion laser power and thus limits further linewidth reduction. This behavior can be explained by a combination of conformational properties of the grown polymer brushes and optical imperfections in the lithography process. In order to understand these effects in a quantitative way, we extend the rate model described above.
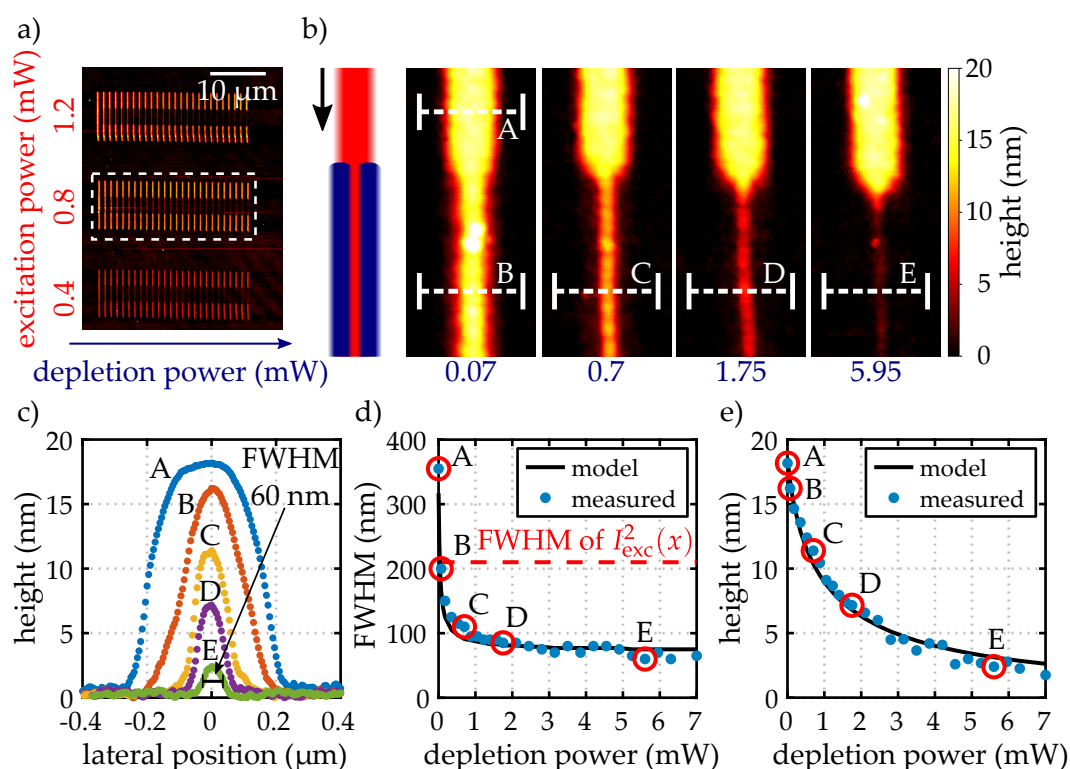
Figure 4.11: AFM images of patterns written for determination of accessible linewidths. a) Excitation and depletion powers are varied in order to identify the ideal parameters. b) The depletion laser is switched on in the central part of each line. With increasing depletion laser power, the linewidth is reduced. c) Profiles along the labeled lines are used to determine the full width at half maximum (FWHM) of each line. The smallest values are typically around 60 nm. d) The FWHM of the lines undercuts the FWHM of the squared excitation intensity, indicating sub-diffraction linewidth. e) The height of the lines is decreased with rising depletion power. The data from panels d) and e) can be reproduced in good agreement by a rate equation model (see main text for details). Adapted from [138].

Rate Equation Model Modified by Nonlinear Polymer Growth

Previously, we assumed that the initiator density on the functionalized substrate surface translates linearly into the polymer brush height. For modeling patterns that were written with the depletion laser switched off, this turned out to be a reasonable assumption. However, when going to
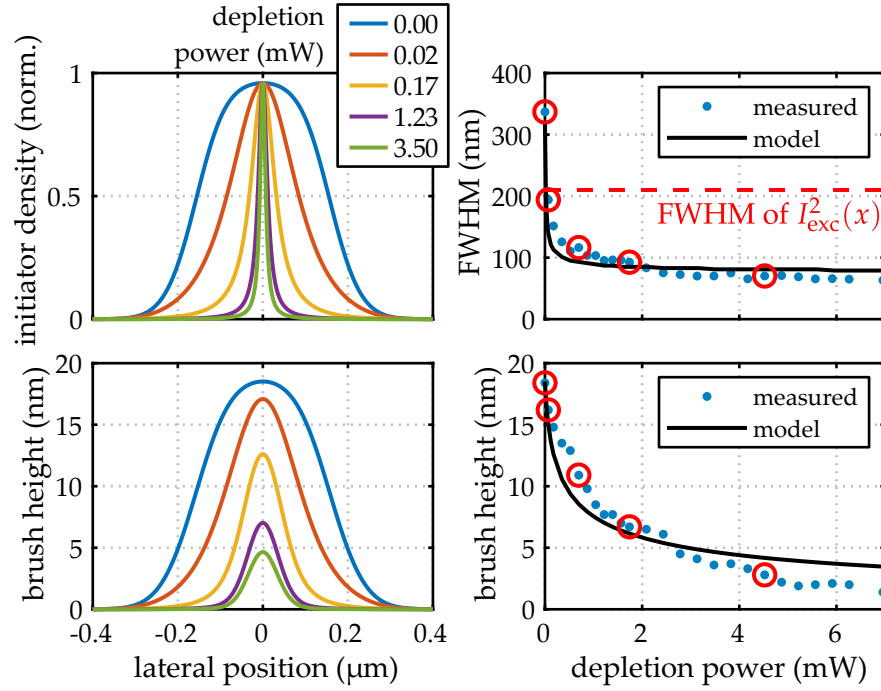
Figure 4.12: Results of calculations based on a rate equation model modified by nonlinear brush growth under the assumption of the depletion laser minimum touching zero. The spatial initiator distribution is convoluted by a Gaussian to account for nonlinear brush growth effects and then translated into polymer brush height, which leads to a decrease in height for high depletion powers. Experimental data from Figure 4.11 is shown as a reference. Adpated from [138].

low initiator densities or when the initiators are confined to lithographically defined patterns of sub-micron size this does not hold true anymore [170]. In those cases, the polymer brushes do not erect to full height but rather fold into a so-called mushroom configuration [171]. In order to model such nonlinear brush growth effects, we convolute the calculated initiator density $N_E(x)$ by a Gaussian with $\sigma = 0.25\,\mu\text{m}$. The resulting initiator distribution is linearly translated into brush height. The results of these calculations shown in Figure 4.12 reveal a decrease in line height with rising depletion power, although the brush height is overestimated compared to the experimental data.

Rate Equation Model Modified by an Imperfect Depletion Focus

Another approach to explain reduced brush height with increasing depletion laser power is to assume that some finite residual intensity remains in the minimum of the depletion focus. In this way, the initiator density and thus the height polymer brushes is also lowered in that area, comparable to global depletion when using a Gaussian depletion focus. This even holds true when the aforementioned effects of modified polymer growth are neglected. We incorporate this into our rate model by rewriting the analytical function describing the depletion intensity profile given in Equation 4.3,

$$I_{\text{depl}}(x) = \exp\left(-\frac{x^2}{2\sigma_{\text{depl}}^2}\right) \cdot \left(x^2 + r\right) , \qquad (4.4)$$

where residual intensity in the minimum of the depletion focus by constant term r. The focus measurement (Figure 3.5) shows a residual intensity of 1.6 % of the maximum, which corresponds to a value of $r = 1.4 \cdot 10^{-4}$. It remains unclear, whether this is reasonably close to the real value, as the typical measurement uncertainty is on the order of 1 %. Further, it is conceptually impossible to measure infinitesimally small features by scanning finite-sized gold beads. In Chapter 6, this issue will be discussed in more detail. Nevertheless, the calculation results depicted in Figure 4.13 demonstrate that employing this approach reproduces the decline in brush height observed in the experimental data, although FWHM is systematically underestimated. Similar effects are also reported for STED microscopy employing the same type of phase mask with comparable fractional intensity [98].

While both investigated models on their own only partially explain the experimental findings, we assess a combination of both effects. The combined model reproduces the experimental data very precisely, as shown by the black curves in panels d) and e) of Figure 4.11. Therefore, we can conclude, that both effects play a role in our experiments.

Grating Structures

After assessing the potential linewidth reduction enabled by employing the depletion effect, we want to investigate the resolution of the process, *i.e.*, the minimum distance two such lines can be written next to each other
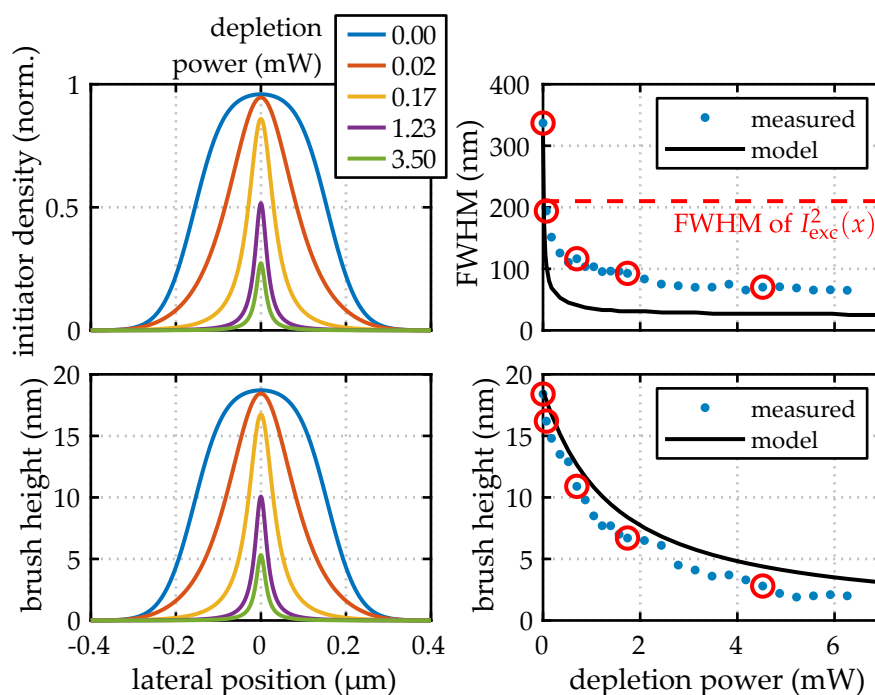
Figure 4.13: Results of calculations based on a rate equation model assuming a finite residual intensity of 1.6 % in the depletion laser minimum. The peak values of the spatial initiator distribution decreases for increasing depletion power. The distribution is linearly translated into polymer brush height. Experimental data from Figure 4.11 is shown as a reference. Adpated from [138].

while they are still separated. Therefore, we fabricated line gratings that consist of several sequentially written lines. The grating period *a* was varied as well as excitation and depletion power. AFM images of a typical set of such gratings for different values of *a* are depicted in Figure 4.14. Similar to the individual line patterns presented above, the depletion laser is only switched on for the second half of each line. Clearly, in the parts that were exposed solely to the excitation laser, flat top plateaus were formed that feature irregular surface corrugations stemming from the polymer growth process, as shown in the profiles A, C, and E in panel b) of Figure 4.14. A clear periodicity is not visible. With decreasing grating period, these plateaus heighten due to increased initiator density on the surface, implying that the functionalization is still not completely saturated at the depicted
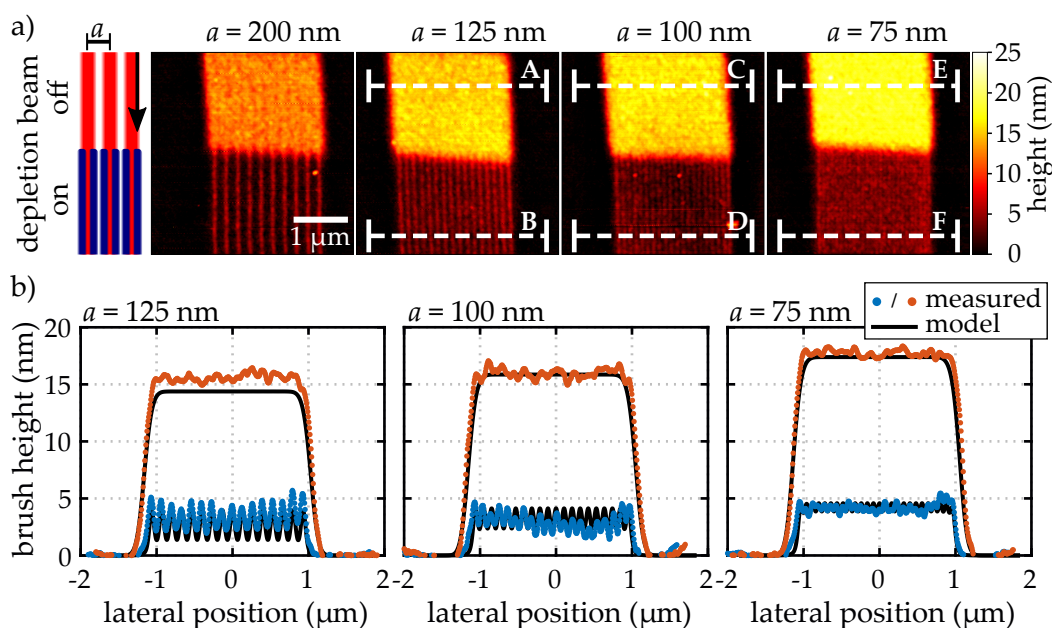
Figure 4.14: a) Line gratings with varying a lattice constants *a* were fabricated by writing individual lines sequentially. The depletion laser is switched on for the lower part of each grating. Down to 100 nm, the grating corrugation can be retrieved in those parts. b) Line profiles of the images show that the space between the lines is partially filled up. The experimental data can be described by a rate equation model (details see main text) in good agreement. Adapted from [138].

excitation powers and grating periods. When looking at the profiles B, D, and F through the parts that were simultaneously irradiated with the depletion laser, we find that periodic corrugations of the polymer brush surface are still visible down to a grating period of $a = 100$ nm. Below that value, *e. g.* at $a = 75$ nm, surface roughness of the polymer prevents unambiguously retrieving a periodicity. For comparison, according to Sparrow's criterion for a two-photon process at 700 nm wavelength and focusing with $NA = 1.4$, the resolution limit without any depletion effects is 177 nm (calculated using Equation 2.7). Therefore, we can conclude that we achieved sub-diffraction resolution. The AFM images reveal that the gaps between the lines of the gratings are partially filled up. This can easily be explained by the fact that the surface functionalization approach does not possess a writing threshold

as typically present for network-forming photoresists. The exposure doses of neighboring lines add up leading to the growth of polymer brushes between the actually exposed lines. Similar to the experiments on individual lines, we observe decreased heights for lines that have seen the depletion light. Again this effect can be explained by the aforementioned combined model that reproduces the experimental data in good agreement.

Alternative Functionalities

With the surface functionalization approach described in this section, we have demonstrated that photoisomerization of intermediate-state photoenols generated from the *o*-MBA chromophore can in fact be employed to achieve sub-diffraction feature sizes and resolution. I would like to emphasize again at this point, that the described process can be easily adapted to achieve different surface functionalities by simply exchanging the maleimide species employed in the lithography step. Especially with regard to biological functionalities, a variety of different maleimide-functionalized molecules is commercially available.

As an example, we conducted experiments using a biotin-carrying maleimide. Instead of growing polymer brushes, we used the the biotin groups on the surface for immobilization of streptavidin dyes, followed by investigation with fluorescence microscopy. After the lithography step, the surface was first passivated by applying a drop of a $1\,\mathrm{mmol\,L^{-1}}$ solution of poly(ethylene glycol)-maleimide in DMF, followed by UV flood exposure for $1\,\mathrm{h}$. After thorough rinsing, streptavidin functionalized with the fluorescent dye Alexa 647 was applied as a solution in phosphate-buffered saline at a concentration of $0.01\,\mathrm{mg\,mL^{-1}}$ for $30\,\mathrm{min}$. In this way, the fluorescent dye was immobilized on the functionalized areas. As explained in the beginning of this section, to resolve sub-diffraction features the measurement method itself needs to be diffraction-unlimited, ruling out simple confocal microscopy. Therefore, samples were inspected using super-resolved stochastic localization microscopy which was performed on a custom-built setup by Lu Zhou (APH, KIT). Unfortunately, the resulting images suffered from unspecific binding (Figure 4.15) and thus did not offer as much insight as the AFM images discussed above. Nevertheless, a depletion effect is clearly visible.

While surface functionalization is conceptually limited to fabrication of

planar structures. In the next section, I present a different approach based on the *o*-MBA chromophore that allows for true 3D structures.
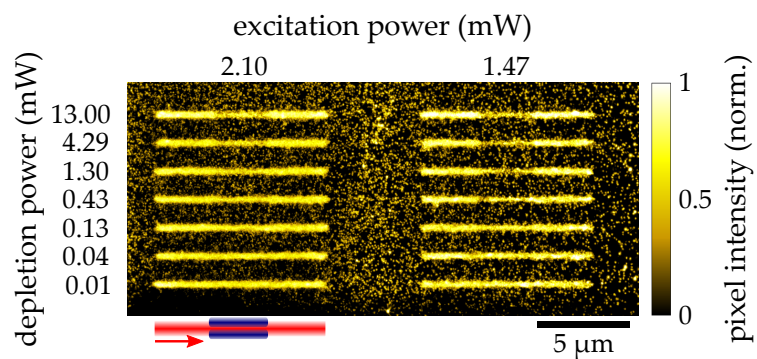
Figure 4.15: Written patterns functionalized with fluorescent dye, imaged by Lu Zhou using stochastic localization microscopy. The depletion laser is switched on in the central part of each line, decreasing the linewidth. Adapted from [138].

4.3 3D Photoresist Based on Dimerization

The first photoenol-based negative-tone photoresist was introduced by Quick *et al.* and proved to be suitable for fabrication of complex 3D structures [136]. The resist solution was composed of two solid components, a tetrafunctional *o*-MBA linker and a methacrylate copolymer bearing maleimide moieties as side groups, and a solvent mixture. Upon two-photon excitation of *o*-MBA, Diels-Alder cycloaddition of generated (Z)-enol and maleimide leads to formation of a stable covalent cross-link between two such molecules. Thus, the formation of an insoluble network proceeds *via* step-growth polymerization. While this approach allowed the fabrication of freestanding 3D structures such as woodpile photonic crystals [27, 34, 35, 172], the structures exhibited grainy surfaces which limited the achievable resolution [165]. The cause of these deteriorations remained unclear but it was speculated that it is connected to the rather low achievable concentration of solid compounds in the photoresist of 10 wt% [165]. As a result, the volume concentration of chromophores was low as well, averting a high cross-linking density. Moreover, the structures were probably swollen immediately by the solvents leading to severe shrinkage effects after development. Therefore, that photoresist is not suitable for investigating possible resolution enhancement by STED-inspired DLW.

To break new ground, we herein introduce a 3D-capable photoenol photoresist that consists of methacrylate copolymers carrying *o*-MBA chromophores as side groups. Instead of Diels-Alder cycloaddition with a dienophile, we rely on self-dimerization of photoenols (see Figure 4.2 d)) for cross-linking between individual chains. Thus, the photoresist consists of just the copolymers and a solvent. Figure 4.16 schematically shows the chemical structure of the copolymers and the principle of cross-link formation upon two-photon excitation of the chromophores. As the self-dimerization also proceeds *via* intermediate-state (Z)-enols, writing inhibition should be possible by depletion of the (Z)-enol population. The choice of a methacrylate backbone was motivated by the feasibility in synthesis of the molecules and the high resolution that has been achieved with poly(methyl methacrylate)-based copolymers in electron beam and UV lithography [173, 174].

The methacrylate copolymers were synthesized by Tim Krappitz (QUT,

PE-1 to **4**
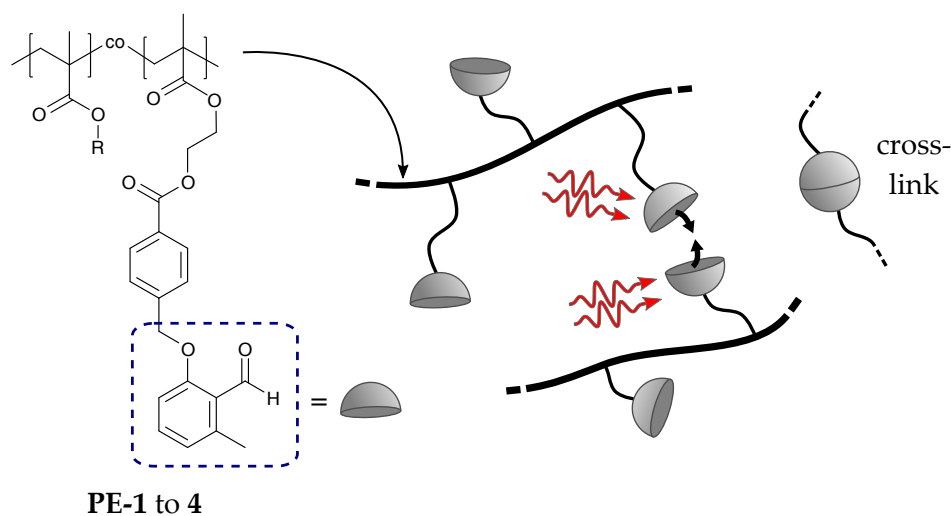
Figure 4.16: Scheme of the copolymers bearing *o*-MBA units. Upon two-photon excitation of the *o*-MBA chromophores, formation of covalent cross-links between copolymer chains proceeds *via* dimerization.

Brisbane) according to a literature procedure based on thermally initiated free-radical polymerization [162]. At KIT, I prepared the photoresist solutions and performed the work for processing and characterizing the samples. Eva Blasco (ITCP, KIT), Tim Krappitz, Christopher Barner-Kowollik (QUT, Brisbane), and Martin Wegener were involved for interpretation of the data and planning of experiments. Sample processing followed the steps given in Section 3.3.2. The lithography setup remained unchanged from the surface functionalization experiments described in Section 4.2. Therefore, the same wavelengths and laser sources were employed as in the previous section, *i.e.*, 700 nm for two-photon excitation and 440 nm for depletion. For all lithography experiments in this section, a scan speed of $100\,\mu\mathrm{m\,s^{-1}}$ was used. The fabricated structures were analyzed by light microscopy and scanning electron microscopy (SEM).

4.3.1 COPOLYMER AND PHOTORESIST PARAMETER STUDY

There are several degrees of freedom in the design of the copolymers and the photoresist composition, *i.e.*, choice of solvent, functionalization degree,

copolymer concentration in the resist solution, molecular weight (given by the chain length), and choice of side groups. In order to understand the influence of these parameters and optimize the photoresist, we conducted screening experiments. By adjusting the composition of the monomer feed used for the synthesis, different copolymer compositions listed in Table 4.1 were realized with varying number average molecular weight M_n and varying molar ratios between the constituent monomers. Employed monomers were *o*-MBA-carrying methacrylate (BAMA), methyl methacrylate (MMA), butyl methacrylate (BMA), tetrahydrofurfuryl methacrylate (THFMA), and isobornyl methacrylate (IBOMA) (Figure 4.17). Different copolymers were used to prepare photoresists that were characterized in experiments using solely the excitation laser beam. One important quantity that was determined is the laser power that is necessary to generate a cross-link density sufficient to overcome the gelation point, *i.e.*, to make the resulting network insoluble during development. This so-called threshold power was determined by writing a dose test pattern which consists of a set of lines written with stepwise increasing laser power. Moreover, the capability of writing freestanding 3D structures was evaluated by writing simple bridge structures at laser powers above the threshold power by a fixed percentage.

Table 4.1: Copolymer compositions used for the parameter study.

	M_n (g mol^{-1})	BAMA (mol%)	MMA (mol%)	BMA (mol%)	THFMA (mol%)	IBOMA (mol%)
PE-1	7500	23	77	-	-	-
PE-2	6700	42	58	-	-	-
PE-3	9300	79	21	-	-	-
PE-4	26400	22	78	-	-	-
PE-5	7200	20	15	65	-	-
PE-6	7100	24	-	-	76	-
PE-7	6700	20	-	-	-	80

Molar ratios given by the monomer feed applied in synthesis.
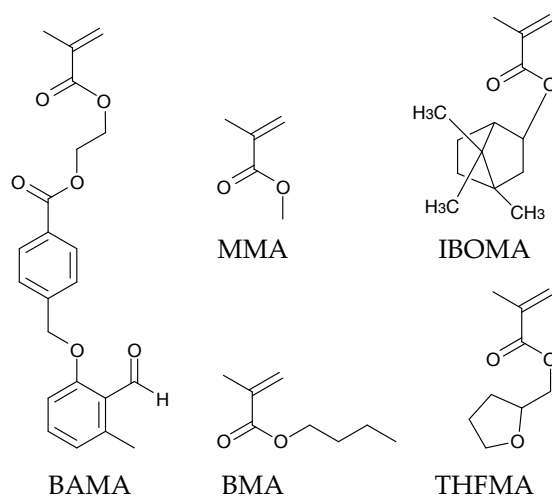
Figure 4.17: Different monomer units employed for copolymer synthesis (compare to Table 4.1): *o*-MBA-carrying methacrylate (BAMA), methyl methacrylate (MMA), butyl methacrylate (BMA), tetrahydrofurfuryl methacrylate (THFMA), and isobornyl methacrylate (IBOMA).

Choice of Solvent

A suitable solvent for the photoresist should fulfill several criteria. i) It should dissolve the copolymers well and allow for highly concentrated solutions, ideally in the range of several 10s of weight percent. ii) It should be transparent for the employed wavelengths. iii) It should be inert to the employed components, *i.e.*, not lead to cross-reactions. iv) It should have a low vapor pressure such that no significant evaporation takes place during handling and processing of samples. After screening several possible candidates, acetophenone was identified as the best solvent thereof that fulfills all conditions above and allowed for the highest polymer loads. Acetophenone was already employed in the past as a solvent for DLW resists [63, 136, 153].

Functionalization degree

The number ratio of BAMA groups to other methacrylate groups in the copolymers, *i.e.*, the functionalization degree of the copolymer, is a trade-off. On one hand, a high volume density of chromophores is desired for efficient
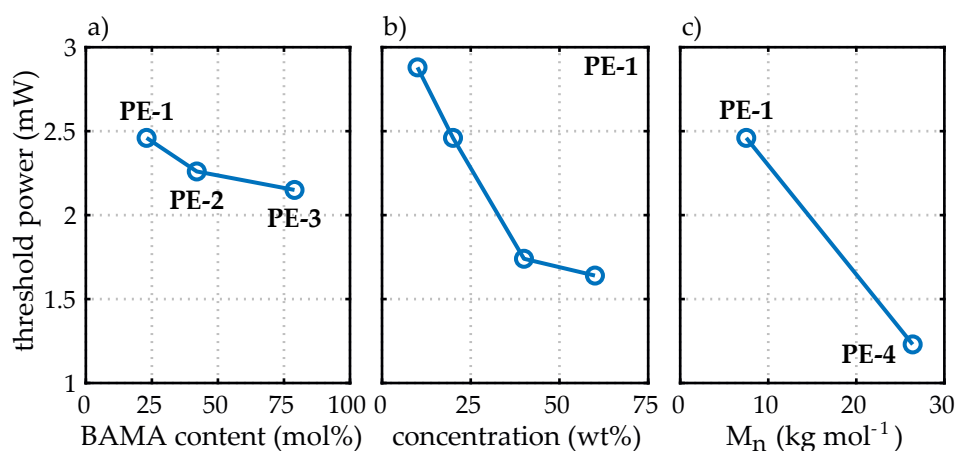
Figure 4.18: The writing threshold power in dependence of different photoresist parameters. The solvent was acetophenone in all cases. The used copolymers are indicated next to the data points. a) Influence of the content of BAMA (functionalization degree) in the copolymer for fixed chain length and concentration. b) Influence of the copolymer concentration in the photoresist solution for fixed functionalization degree and chain length. c) Influence of the chain length of the copolymer, represented by the molecular weight M_n, for fixed functionalization degree and concentration.

dimerization but on the other hand, high functionalization degrees typically lower the solubility of the molecules and increase the probability of unwanted intra-molecular dimerization. The copolymers **PE-1**, **PE-2**, and **PE-3**, which have similar molecular weights and thus similar chain lengths, were dissolved at 20 wt% in acetophenone. Figure 4.18 a) shows the dependency of the threshold power on the functionalization degree. The threshold power only moderately decreased by 13 % for an increase in functionalization degree by almost a factor of 4. On the other hand, the solubility of copolymers strongly decreased with increasing functionalization degree.

Copolymer Concentration

The concentration of copolymers in the photoresist solution, given the weight percentage, is proportional to the volume density of chromophores. Thus, we expect that higher concentrations lead to lower threshold powers. This is confirmed by the experimental data shown in Figure 4.18 b) for the copolymer

PE-1 at different concentrations in acetophenone. The threshold decreases roughly linearly with concentration but between 40 wt% and 60 wt% the slope decreases. A possible explanation is, that the volume of the solution is no longer constant but increases with the copolymer load. Thus, an increase in weight percentage does not lead to a proportional increase in chromophore density anymore. This was not investigated in more detail within this work. While it was possible to dissolve the copolymer **PE-1** at concentrations of even more than 60 wt%, the maximally feasible concentrations of copolymers **PE-2** and **PE-3** were 40 wt% and 20 wt%, respectively, due to their higher functionalization degree. This limitation becomes more apparent when looking at SEM images of 3D structures depicted in Figure 4.19. The structure written using **PE-1** at 60 wt% shows significantly less shrinkage than the structure at lower concentration of 40 wt%, indicating a higher degree of cross-linking, most probably due to the higher molar concentration of chromophores. Structures written using the copolymers **PE-2** or **PE-3** at a concentration of 20 wt% suffer from stronger shrinkage as well. The higher functionalization degree of **PE-2** and **PE-3** compared to **PE-1** cannot compensate for the lower concentrations with regard to the cross-linking density. Furthermore, partial fallout occurred during the writing time of about 1 h, causing spots of material on the substrate surface.

Chain Length

Another parameter is the length of the polymer chain, *i.e.*, how many repeating units a chain consists of on average, represented by the number average molecular weight M_n. Due to synthesis by free-radical polymerization, the copolymers were not monodisperse.[3]. Comparing shorter and longer chains with the same functionalization degree, one can expect a decrease in threshold laser power if longer chains are employed. The reason for this scaling is that with each cross-link made a greater mass is added to the existing polymer network compared to shorter chains. Thus, less cross-links are needed in total to achieve a polymer network that cannot be dissolved anymore in the development step, *i.e.*, to cross the gelation point. As a

---

[3] The measured polydispersity index, *i.e.*, the ratio between weight average and number average molecular weight, was 2.0.
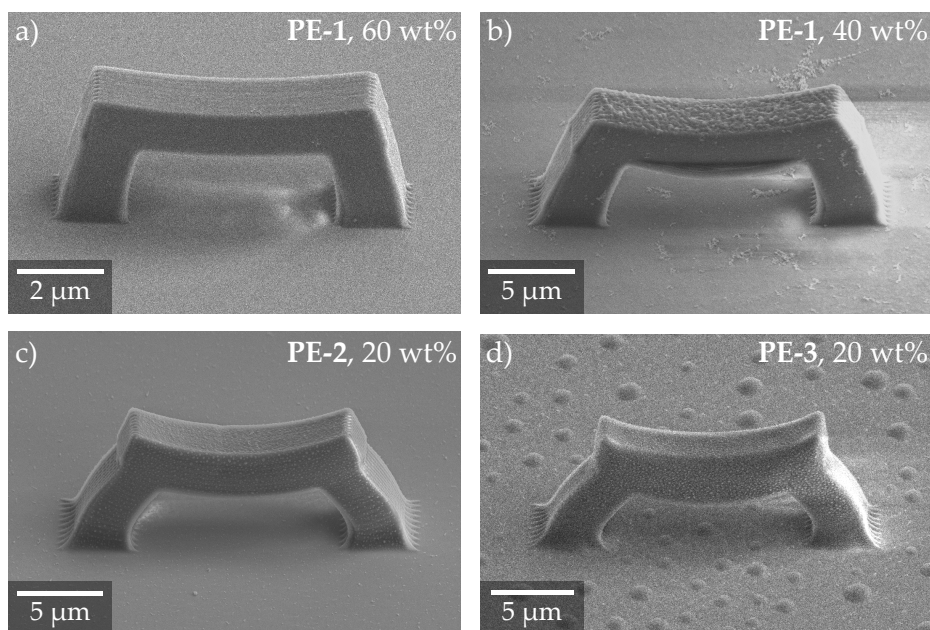
Figure 4.19: SEM images of 3D bridge structures fabricated using different photoresist compositions as indicated in the panels.

result, the cross-link density in a structure written with an excitation power, *e.g.*, 10 % above the threshold, is expected to be lower when using long chains. Such a dependence was reported in literature [175] and we could find this behavior in our resist system as well, as shown in Figure 4.18 b). By comparing copolymers **PE-1** and **PE-4** which have approximately the same functionalization degree at the same concentration, we found that an increase in M_n by a factor of 3.5 led to a 50 % decrease in threshold power. 3D structures written using **PE-4** exhibited shrinkage very similar to **PE-2** and **PE-3** (not depicted), which can be interpreted as a direct result of the lower cross-linking density.

Copolymer Side Groups

The material properties of copolymers, especially glass transition temperature or Young's modulus, can be tuned by introducing other side groups additionally to methyl and *o*-MBA. In the procedure used herein, this was achieved by simply adding the BMA, THFMA or IBOMA in the corresponding ratios to the polymer feed during synthesis [162]. Different photoresists

consisting of the resulting copolymers **PE-5**, **PE-6**, and **PE-7** (listed in Table 4.1) were evaluated. The structures written using **PE-5** at 60 wt% in acetophenone show very similar quality to **PE-1** at the same concentration. In contrast, the use of **PE-6** resulted in very grainy structures while employing **PE-7** led to a high degree of shrinkage (not depicted). Thus, by adding different side groups, no improvement could be observed within our experiments.

To conclude, the concentration of copolymers in the photoresist solution is the most critical parameter for the tested systems with regard to achieving high cross-linking densities. Thus, the photoresist consisting of **PE-1** dissolved at 60 wt% in acetophenone was employed for further experiments.

4.3.2 FABRICATION OF COMPLEX 3D STRUCTURES

Order of Nonlinearity

As demonstrated in Section 2.1.2, an effectively nonlinear process is necessary in order to be able to fabricate truly three-dimensional structures. While the bridge structures shown above have already demonstrated the 3D capability of our photoresist, the experimental determination of the order of nonlinearity N can still provide some insight into the resist system.

To determine N for our photoresist, we employed an established method that was previously published by our group [12, 72], which I briefly revisit in the following. In multi-photon lithography, the exposure dose necessary to cross the gelation point, D_{thr}, is given by a time integral over the exposure time t_{exp} as

$$D_{\mathrm{thr}} \propto \int_{t_{\mathrm{exp}}} P_{\mathrm{avg}}^{N}(t)\, \mathrm{d}t \,, \tag{4.5}$$

with the average laser power P_{avg}. Instead of delivering the laser light as a continuous train of femtosecond laser pulses, we applied super-pulses of width Δt and repetition rate R by electronically gating the excitation beam using the acousto-optic modulator, as shown schematically in Figure 4.20 a). Thus, the threshold dose can be rewritten as

$$D_{\mathrm{thr}} \propto t_{\mathrm{exp}} \cdot R \cdot \Delta t \cdot P^{N} \,, \tag{4.6}$$
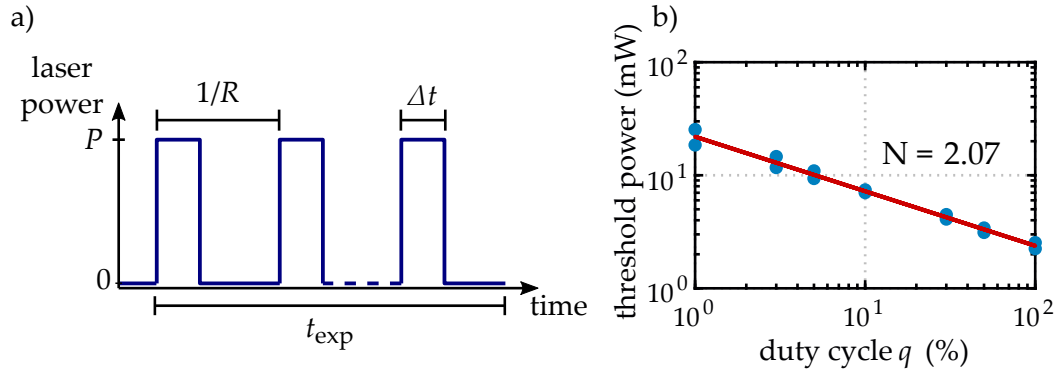
Figure 4.20: a) Scheme of the super-pulsing scheme imposed onto the excitation laser using the acousto-optic modulator. b) A linear regression of the threshold laser power dependence on the duty cycle q of the super-pulsing scheme yields the effective order of nonlinearity N of the process.

with the peak power P of one super-pulse. The exposure time is inversely proportional to the writing speed and is kept constant. Therefore, the laser power necessary to cross the threshold, P_{thr}, is given by

$$P_{thr} \propto \left(\underbrace{\frac{D_{thr}}{R \cdot \Delta t}}_{=:q} \right)^{\frac{1}{N}} . \tag{4.7}$$

The quantity q can be identified as the duty cycle of the super-pulsing scheme. For different sets of repetition rate R and super-pulse width Δt, *i.e.*, for different values of q, dose test patterns were written to determine the threshold power. A double-logarithmic plot of the resulting threshold powers over the duty cycle is depicted in Figure 4.20 b). The data points lie on a straight line. By taking the logarithm of Equation 4.7, one finds

$$\log P_{thr} = -\frac{1}{N} \cdot \log q + \frac{D_{thr}}{N} . \tag{4.8}$$

Therefore, the negative inverse of the slope calculated by linear regression yields the effective order of nonlinearity $N = 2.07$. The resist shows an effective two-photon behavior.

This result could be explained by assuming that two photons need to be absorbed to create a single cross-link between two copolymer chains. However, this would be contradicting to the underlying chemical processes as

two photoenols must be present for dimerization [162], which would require $N = 4$ photons. This contradiction can be possibly explained by taking a view on the greater picture. The formation of a network is a highly nonlinear process whose theoretical description is challenging. In the case of DLW, the exposed volume is very small such that diffusion effects [74] and statistical fluctuations [75, 76] play a major role. A study by Fischer *et al.* on several acrylate-based photoresists that were presumably initiated by two-photon absorption, revealed that depending on the repetition rate and the employed photoinitiator, regimes exhibiting different effective orders can be found [72]. In our case the network formation can be assumed to follow step-growth dynamics [135]. As each molecule carries on average 10 *o*-MBA moieties, intramolecular reactions which impede network formation possibly play a role. Furthermore, in DLW experiments, the exposure volume is usually hit by many consecutive pulses and is moving through the resist, which both influence the gelation process. It was reported that the employed scan speed influences not only the effective order of nonlinearity but also the shape of polymerized structures due to the interplay of oxygen diffusion [176]. A nonlinear polymerization behavior could even be observed using continuous-wave lasers that for typical two-photon absorption cross-sections should not at all permit an efficient two-photon absorption [8, 11, 12, 70]. Instead, photoactivation is presumably taking place *via* inefficient one-photon absorption while the necessary nonlinearity is stemming from the polymerization process. Thus, the effective order of nonlinearity determined in experiments such as the one described above is not necessarily related to the number of photons absorbed in microscopic processes initiating the cross-linking process.

Shrinkage and Stiffness

The optimized photoresist formulation was employed for fabrication of a variety of 3D structures. In the SEM images shown in Figure 4.21, simple bridge-like structures were written with either varied laser power (panel a)) or varied bridge width (panel b)). At the lowest laser power, which is just at the writing threshold, the resulting structure bent over, most likely during development of the sample, but without losing the connection to the substrate. This indicates that the resist is very soft when written at low
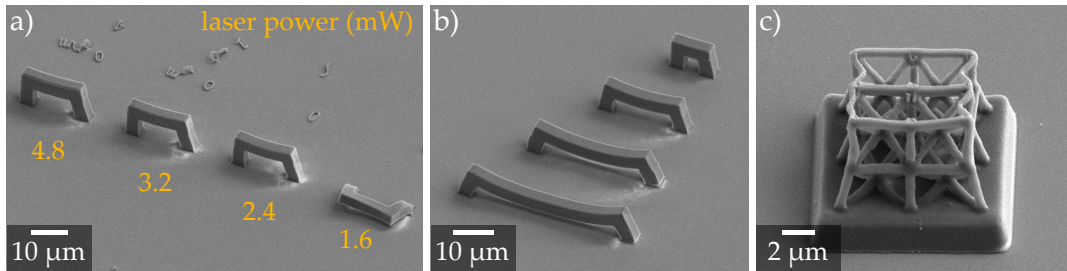
Figure 4.21: SEM images of various 3D microstructures. Stiffness and stability of the structures depend on the laser power (a)) and the geometrical shape (b)) of the structures. Shrinkage induces deteriorations as shown in the scaffold structure in panel c).

powers and that the stiffness can be controlled by the laser power. Such a behavior was also reported for other photoresists employed in 3D DLW [177] and is due to the dependence of the cross-linking density on the laser power. Panel b) shows that elongation of the bridges without appropriate precompensation leads to increased deviations of the actually exposed shape due to shrinkage. Similar shrinkage-induced deteriorations are also visible in the SEM image of a scaffold structure depicted in panel c) of Figure 4.21.

Woodpile Photonic Crystals

Further, woodpile photonic crystals were fabricated varying the laser power and the rod distance a. Figure 4.22 a) – c) shows SEM images of a set of such woodpile structures with a rod distance of $a = 600$ nm. The edges of the structures are heavily deformed as a result of anisotropic shrinkage in the development step. In the center however, the desired structure is retained in good quality. The linewidth on the top layer of the structure is notably reduced to typically 65 nm, at some points even 43 nm, compared to the lines in the two layers below written with nominally the same parameters exhibiting a linewidth of 125 nm and 170 nm respectively. This huge difference can be attributed in part to shrinkage and proximity effects Section 2.1.2. The lines written deeper inside the structure are widened because marginal exposure dose contributions of the neighboring lines added up during writing. Evidently, such proximity effects are very pronounced in the studied photoresist. Panel d) of Figure 4.22 shows a light microscope
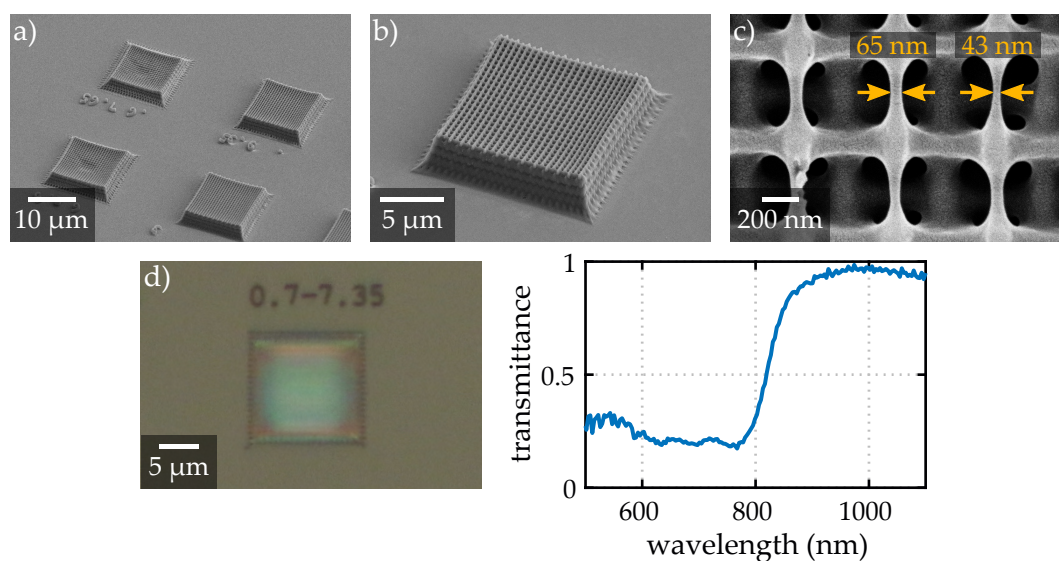
Figure 4.22: a) – c) Scanning electron micrographs of woodpile photonic crystal structures with a nominal rod distance of $a = 600\,$nm. The lines of the top layer show reduced linewidths of typically $65\,$nm due to shrinkage effects. d) A light microscope image under reflection illumination from a different woodpile structure with $a = 700\,$nm shows blueish and greenish color impressions. e) This can be attributed to formation of a stop band in the crystal structure, which is confirmed by a corresponding transmittance decrease in the visible wavelength range.

image of a different woodpile structure with $a = 700\,$nm under reflection illumination. The structure exhibits blueish and greenish color impressions. A transmittance spectrum of the woodpile structure, measured using a white light source and an optical spectrum analyzer with a collecting angle of 24°, is depicted in panel e). The transmittance is almost 100 % above $900\,$nm but drops down to 20 % between $800\,$nm and $500\,$nm due to formation of a stop band in the photonic crystal. The part of the light that is not transmitted must be reflected (neglecting scattering and absorption losses). The existence of a stop band explains the color impression seen in the light microscope image and proves that the woodpile structure is retained in the center of the structure in good quality.

4.3.3 Depletion Experiments

Reversible Depletion

Similar to the experiments on surface functionalization in Section 4.2, a first test towards investigating the depletion effect is assessing the reversibility of the depletion. Therefore, we employed the excitation and depletion lasers with overlaid Gaussian focus shapes (see Figure 3.5) and wrote loop patterns, similar to those already presented in Section 4.2.1 for varying excitation and depletion laser powers. A typical result is depicted in Figure 4.23. Panel a) shows the exposure scheme, where the depletion beam is switched on only for the central part. Writing was clearly suppressed by the depletion light, as can be seen in the scanning electron micrograph in panel b). The crossing in dashed area A shows no degradation of the previously written line. Moreover, it was possible to write through a formerly depleted volume again, as proven by the second crossing marked by dashed area B. Thus, the 3D photoenol photoresist exhibits a reversible activation/depletion behavior very similar to the results of the surface functionalization approach.

Employing the same Gaussian laser foci, the writing threshold power P_thr was determined for several depletion laser powers. As expected, the threshold power increases with rising depletion laser power, as the partial depletion effect needs to be compensated by a higher number of chromophore excitations. To quantify this effect, the relative threshold shift ΔP_rel is calculated with respect to the threshold power at zero depletion $P_\text{thr,0}$ by $\Delta P_\text{rel} = P_\text{thr}/P_\text{thr,0} - 1$. The result obtained for a resist consisting of copolymer **PE-1** at 40 wt% in acetophenone is plotted in Figure 4.23 c). For depletion powers above 0.8 mW, we find a steady decrease in threshold power, which can be attributed to parasitic one-photon writing by the depletion laser. Such a behavior was also observed for other material systems discussed in literature [106]. While the exact power at which this phenomenon kicks in shifted depending on the resist composition and foci used, no parameters could be found to avert it. Therefore, the maximally attainable depletion power is limited, potentially limiting a resolution increase by STED-inspired laser lithography. Still, there is a considerable window for such experiments.

a)

— excitation beam on
↘↘ depletion beam on

b)

2 µm

c)
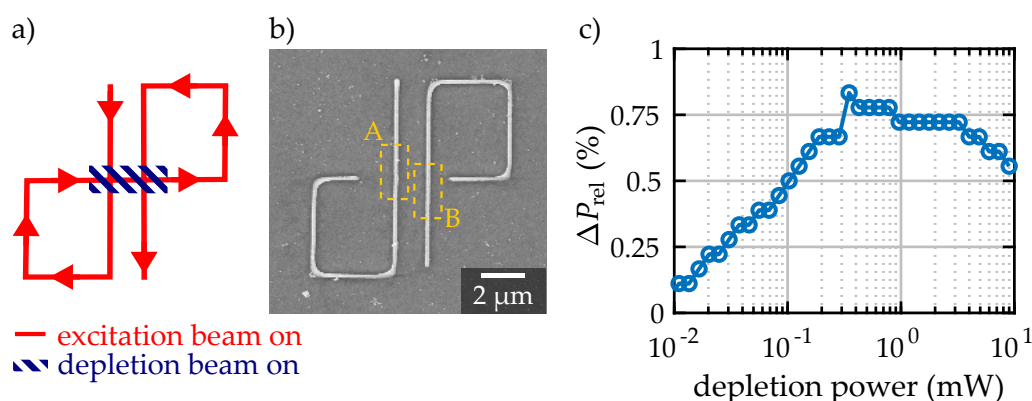
Figure 4.23: Depletion experiments with Gaussian laser foci. a) Scheme of the exposed patterns. b) The depletion laser does not affect previously written lines (dashed area A). It is possible to write through a formerly depleted area again (dashed area B). c) The relative threshold shift caused by the depletion effect in dependence of the employed depletion laser power reveals parasitic writing above depletion laser powers of 0.8 mW.

Enhancement of Lateral Linewidth and Resolution

Having characterized the depletion effect, we investigated possible linewidth and resolution enhancements. By employing a half-space phase mask, a depletion focus featuring a plane of zero intensity through its center was achieved (see Figure 3.5) and line patterns were written where the depletion beam was switched on for the central part of each line. Figure 4.24 shows typical results of such experiments. The linewidth was evidently reduced with rising depletion power until at some point the lines are not continuous anymore. A profile of a line can be obtained from the gray value data of a SEM image, allowing calculation of the FWHM of the line. By taking the mean over a section along the line, fluctuations in linewidth are averaged. In the best case, the FWHM could be reduced down to 51 nm (Figure 4.24 b)). The width of a line written with solely the excitation laser at the same laser power of 2.25 mW is 102 nm. For comparison, the smallest linewidth found without the depletion laser at an excitation power close to the threshold of 1.64 mW was 75 nm. At such low powers, employing the depletion laser directly resulted in disconnected lines. Thus, by employing depletion, a linewidth improvement of 32 % was achieved.
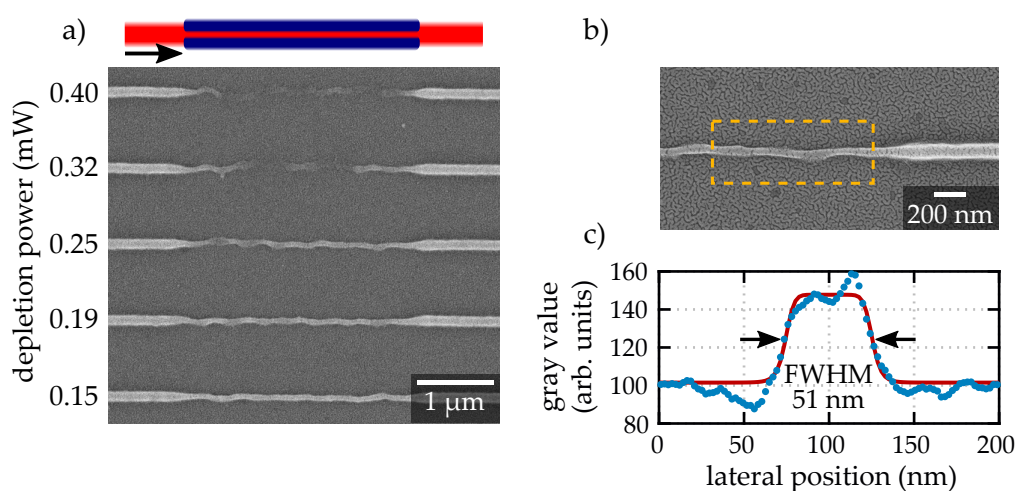
Figure 4.24: a) Line patterns were written by the excitation laser, where the depletion laser was additionally switched on for the central part of each line. The SEM image shows that the linewidth decreases with increasing depletion laser power until the lines are non continuous anymore. The lines are wiggly due to partial detachment from the substrate. b) Close-up view of the thinnest line found. c) A profile of the line averaged along the writing direction is extracted from the SEM data and reveals a FWHM of the line of 51 nm.

However, the SEM images show very prominently that the lines were not straight in the depleted sections but rather formed wiggly lines. Presumably, this stems from the lines being detached from the substrate surface during the development step, when the unused photoresist is removed by immersing the sample in toluene. In order to avoid attachment issues, the cover glasses were silanized with an acrylate-bearing triethoxysilane before conducting the lithography step. In this way, the (Z)-enols could covalently bind to the glass surface *via* Diels-Alder cycloaddition of photoenol and acrylate. As expected, surface adhesion was greatly enhanced. A typical set of line patterns is depicted in Figure 4.25 a) and reveals that the silanization did not allow a further reduction of the linewidth. Instead, the increased adhesion caused the lines to bend over or deform and stick to the substrate. It can be assumed that the lines swell to a significant degree during the development. Figure 4.25 b) explains schematically how this assumption explains wiggly shapes or deformed cross-sections. Directly after writing, the lines written
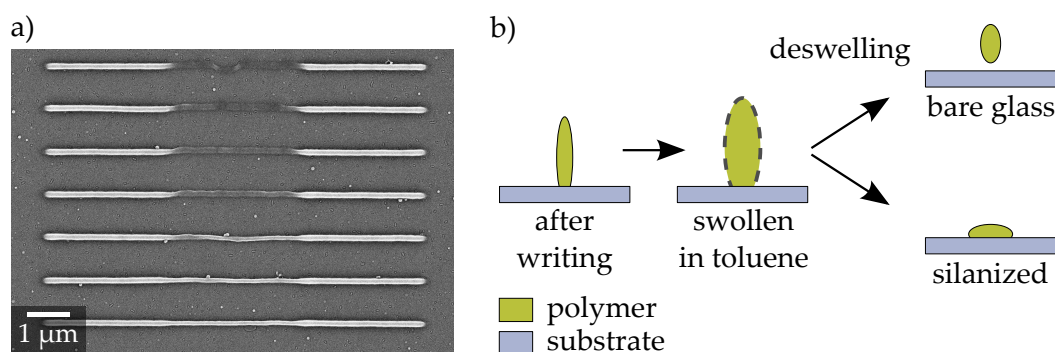
Figure 4.25: a) SEM image of a set of depletion test patterns written onto an acrylate-functionalized substrate. The parts of the lines that were exposed to the depletion laser stuck to the substrate. b) Scheme of possible shrinkage effects. During development, the cross-linked polymer network of a written line swells considerably in toluene, followed by deswelling in isopropyl alcohol. If bare glass substrates are used, the line shrinks in all lateral directions, disconnecting it from the surface. In case of silanized substrate, the line deforms and adheres to the substrate.

with both excitation and depletion beam exhibit a high aspect ratio due to confinement by the depletion focus shape. During development, the structures swell while immersed in toluene. At the same time, their density decreases as unused copolymer is removed. Then the structures shrink again when immersed into the non-solvent isopropyl alcohol due to the loss of residual toluene in the network. In case of a bare glass substrate, the lines detach from the glass substrate and shrink laterally. Without contact to the substrate, the line is deformed by liquid or nitrogen flow while still suspended by the neighboring undepleted lines. If instead a silanized substrate is used, a part of the line is fixed to the glass substrate. When deswelling, the line collapses onto the substrate.

By writing grating structures consisting of sequentially written lines, we assessed the achievable resolution. The lattice constant *a*, excitation power, depletion power and the *z* position with respect to the glass surface were varied in fine steps. When writing gratings using solely the excitation laser, it became apparent that the limitations observed for individual lines applied to grating structures as well. Typically gratings consisted of wiggly lines that formed connections with neighboring lines at several positions (Fig-

a) P_{exc} = 1.75 mW
no depletion

a = 300 nm

1 µm

b) P_{exc} = 1.82 mW / no depletion

a = 500 nm   a = 400 nm   a = 300 nm

2 µm

c) P_{exc} = 1.76 mW

a = 175 nm

2 µm

0.08   0.16   0.32
depletion power (mW)
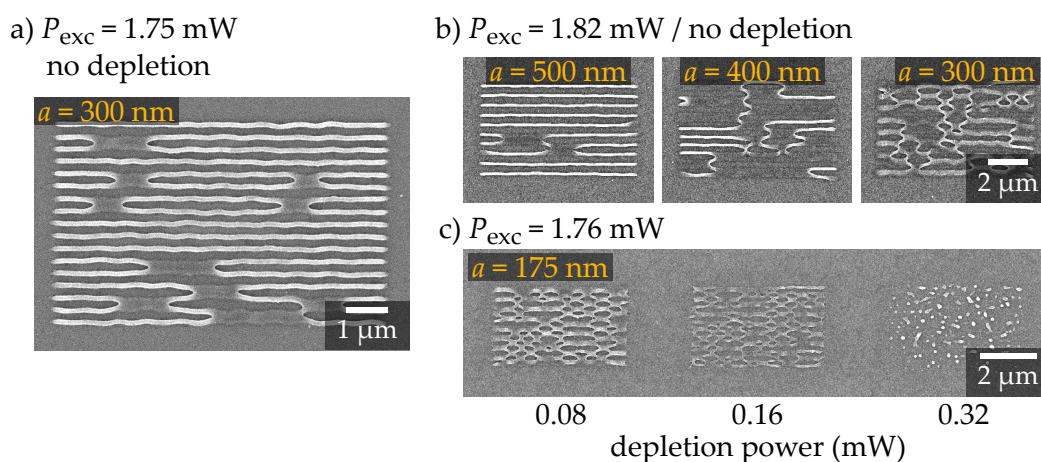
Figure 4.26: SEM images of grating structures written with different parameters. a) A grating written using only the excitation laser shows wiggly lines and microbridge formation. b) The number of microbridges increased for decreasing lattice constants. c) Using silanized cover glasses and the depletion laser allowed for resolving smaller lattice constants. Increasing the depletion laser power did not reduce the number of microbridges but led to deterioration of the grating structure.

ure 4.26 a)). These connections occur in the form of so-called microbridges connecting two neighboring lines with a thin strand or in the form of two lines having collapsed onto each other, called pattern collapse. The number of such connections increased for decreasing lattice constant (Figure 4.26 b)). Only gratings with lattice constants significantly above the diffraction limit of 177 nm were achieved without the occurrence of such microbridges. If the phase-modulated depletion laser and silanized substrates were used additionally partly resolved grating structures with $a = 175$ nm were feasible (Figure 4.26 c)). However, increasing the depletion power did not result in less microbridge formation or pattern collapse but rather in a continuous degradation of the structure, very similar to the transition towards disconnected lines in the single line experiments described above. Presumably, the microbridges were formed in the swollen state during the development step, when neighboring lines touched each other. A part of these non-covalent connections was retained during deswelling and drying of the sample. In other parts, the tension led to collapse of adjacent lines. Such defects have

been reported for many different photoresist systems across all kinds of microlithography processes [178–181]. For some methacrylate-based resists, this problem can be averted by employing very mild development conditions [182–184]. Although a wide variety of developer solvents and developing conditions was examined in that regard, no improvement could be found over a simple two-step development in toluene and isopropyl alcohol. Also, no improvement could be achieved by employing different photoresist compositions along the lines of Section 4.3.1. As I show in Section 5.4.2, very similar issues occurred for the spirothiopyran-based photoresist developed within this thesis. I compare the results in Chapter 6.

In conclusion, the 3D photoresist based on dimerization of photoenols presented in this section allowed for fabrication of 3D microstructures with feature sizes of less than 100 nm by two-photon excitation at 700 nm. An extensive study was performed in order to understand the influence of different copolymer and photoresist compositions and enabled the optimization of the photoresist. Employing depletion at 440 nm, linewidth could be reduced by 32 %, down to 51 nm. Both, single line experiments and fabrication of gratings suffered tremendously from lines detaching from the substrate and swelling effects during development, strongly limiting the achievable resolution. Yet, a clear and pronounced depletion effect was observed, proving that photoisomerization of intermediate-state photoenols can effectively suppress the dimerization reaction.

5

THE SPIROTHIOPYRAN MOLECULAR PHOTOSWITCH
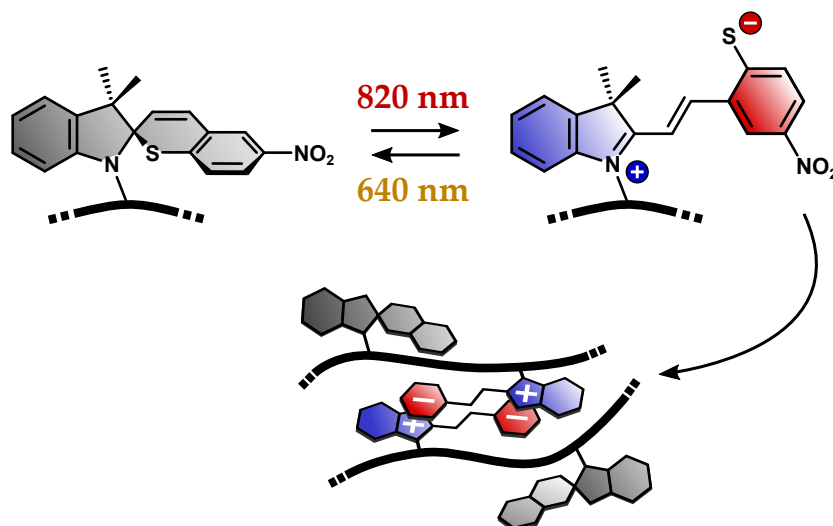
Excited spirothiopyrans undergo supramolecular linkage that can be suppressed by exposure at 640 nm.

Herein, I describe a molecular photoswitch which is based on photochromic spiro-thiopyran. After an introduction to the photochemistry of spirothiopyran, I present experiments on surface functionalization. A negative-tone photoresist based on methacrylate copolymers is described that allowed for fabrication of 3D structures. Finally, results on linewidth and resolution enhancement by depletion are shown and discussed.

5.1 Photochromism of Spirothiopyran

5.1.1 Photochromic Compounds

Materials that reversibly change their color upon stimulation by light are called *photochromic* materials [185]. They possess two (ideally) bistable forms A and B which can transit into each other by exposure to different wavelengths λ_1 and λ_2.

$$A \underset{\lambda_2}{\overset{\lambda_1}{\rightleftarrows}} B$$
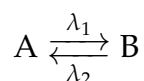
Typically, the starting material A is colorless and develops an absorption band in the visible range when converted into B by exposure to UV light, changing the perceived color. The change in the reverse direction, $B \to A$, can be induced photochemically, by absorption of visible light. In some materials, the change back into form A can be thermally induced as well. Common everyday examples for such materials are variable-tint lenses for glasses that darken in the sunlight.

With regard to organic compounds, photochromic chromophores can be divided into five major classes. Azobenzenes and chromenes rely on *cis-trans* photoisomerization for switching. Photochromism of diarylethenes, fulgides, and spiropyrans/-oxazines is based on unimolecular electrocyclization [185]. In many cases, it is not only the absorption spectrum that is changed but also other material properties connected to luminescence, dipole moment, or refractive index [186].

Photochromic molecules have been applied with great success in super-resolution microscopy. Their switching behavior fulfills the requirements for a molecular photoswitch necessary for sub-diffraction resolution (see Section 2.2.2). In super-resolution fluorescence microscopy, the use of photochromic derivatives of commonly employed fluorescent dyes [87, 88] or photochromic proteins [89–92] has allowed to decrease the necessary laser powers for the depletion beams in both STED-inspired microscopy and stochastic localization microscopy. Recently, a 4π-microscopy technique enabled imaging of living cells labeled with photochromic proteins with sub-diffraction resolution [187]. For lithographic applications, a limiting factor is that the huge change in optical properties is typically not accom-

panied by a change in reactivity. In interference lithography, photochromic diarylethenes have been used either as absorbance modulation layer on top of photoresists [127, 129] or directly as the photoresist material [130] enabling sub-diffraction feature size and resolution by performing multiple consecutive exposure steps. Regarding "writing" in the sense of recording information rather than structuring materials, the use of photochromic proteins enabled sub-diffraction recording and read-out both *via* STED-inspired microscopy [91].

5.1.2 SPIROPYRANS

The photochromic compounds used in this thesis stem from the family of spiropyrans that exist in two isomeric forms: ring-closed spiropyran (SP) or ring-opened merocyanine (MC). Spiropyrans have been studied extensively and have found numerous applications in different fields [188]. The structural formula of the ring-closed isomer shown in Figure 5.1 a) comprises an indoline and a chromene moiety that are oriented perpendicular with respect to each other and that are connected by a spiro carbon atom. Depending on the heteroatom in the chromene moiety, the compound is either referred to as spiropyran (SP) in the case of oxygen or spirothiopyran (STP) in the case of sulfur. In the following, I mainly refer to the second species, STP. Upon exposure to UV light, the C–S bond is cleaved, followed by a rotation about the central C–C bonds. The result is the planar MC form whereby the conjugated system of the two molecule fragments are connected. Therefore, the absorption band is red-shifted into the visible spectrum, typically around 600 nm, depending on the heteroatom, side groups and the environment (Figure 5.1 b)). The MC form can thermally fade back into the STP form, although interactions with other MC forms or solvent molecules can extend the lifetime to minutes or even hours [189], resulting in an effectively bistable system. The back reaction can be tremendously accelerated by exposure to light in the spectral range of the visible absorption band of the MC form. This switching behavior constitutes the molecular photoswitch that we will employ for lithography below.

The properties of the SP/STP and MC forms are vastly different not only with respect to the absorption spectrum. The MC form can be drawn as
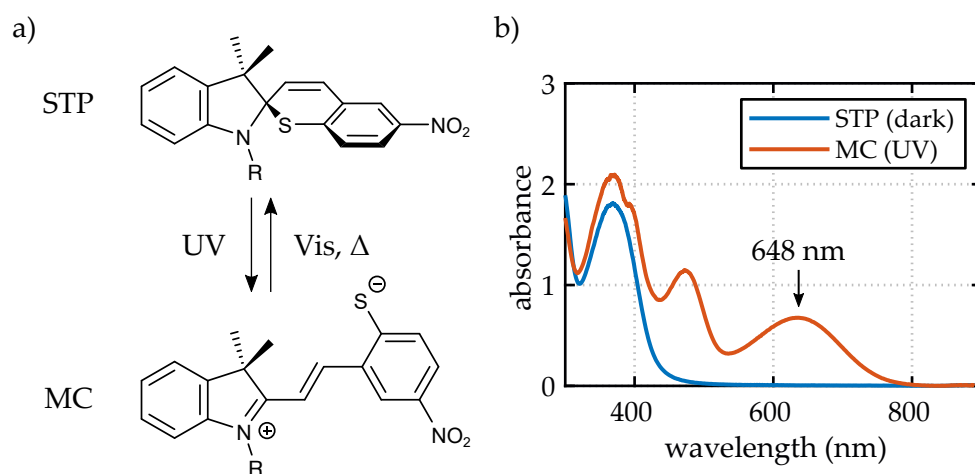
Figure 5.1: a) Schematic view of the photoisomerization of closed-form spirothiopyran (STP) into its open merocyanine (MC) form by UV light. The back-reaction can be thermally induced and enhanced by visible light. b) Absorbance spectra of STP (in dark) and MC (UV light, photostationary state) in DMSO (R = hydroxyethyl, $0.2\,\mathrm{mmol\,L^{-1}}$, $10\,\mathrm{mm}$ path length, measured by Larissa Hammer).

a zwitterionic resonance structure due to the charge separation between nitrogen and the heteroatom (oxygen for SP or sulfur for STP).[1] This leads to an increase in dipole moment by more than a factor of 4 from SP to MC [191]. While the closed form of SP is not luminescent, the open form shows strong fluorescence emission around 650 nm which was used for photoswitching of the fluorescence of nanoparticles [192]. Moreover, the two isomers occupy different volumes due to the large conformational change and differ in acidity [188].

Despite these large differences, an application of oxygen-containing SP for lithography is not straight-forward as the open form is not distinctly reactive. One possibility is to use the MC form as a switchable photosensitizer for a radical generator, which enables stepwise photoinitiation of free-radical polymerization [193, 194]. Irie and coworkers demonstrated that the change in dipole moment can be employed to alter the solubility of SP-carrying

---

[1] Strictly speaking, the MC form exists as a hybrid of a zwitterionic form and a quinoidal form without charge separation, depending on the solvent environment. For the STP species mainly used in this work, the zwitterionic form is predominant [190].

copolymers although the contrast was reported to be low [195]. The open MC form tends to form complex aggregates with other MC or SP moieties [196]. This behavior was exploited to achieve light-patterned adsorption of SP-functionalized silica nanoparticles onto SP-functionalized surfaces [197]. Further studies by the same authors demonstrated nanoparticle aggregation by UV light [198] and direct laser writing of porous colloidal nanostructures by means of two-photon absorption [199]. Still, directly inducing a covalent cross-linking reaction is not feasible using SP.

The situation is different for the sulfur-containing STP. Here, the open MC form features a thiolate anion which can undergo various reactions. Shiraishi and coworkers used STP as an additive in a suspension to trigger aggregation of gold nanoparticles by light [200]. Upon UV exposure, the generated thiolate anions bound to the nanoparticle *via* the strong sulfur-gold bond, changing the electronic charge of the surface and promoting aggregation. However, illumination with visible light did not degrade the aggregates as the stable gold-sulfur bond prevented the back reaction from MC to STP. Further, the thiolate anion can react *via* a thiol-Michael addition with a second molecule carrying an electron-deficient carbon double bond, *e. g.*, a maleimide or (meth)acrylate, resulting in a stable covalent bond (Figure 5.2). Thiol-Michael addition is a versatile reaction that is widely employed in different branches of chemistry and belongs to the class of *click* reactions featuring high yields of highly selective products at fast reaction speeds [160, 161]. Employing photoswitchable STP allows for precise sequential control over thiol-Michael reactions by varying the UV exposure in time or space [201]. STP incorporated into polymer chains has recently been used as a mechanophore leading to a color change of the polymer upon mechanical load [202]. The color change resulted from generation of MC forms which could further react *via* thiol-Michael addition with maleimide linkers encoding the mechanical load into the polymer network.

Vijayamohanan and coworkers have recently proposed to employ the STP chromophore for super-resolution laser lithography [203]. The proposed concept is based on a photoresist composed of copolymers bearing either STP moieties or maleimide functionalities as side groups. By UV exposure, the STP → MC transition (*excitation*) is triggered, generating a population of MC forms with thiolate anions that subsequently form intermolecular
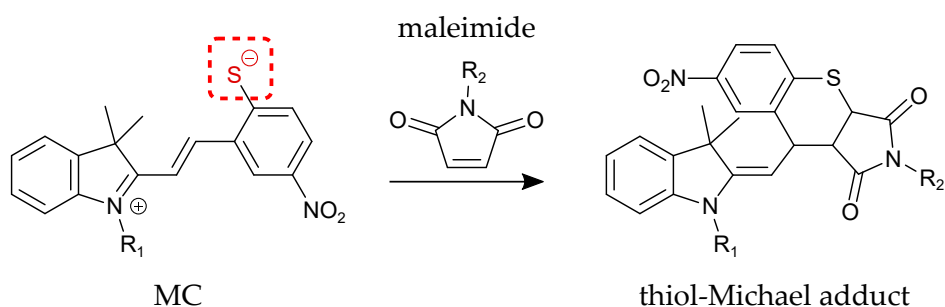
Figure 5.2: The MC form of STP features a thiolate anion (red) that can undergo a thiol-Michael reaction with a maleimide, forming a covalent linkage between the side groups R_1 and R_2.

cross-links by thiol-Michael addition with maleimides. The reaction can be suppressed by visible laser light, promoting the reverse MC $\rightarrow$ STP transition (*depletion*) and reducing the population of MC forms. The beam profile of the visible laser features points (or lines or planes) of zero intensity such that the thiol-Michael cross-link formation is confined to the vicinity of these points, similar to the concept of STED-inspired lithography. The authors have proved in macroscopic experiments that exposure of the photoresist to both UV and visible light in fact leads to a reduced reaction yield compared to exposure to UV light only. Furthermore, they have proposed the application of this technique in interference lithography and theoretically calculated the potential resolution increase without experimental demonstration.

An adoption of this approach for STED-inspired DLW requires efficient two-photon (or multi-photon) excitation of the STP chromophore. For the oxygen-containing analogue SP, a number of studies showed that the SP $\rightarrow$ MC transition can be efficiently triggered by two-photon absorption in the range of 700–800 nm, although the reported two-photon absorption cross sections vary [197, 199, 204–206]. Moreover, it was demonstrated that two-photon excitation of the MC form at these wavelengths leads to fluorescence, whereas the reverse transition from MC to SP does not take place in quantitative amount [207].

In the following, I present experiments that we conducted in order to employ the STP chromophore for STED-inspired DLW and demonstrate a resolution improvement in the microscale. First, surface functionalization experiments are described relying on thiol-Michael addition of MC groups

fixed on a surface and maleimide species in solution. Second, I discuss the results we obtained when developing a photoresist capable of supporting 3D structures based on methacrylate copolymers bearing STP side groups. To refer to the scheme for a molecular photoswitch introduced in Section 2.2.2, the unreactive state A is represented by the STP form, the reactive state B is the MC form, which can undergo an irreversible chemical reaction into state C, the reaction products. The chemical compounds used in these experiments were synthesized by Larissa Hammer and Rouven Müller (ITCP, KIT) who additionally recorded optical spectra and performed solvent studies. I prepared the photoresist mixtures and conducted the lithography experiments as well as the characterization of the samples. Eva Blasco (ITCP, KIT), Christopher Barner-Kowollik (ITCP, KIT), and Martin Wegener participated in planning of experiments and discussion of experimental results. The work on the STP-based 3D photoresist described in Section 5.4 was presented at a conference [208] and published in a peer-reviewed journal [139].

5.2 SURFACE FUNCTIONALIZATION

For surface functionalization experiments, sample processing followed Section 3.3.1. The STP-carrying triethoxysilane compound and the bromine-carrying maleimide species were synthesized by Larissa Hammer and are depicted in Figure 5.3. Glass substrates were coated with the STP-silane and inserted into the lithography setup. Based on the absorption spectra shown in Figure 5.1 b), we employed femtosecond laser pulses with a center wavelength of 750 nm for two-photon excitation of STP which is spectrally well separated from the visible absorption of the open MC form. For depletion, a cw laser diode at 640 nm was used (see Figure 3.1). It is well known in literature that the solvent has a strong influence on the switching dynamics of spiropyrans and merocyanines [188]. Therefore, it is necessary to carefully select a suitable solvent for the maleimide-bromine during the lithography step. Therefore, a series of solution experiments was performed by Larissa Hammer [209] before I conducted lithography experiments.

Finding the Right Solvent

Solutions of a STP compound (at $0.2\,\mathrm{mmol\,L^{-1}}$) in different solvents or solvent mixtures were first exposed to UV light at 385 nm to trigger the STP $\rightarrow$ MC transition. In parallel, the absorption spectrum was measured to determine the spectral position λ_{max} of the peak absorbance of the MC form in the visible range between 500 nm and 700 nm and the value of absorbance was taken as a (uncalibrated) proxy for the concentration of MC species. Results of the study are listed in Table 5.1. For the solvents DMF, acetonitrile, and anisole a decrease of MC absorbance as well as a spectral shift were observed for prolonged irradiation times >1 min which might be attributed to degradation or decomposition of the MC form in these solvents. This effect is quantified by the irradiation time $t_{10\%,\mathrm{UV}}$ after which the absorbance has decreased down to 10 % of the maximum value. DMSO and a mixture of DMF and water (1 : 1 vol%) did not show such degradation. Further, all solutions were excited by brief exposure to UV light (avoiding the degradation regime) and the decrease of MC absorbance was monitored as the MC forms were thermally converted back into SP. In

spirothiopyran-silane · · · · · · · · maleimide-bromine

Figure 5.3: Schematic view of a) STP-carrying triethoxysilane and b) maleimide-bromine.

parallel experiments, the photo-induced back-conversion was recorded under exposure to a visible light LED with 590 nm peak emission wavelength. The corresponding times necessary for an absorbance decrease down to 10 % of the maximum are denoted by $t_{10\%,\text{therm}}$ and $t_{10\%,\text{Vis}}$, respectively. The data clearly shows that the light-induced MC $\rightarrow$ STP transition is much faster than thermal relaxation, typically by a factor of 50. In Table 5.1, the relative polarity of each solvent is denoted by Reichardt's normalized solvatochromic indicator $E_T^N(30)$ [210]. Evidently, MC forms are stabilized in polar solvents by dipolar interactions and hydrogen-bonding, leading to a hypsochromic shift (blue shift) of λ_{max} as well as longer MC lifetimes for both thermal and light-induced isomerization.

To avoid degradation, writing experiments were only assessed using DMSO or the DMF/water mixture as a solvent for the maleimide-bromine at a concentration of $10\,\text{mmol}\,\text{L}^{-1}$. All further processing steps were identical for both solvents. After lithography, PEGMEMA polymer brushes were grown on the samples by ATRP and characterized by light microscopy and AFM (see Section 3.3.1). However, samples processed using the DMF/water mixture suffered from discontinuous polymer brushes with high surface roughness (not depicted). Possibly, this was caused by water condensating on the areas decorated with MC forms. As the thiol-Michael reaction

Table 5.1: Results of the solvent study performed by Larissa Hammer [209].

solvent	$E_T^N(30)$	$\lambda_{\max}$ (nm)	$t_{10\%,UV}$ (s)	$t_{10\%,therm}$	$t_{10\%,Vis}(s)$
DMF/H$_2$O (1 : 1)	0.599[1]	564	-	6.5 h	80
DMSO	0.444[2]	648	-	80 min	80
acetonitrile	0.460[2]	643	20	110 s	1.5
DMF	0.386[2]	648	25	7 min	2
anisole	0.198[2]	700	40	50 s	1

[1] Value reported in [211].
[2] Values reported in [210].

does not proceed efficiently in pure water, these areas were not uniformly functionalized with maleimide-bromine.

In contrast, samples processed using a solution of maleimide-bromine in DMSO showed clearly defined structures with good quality. Figure 5.4 a) depicts a light microscope image of a dose test pattern consisting of lines written at a scan speed of $100\,\mu m\,s^{-1}$ with varying excitation power and at different offsets with respect to the sample interface. An AFM image of a part of such a pattern reveals increasing line height and linewidth which can be explained by similar saturation effects as already discussed in Section 4.2.

In order to investigate the expected depletion effect, experiments were performed using overlaid Gaussian laser beams. A pattern was written consisting of several lines each of which was exposed to a different set of excitation and depletion laser powers. In Figure 5.5, a light microscope image of a typical result is depicted. Evidently, writing is not suppressed by the depletion light. Instead, the depletion light even enhances writing. Compared to not using depletion, lines can be observed at even lower excitation powers if the depletion laser is switched on (dashed area A). The MC form apparently did not efficiently revert back into the STP form by exposure to the depletion light. At even higher depletion laser powers, the depletion laser light alone led to parasitic writing (dashed area B) which we attribute to residual absorption of STP at that wavelength. If the absorption spectrum shown in Figure 5.1 b) is plotted on a logarithmic scale (Figure 5.6), it becomes clear that the absorbance of the STP form at 640 nm is non-zero and lies two orders of magnitude lower than for the MC form in
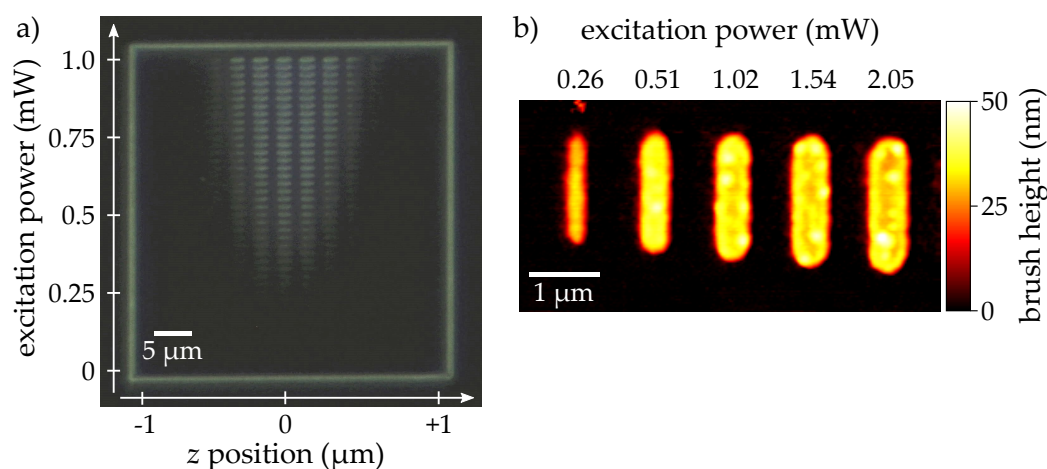
Figure 5.4: a) Dark field light microscope image of polymer brushes grown on lithographically defined functionalized patterns. The contrast of the lines increases with rising excitation power. b) An AFM image of a similar pattern reveals that both line width and height increase with rising excitation power. The height is limited by saturation effects.

the photostationary state under UV illumination.

Given the huge evidence of efficient photoswitching of SP and STP reported in literature, we attempted further experiments in solution as well as under lithography conditions. A study performed by Larissa Hammer aimed for determining the thiol-Michael reaction yield in equimolar solutions of a STP species and maleimide-bromine in DMSO under different illumination conditions by nuclear magnetic resonance (NMR) measurements [209]. After 90 min exposure to an UV LED at 385 nm, 38 % of the initial STP molecules underwent a thiol-Michael addition in one sample. A second sample simultaneously irradiated by UV and visible light (LED with peak emission at 590 nm) showed a decreased reaction yield of 19 %, which proved that the depletion effect is very pronounced, even in the presence of thiol-Michael reaction partners, *i.e.,* maleimides. In a third control sample exposed to only the visible LED, conversion of STP by thiol-Michael addition could not be detected at all. Several different approaches were assessed in order to achieve a similar depletion effect in lithography experiments. The use of other solvents than DMSO listed in Table 5.1 led to deteriorated structures that did not allow to draw conclusions on the depletion effect. Further,
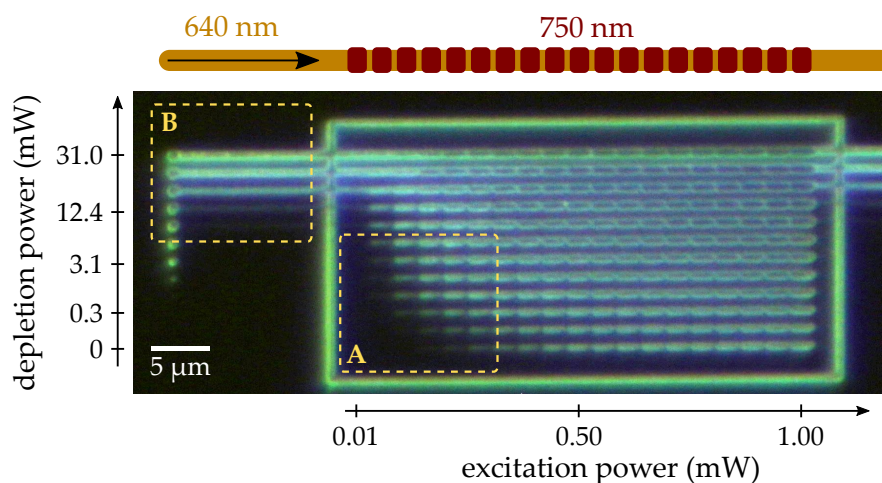
Figure 5.5: Dark field light micrograph of a depletion test pattern where each horizontal set of lines was written as indicated in the scheme shown on top. While the depletion laser was at a fixed power for the whole line, small lines were written with increasing excitation laser power. With increasing depletion power, lower excitation powers were needed to achieve visible lines (dashed area A). At very high depletion powers, the depletion laser writes even without excitation light (parasitic writing, dashed area B).
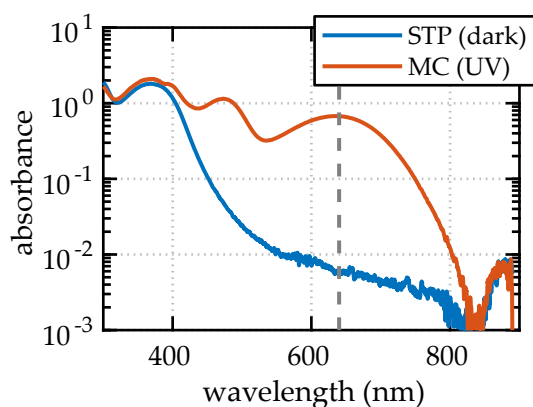
Figure 5.6: Logarithmic plot of the absorbance spectrum of a small STP species in DMSO shown in Figure 5.1 b). The gray dashed line indicates the spectral position of the depletion laser, *i.e.*, 640 nm.

attempting depletion at a shorter wavelength of 532 nm did not lead to an improvement. The influence of the concentration of maleimide-bromine was investigated as well and showed that at concentrations below $3.3\,\mathrm{mmol\,L^{-1}}$ no writing takes place. A possible oversaturation by maleimide species can therefore be ruled out as well.

These results led us to the conclusion that the absence of depletion in our lithography experiments must be connected to the STP being attached to a glass surface. Due to the large conformational changes involved, the conversion from STP to MC and vice versa is sensitive to steric effects [212–214]. Presumably, the MC $\rightarrow$ STP transition is not only sterically hindered but in addition suppressed as the MC forms are stabilized by aggregating with neighboring MC moieties or by the polar solvent DMSO. Rosario *et al.* reported similar findings for surface-bound SP-carrying silane [213]. The authors found an improved switching behavior if the SP-carrying silane was diluted by a second unpolar silane species prior to silanization. In our experiments, we therefore assessed the dilution the STP silane by addition of triethoxy(octyl)silane. Unfortunately, this approach did not prove suitable for lithography experiments. The dilution of STP silane resulted in a lower grafting density of MC forms and therefore led to a lower bromine density on the surface. This is detrimental to the requirement of high initiator densities for achieving high polymer brushes (compare to Section 4.2). With increasing STP dilution employed in our experiments, the the height of the polymer brushes became too low to be effectively measurable anymore by our means before we could detect a clear depletion effect.

Therefore, we draw the conclusion that the approach of surface functionalization did not allow to observe the expected depletion effect of the STP chromophore. While this technique proved successful for characterizing the photoenol molecular photoswitch (see Section 4.2), the STP chromophore is more sensitive to the environment, presumably due to the large steric changes involved in the isomerization process.

5.3 SPIROTHIOPYRAN-BASED NEGATIVE-TONE PHOTORESISTS

In order to achieve a photoresist that allows for 3D structures, we followed the route of attaching STP moieties to the side groups of methacrylate copolymers. This approach is analogous to the work presented in Section 4.3 on the photoenol molecular photoswitch. Different methacrylate-based copolymers with either STP or maleimide functionalities as side groups were synthesized by Larissa Hammer and Rouven Müller by thermal copolymerization of methyl methacrylate (MMA) and previously synthesized STP-carrying methacrylate (STPMA) or protected maleimide-carrying methacrylate (MALMA), respectively [139, 209]. Figure 5.7 a) shows the chemical structures of the employed copolymers while their compositions and number average molecular weights M_n are listed in Table 5.2. Upon two-photon absorption in the near infrared, the STP moieties photoisomerize into their MC forms. The reverse MC $\rightarrow$ STP transition is stimulated by one-photon absorption of visible light [215]. First, I describe experiments on a two-component photoresist relying on thiol-Michael addition for cross-linking between STP- and maleimide-functionalized copolymers. After that, I show how an interesting discovery allowed us to simplify the photoresist to only a

Table 5.2: Compositions of the different copolymers.

copolymer	M_n[1] ($\mathrm{g\,mol^{-1}}$)	STPMA[2] (mol%)	MMA[3] (mol%)	MALMA[4] (mol%)
STP-1	6100	14	86	-
STP-2	7600	27	73	-
STP-3	8600	56	44	-
STP-4	44000	7	93	-
Mal-Pol	6700	-	84	16

Molar ratios determined by NMR measurements.
[1] Measured by size-exclusion chromatography [139, 209].
[2] STP-functionalized MMA.
[3] Methyl methacrylate.
[4] Methacrylate bearing protected maleimide. Deprotection followed directly after copolymer synthesis [209].

a)

b)
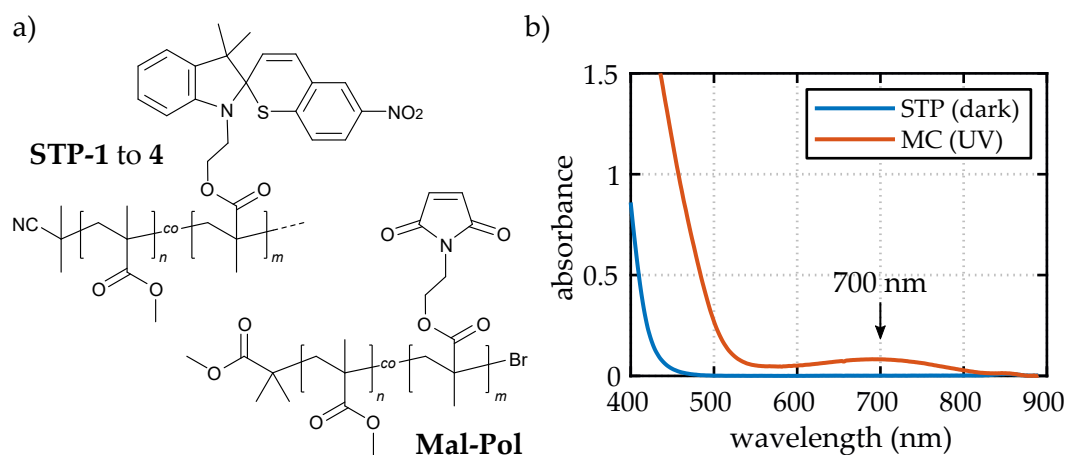
Figure 5.7: a) Schemes of STP-carrying methacrylate copolymers and the maleimide-carrying methacrylate copolymer. The compositions of the copolymers are given in Table 5.2. b) Absorbance spectra of **STP-1** in acetophenone in the dark and in the photostationary state under exposure to UV light (4.1 mg ml^{-1}, 2 mm path length, measured by Rouven Müller). Adapted from [139].

single constituting compound, based on supramolecular link formation. In both cases, a negative-tone photoresist capable of supporting 3D structures was obtained.

Figure 5.7 b) depicts the absorption spectra of the STP copolymer **STP-1** dissolved in acetophenone at 4.1 mg ml^{-1} in dark and in the photostationary state under UV illumination. Compared to the small molecule spectrum shown above in Figure 5.1, the absorption peak of the MC form is red-shifted to a spectral position of $\lambda_{\mathrm{max}} = 700$ nm, presumably due to the lower polarity of acetophenone compared to DMSO. While the depletion wavelength of 640 nm previously used for the surface functionalization experiments was still suitable, we tuned the titanium-sapphire excitation laser to 820 nm in order to reduce overlap with the absorption of the MC form. The employed laser foci are depicted in Figure 3.6.

5.3.1 3D Photoresist Based on Thiol-Michael Addition

In a first set of experiments, we employed a photoresist consisting of copolymers bearing STP units and copolymers bearing maleimide moieties. By thiol-Michael addition of thiolate anions and maleimides, covalent cross-links are formed between the copolymer chains. Thus, a polymer network is formed in a step growth manner within the exposed volume. The cross-linking can be suppressed by simultaneous exposure to visible light which stimulates the conversion of MC back into STP before cross-link formation can occur. Generally, sample processing followed the procedure described in Section 3.3.2. The photoresist was prepared as a mixture of the STP copolymer **STP-4**[2] (31.5 mg, 0.7 µmol) and the maleimide copolymer **Mal-Pol** (20.6 mg, 3.1 µmol) at 25 wt% in acetophenone and DMSO (1 : 1 vol%). By warming to 40 °C and ultrasonication, a homogeneous mixture was achieved within 20 min. The system of two solvents was necessary to dissolve both copolymers sufficientlyand thus achieve concentrations above 10 wt%. The molar ratio of maleimide to STP functional groups was 1.5 : 1. A droplet of the photoresist was placed onto a cleaned glass cover slip, retained by a PDMS ring and inserted into the DLW setup. After lithography, samples were developed by immersion in toluene for typically 5 min, followed by immersion into isopropyl alcohol which is a non-solvent for the copolymers. Afterwards, the samples were dried in a stream of nitrogen.

The photoresist proved writable and allowed for fabrication of quasi-2D patterns on the substrate as well as free-standing 3D structures. The writing threshold power was 1.13 mW. SEM images of exemplary 3D structures are shown in Figure 5.8 a). Evidently, the structures suffer from very pronounced shrinkage as indicated by the dashed lines outlining the actually exposed volume. Dented side faces contribute to the rather bad overall structure quality. Presumably, the cross-linking density was very low and thus much unused photoresist material initially resided inside the structures. During development this surplus material was washed out leading to deteriorations during drying. Further, the structures are covered by small grains which we attribute to partial fallout of the photoresist solution.

---

[2] The reason for this particular choice was that this copolymer was the only one available at the time.
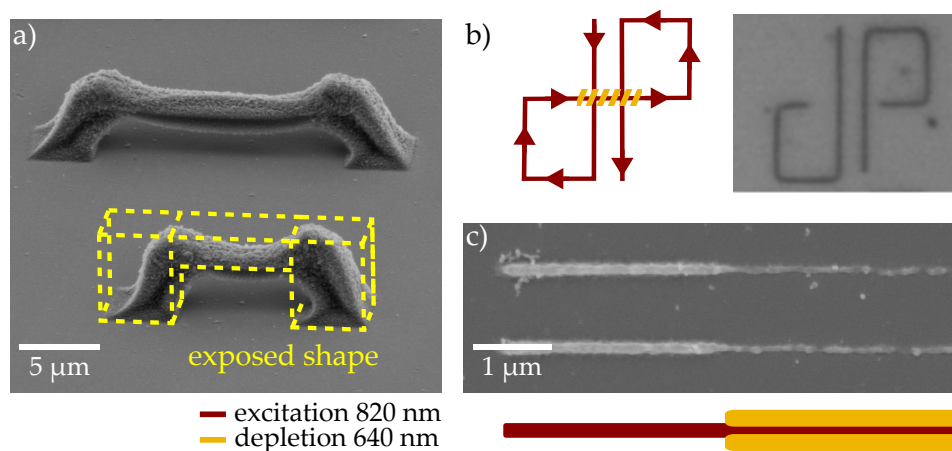
Figure 5.8: Writing results using the two-component photoresist. a) A SEM image of free-standing bridge structures reveals shrinkage-induced deteriorations. b) Using a Gaussian depletion beam, the schematically depicted loop test pattern was written. A light microscope image of the resulting structure shows that a reversible depletion effect has been achieved. c) SEM image of a depletion experiment using a phase mask-modulated depletion beam. Adapted from [139, 208]

For assessing the suppression of the cross-linking reaction by the depletion laser light, both excitation and depletion laser were employed with overlaid Gaussian foci (Figure 3.6). Loop patterns were written according to the scheme depicted in Figure 5.8 b), similar to experiments already described for the photoenol system in Section 4.3. The depletion beam was switched on for the central part of the line, which completely suppressed writing. The depletion laser thereby neither damaged previously written lines nor rendered an area unwritable for later exposures by the writing laser. This behavior was achieved for depletion powers ranging over two orders of magnitude. The achievable resolution in STED-inspired DLW scales with the inverse square root of the depletion power (see Equation 2.14) and as such an improvement of $\sqrt{100} = 10$ can be expected. Unfortunately, the bad quality of the structures ruled out an unambiguous assessment of this theoretical improvement. In fact, the inherent graininess of the fabricated structures became even more prevalent when going to small isolated lines, as shown in Figure 5.8 c). By modulating the depletion beam using a half-space phase

mask, a depletion focus featuring a plane of zero intensity was achieved (Figure 3.6) which was switched on for the right halves of the depicted lines. While the depletion light clearly led to linewidth reduction, the lines suffer from discontinuities and deteriorations and do not allow a clear determination of linewidth. Thus, the photoresist composition based on two copolymer components and two solvents was not suitable for high-resolution experiments.

5.4 3D PHOTORESIST BASED ON SUPRAMOLECULAR AGGREGATION

While the described experiments using the two-component photoresist were hampered by the bad structure quality, an unexpected discovery opened up a promising avenue. We found that the STP copolymers could also be structured when the copolymers bearing maleimide groups were left out of the photoresist mixture altogether. This simplification allowed to settle for acetophenone as the exclusive solvent and to increase the copolymer load in the solution up to several tens in weight percentage. Furthermore, the quality of the written structures improved considerably compared to the two-component approach while the sample processing procedure remained unchanged. Figure 5.9 shows SEM images of several well-defined 3D microstructures fabricated using a photoresist consisting of the STP copolymer **STP-1** at 40 wt% in acetophenone. The structures still exhibit shrinkage due to unused material being washed out during the development step but at a significantly reduced level compared to the structures depicted in Figure 5.8. The writing threshold power was 0.46 mW.
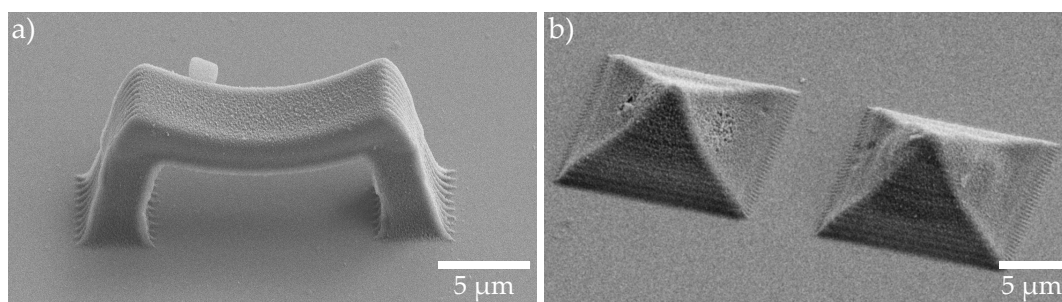
Figure 5.9: SEM images of a) a free-standing bridge structure and b) pyramid structures written using a photoresist composed of copolymer **STP-1** in acetophenone at 40 wt%. Adapted from [139].

5.4.1 CHARACTERIZING THE PHOTORESIST

Identifying the Cross-Linking Mechanism

As there is no activated ene present in the photoresist which could act as a suitable reaction partner for the thiolate anion, the above-described thiol-Michael reaction cannot account for the cross-link formation. Instead, we attribute the formation of stable structures to supramolecular interactions of MC and STP groups. As already explained in Section 5.1.2, the open MC form features an increased dipole moment compared to the closed form. For the oxygen-containing SP, Krongauz *et al.* were the first to report that the corresponding MC form can form strong intermolecular linkages [196]. They observed aggregation of small SP molecules into microscale structures induced by formation of SP-MC dimers and charge-transfer complexes. Later studies along the same lines described aggregates of type SP-MC, MC_n, and (SP_nMC_m) [216–219]. Using methacrylate copolymers bearing SP moieties, inducing intermolecular links by a mechanism termed *zipper polymerization* led to polymer crystals which were stable up to temperatures of $150\,°C$ [220–223]. Similar mechanisms were exploited for lithographically defined adsorption or aggregation of SP-decorated nanoparticles as already listed in Section 5.1.2 [197–199]. In order to validate this interpretation of our experimental results, Rouven Müller synthesized methacrylate copolymer bearing oxygen-containing SP in the side groups, **SP-1**, with a composition similar to **STP-1** (Figure 5.10 a), $M_n = 7300\,g\,mol^{-1}$, 16 mol% SP) [139]. A photoresist was prepared by mixing the SP copolymer at 40 wt% with acetophenone and tested by performing DLW experiments. The photoresist exhibited very similar writing performance, structure quality, and shrinkage effects compared to the photoresist based on STP copolymer. A SEM image of a bridge structure obtained using the SP photoresist is shown in Figure 5.10 c). The writing threshold power was 3.84 mW, which is a factor of 8.3 above the the value obtained for **STP-1**. While functionalization degree, molecular weight and concentration are very similar in both photoresists, this huge difference can be explained by the blue-shifted UV absorption of SP (Figure 5.10 b). In fact, tuning the excitation laser to shorter wavelengths lead to a decrease in threshold power. The cause for this blue-shift lies in the higher electronegativity of the oxygen heteroatom compared to
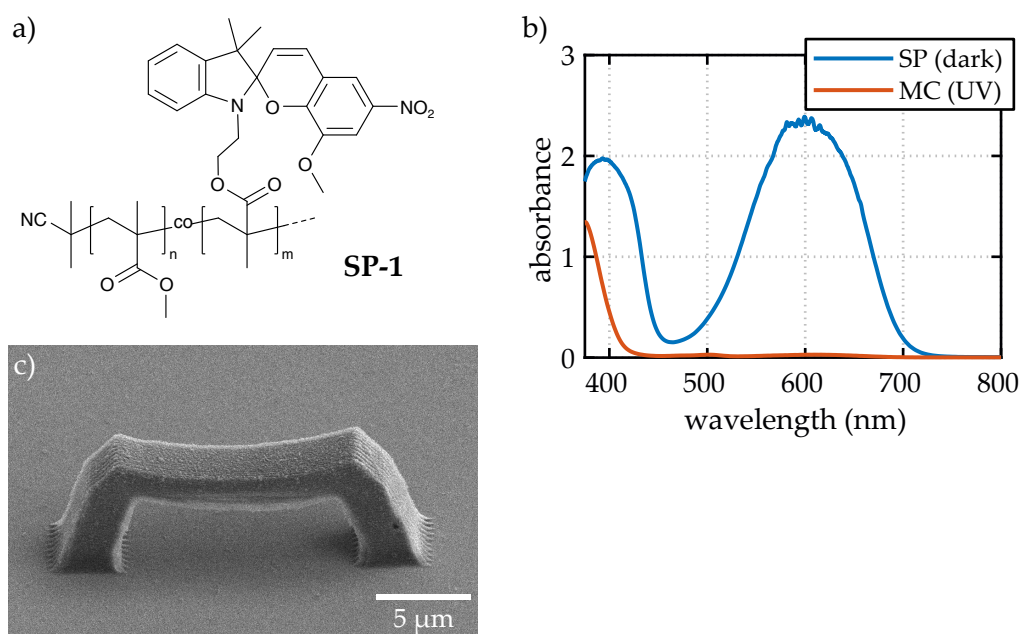
Figure 5.10: a) Scheme of the employed copolymers bearing oxygen-containing spiropyran. b) Absorbance spectra of **SP-1** in acetophenone in dark and in the photostationary state under UV illumination ($1\,mg\,ml^{-1}$, $2\,mm$ path length, measured by Rouven Müller). (c) SEM image of a free-standing bridge structure fabricated from a photoresist consisting of SP copolymer at $40\,wt\%$ in acetophenone. Adapted from [139].

sulfur [224]. Therefore, we attribute the formation of stable 3D structures in both the STP and SP photoresist to a combination of the strong supramolecular interactions described above leading to intermolecular aggregation and thereby to physically linked networks. As shown below, writing inhibition by the depletion laser could be achieved for the STP photoresist but not for the SP photoresist. Therefore, experiments using the SP copolymers were discontinued.

The non-covalent cross-link mechanism explains issues arising in the fabrication of more complex 3D structures than the ones shown in Figure 5.9. The structures often collapsed during development because the photoresist became too soft when swollen by the developer. Evidently, the non-covalent binding can be weakened by solvent intrusion. Similar findings were reported for aggregated SP-decorated nanoparticles [199]. Moreover, with

increasing structure volume, an increasing amount of small grains attached to the structures obscuring the exposed shape. Presumably, material from the photoresist solution agglomerated onto the structures by similar supramolecular interactions.

Investigating Different Copolymer Compositions

The copolymers **STP-1** to **STP-4** vary either in degree of functionalization, *i.e.*, the molar percentage of STP units, or chain length, given by the number average molecular weight M_n. Additionally, the maximum concentration achievable in acetophenone depends on these parameters. To find the ideal conditions, we assessed the writing performance of different photoresist mixtures. The results of this study are listed in Table 5.3. Generally, we could observe very similar trends as already described for the photoenol photoresists investigated in Section 4.3.1. While the copolymer with the longest average chain length, **STP-4**, showed the overall lowest threshold power, the 3D structures suffered more heavily from shrinkage and achievable resolution (using only the excitation laser) was lowest. This can be explained by considering the network formation process. With each cross-link formed, the total weight of the polymer network approximately[3] increases by the weight of a single copolymer chain. The gelation point, *i.e.*, the writing threshold, is crossed once the network achieves a certain molecular weight. Thus, using longer copolymer chains, less cross-links are necessary to reach this point, which leads to a decreased threshold laser power. On the other hand, the cross-linking density is also lower at the gelation point for longer copolymers, leading to a softer resist and more material being washed out during development [175]. The copolymers **STP-2** and **STP-3** possess roughly two and three times as many STP units compared to **STP-1**. The higher chromophore density theoretically leads to a higher cross-link density. In practice, there is a trade-off as the solubility of highly-functionalized copolymers is lower and switching of STP groups might be sterically hindered [223]. While initially well dissolved, photoresists containing **STP-2** or **STP-3** suffered from fallout during typical writing times of 1 h per sample. We also investigated different

---

[3] Here, it is assumed that each link is formed between two units that are not already linked. In reality, multiple inter- and intramolecular links could be formed.

Table 5.3: Comparison of the different STP copolymers. Adapted from [139].

copolymer	M_n (g mol^{-1})	STP content (mol%)	c_{max}[1] (wt%)	P_{thr}[2] (mW)
STP-1	6100	14	40	0.46
STP-2	7600	27	30	0.36
STP-3	8600	56	15	0.72
STP-4	44000	7	30	0.33

[1] Highest achievable concentration in acetophenone.
[2] Threshold laser power at c_{max}.

solvents, however, acetophenone proved to allow for highest concentrations and possesses a high boiling point which avoids changing concentrations and fallout during lithography experiments. The aforementioned photoresist consisting of copolymer **STP-1** at 40 wt% in acetophenone exhibited the best writing performance and was thus chosen for further experiments.

Effective Order of Nonlinearity

The effective nonlinearity N of the process was determined by imposing super-pulsing schemes onto the excitation laser and determining the threshold power for each set of pulse scheme parameters. This method was employed for the photoenol-based photoresists as well and is described in detail in Section 4.3.2. The effective order of nonlinearity was determined from a linear regression of a double-log plot of threshold power in dependency of the duty cycle of the super-pulsing scheme (Figure 5.11). The obtained value of $N = 1.84$ is in agreement with the two-photon behavior that is expected for a process based on two-photon absorption. Deviations from the theoretical value of 2.0 can be attributed to further non-optical nonlinearities occurring in the complex process of network formation.
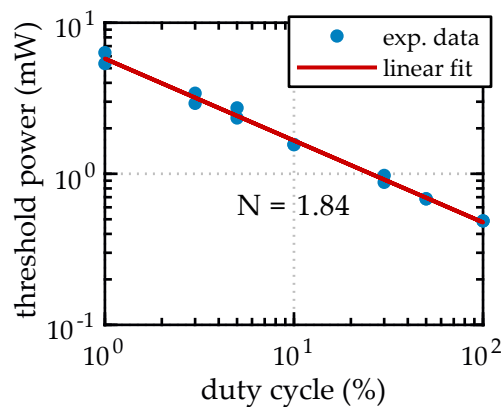
Figure 5.11: Double-log plot of polymerization threshold in dependence of super-pulse duty cycle. The negative inverse of the slope calculated by linear regression yields the effective order of nonlinearity $N = 1.84$. Adapted from [139].
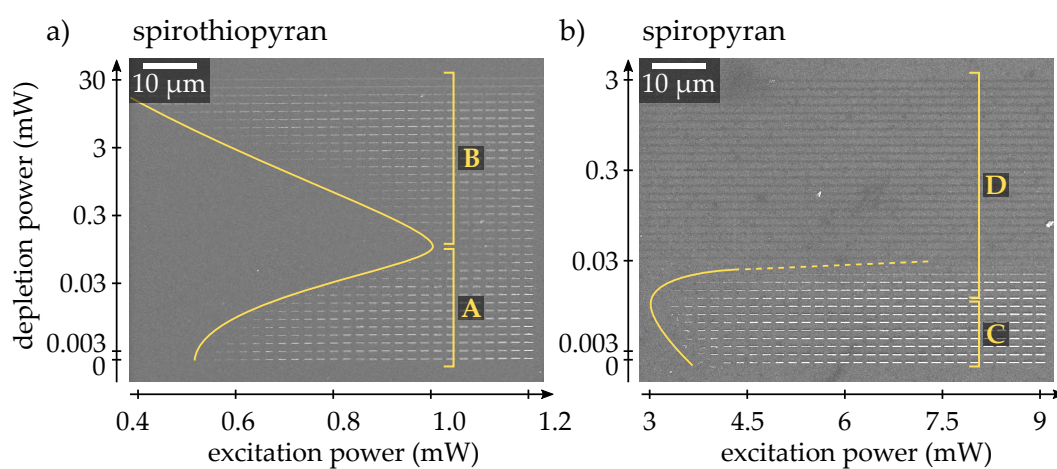
Figure 5.12: SEM images of depletion test patterns fabricated using a) the STP-based photoresist, and b) the SP-based photoresist. For each combination of excitation and depletion power, a line was written. The yellow lines are a guide to the eye. Different regimes can be identified: depletion (A), parasitic writing (B and C), and a destructive regime (D). Adapted from [139].

5.4.2 DEPLETION EXPERIMENTS

For proving the expected cross-linking suppression by depletion, overlaid Gaussian foci were employed (Figure 3.6). Excitation and depletion laser powers were varied and a line was written for each combination, resulting in patterns as depicted in Figure 5.12. Here, the best-performing STP photoresist based on **STP-1** is compared with the oxygen-analogue **SP-1** at the same concentration. Evidently, while the two photoresists showed similar results when using only the excitation laser (see above), a very different behavior was observed when the depletion laser power was increased. For the STP-based resist, the threshold power first increases with rising depletion power because the cross-linking is suppressed by the depletion light converting MC to STP (regime A). Thus, higher concentrations of MC forms are necessary requiring higher excitation powers. Above depletion powers of approximately 0.3 mW, the threshold power decreases again (regime B). We attribute this to parasitic one-photon absorption of the depletion laser by the STP form. This phenomenon can also be observed for other resist systems, *e. g.*, acrylate photoresists [106], or the photoenol-based resist described in Section 4.3.3. Nonetheless, a considerable window remains for depletion. The picture looks quite different for the oxygen-containing SP-based photoresist. Here, using low depletion powers in the microwatt range leads to a decrease in threshold power, indicating parasitic writing (regime C). Above a depletion power of 10 µW, the threshold increases again. However, this is accompanied by increasing degradation of the lines (indicated by the lower contrast in SEM) until there are no cross-linked lines visible anymore (regime D). This destructive effect was irreversible and also affected previously written lines. The cause for these differences between STP- and SP-based photoresists was not investigated in detail but can possibly be explained by looking at the MC $\rightarrow$ SP/STP transition which takes place *via* singlet-excited MC* [207]. From MC*, three pathways are possible, transition back in to the MC state by fluorescence or radiation-less decay, or (radiation-less) conversion into SP/STP. The MC form of STP is reported to exhibit much weaker fluorescence than its analogous SP, while radiation-less deactivation processes are more pronounced, presumably including transition from MC* into the STP form [225, 226]. Therefore, the formation of STP by the depletion light is

expected to be more efficient than the formation of SP. Furthermore, the equilibrium between SP/STP and MC forms in the photostationary state is shifted more towards the MC form for oxygen-containing SP than for STP [215, 224]. Thus, for SP, a higher concentration of MC forms is obtained in an exposed volume, which requires higher depletion laser powers, potentially closing down the working window for an efficient depletion effect. We therefore concluded that the SP-based photoresist does not offer a depletion channel suitable for this lithography approach and continued further depletion experiments using only the STP-based photoresist.[4]

Reversible Depletion

By writing loop patterns as schematically depicted in Figure 5.13, the reversibility of the depletion effect was investigated. The result proves the two necessary prerequisites for a useful depletion effect. First, lines that had been previously written were not affected by the depletion light (dashed area A). The dipolar interactions forming the cross-links in the structures are stable enough to withstand the depletion laser beam. Second, after an area had seen the depletion light, it was possible to write in that area again, *i.e.*, the depletion effect is reversible (dashed area B).

Similar to Section 4.2.1, it is possible to estimate the lifetime of the MC form in the photoresist during lithography experiments. Therefore, point exposures were performed with overlaid excitation and depletion lasers. A time-gating scheme as depicted in Figure 5.14 a) was imposed onto the lasers by electronically gating the AOM or the diode current, respectively. Both beams were switched on for a single super-pulse of $2\,\mu s$ each with time delay Δt between the excitation and the depletion super-pulse. For each time delay, a series of points was exposed with a fixed depletion power of $29\,mW$ and with increasing excitation power. The threshold excitation power P_{thr} was determined for each Δt by inspection of the sample in a dark-field light microscope. The dependency of the writing threshold power on the pulse delay is depicted in Figure 5.14 b). At $\Delta t = -4\,\mu s$, the depletion had no

---

[4] It is worth revisiting the results obtained using the two-component photoresist (see Section 5.3.1) at this point. While the thiol-Michael addition is an efficient and preferable reaction pathway, it cannot be ruled out that the supramolecular interactions described herein contributed to network formation for the two-component system as well.

excitation beam switched on
depletion beam switched on
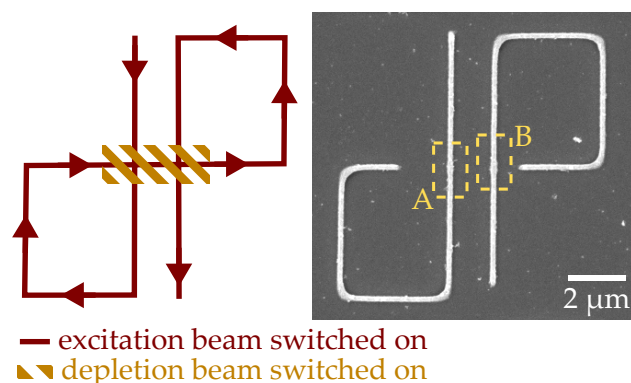
Figure 5.13: Loop pattern written for assessing the reversibility of the depletion effect, shown schematically (left) and in a SEM image of a written structure (right). Neither previously written lines (dashed area A) were affected nor was the depleted area rendered unwritable by the depletion light (dashed area B), proving a reversible depletion effect. Adapted from [139].

effect and the threshold power was 21.1 mW. Around $\Delta t = 0$, the threshold shift due to the depletion peaked at 35.1 mW, corresponding to a threshold shift of 66 %. At time delays of more than about 2 µs, the threshold power returned to a constant level of 22.5 mW, indicating that the depletion was not effective anymore after that time. Presumably, the majority of molecules in the MC state had already undergone irreversible linkage formation and could therefore not be converted back into STP. To quantify the decay of the threshold, the data is fitted by an exponential which yields a 1/e decay time of $\tau = 0.95$ µs. This value is lower than the super-pulse width of 2 µs and should therefore be only regarded as an upper limit to the MC lifetime. Employing shorter super-pulses was not feasible as due to electronic limitations.

Linewidth Enhancement by Depletion

With a reversible depletion effect at hand, we subsequently explored achievable linewidth enhancement and resolution increase in high-resolution experiments. Therefore, the depletion beam was modulated by a half-space phase mask to achieve a focus shape featuring a plane of zero intensity (Figure 3.6). Test patterns fabricated for assessment of the linewidth en-

a)

exposure scheme:

b)
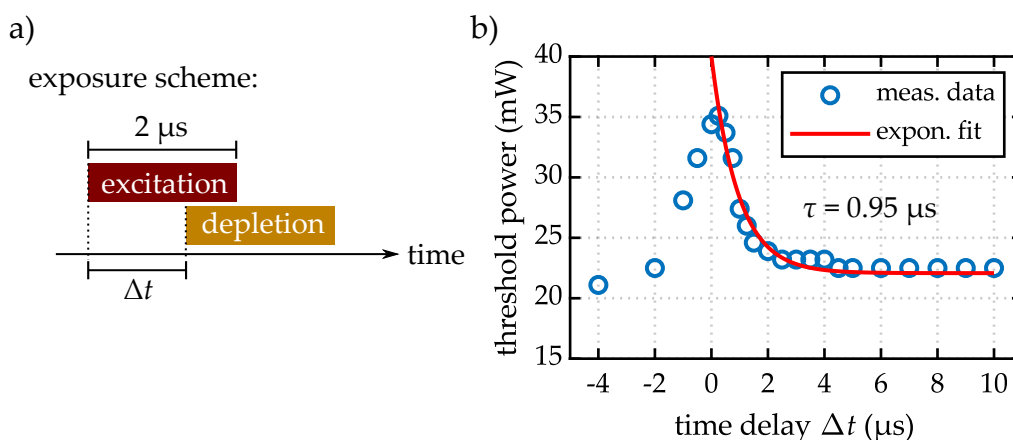
Figure 5.14: a) Exposure scheme employed for determination of the lifetime of the MC form by point exposures. Excitation and depletion lasers are super-pulsed by gating the AOM and the diode current, respectively, with pulse widths of 2 μs and shifted by a time delay Δt. b) The threshold laser power is determined for each time delay Δt, at a fixed depletion power of 29 mW. An exponential fit for positive Δt reveals a 1/e decay time of $\tau = 0.95$ μs.

hancement consisted of sets of lines written with a fixed excitation laser power, where the depletion laser was switched on for a part of the line. From line to line, the depletion power was increased. The SEM image depicted in Figure 5.15 a) shows a set of lines written with an excitation power of 0.69 mW and depletion laser powers in the range of 1.3–2.7 mW. Evidently, the linewidth is decreasing with increasing depletion laser power until the lines become discontinuous at some point. The linewidth is determined from the gray value of the SEM image by averaging the line profiles along a section of the line, as indicated by the dashed box in Figure 5.15 a), and calculating the FWHM of the averaged profile. The smallest achievable FWHM of such lines was typically in the range of 30 nm to 35 nm, including the sputtered gold layer of nominally 5 nm. In the depicted case, a FWHM of 31.2 nm was achieved, as shown in the plot of line profile (Figure 5.15 b)). In panel c), the dependency of the linewidth on the depletion power P_{depl} is plotted. The FWHM approximately scales with the inverse square root of the depletion power as expected for a STED-like process (see Equation 2.14), until the regime of disconnected lines is reached. At the employed excitation
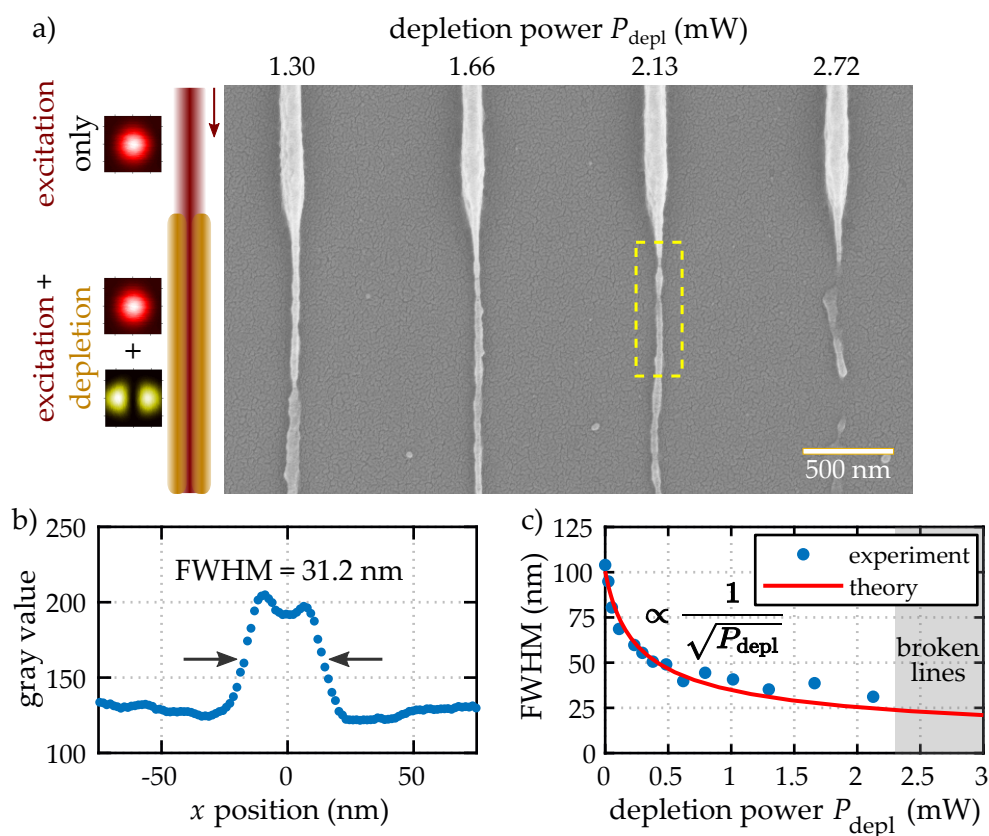
Figure 5.15: a) Scanning electron micrograph of a typical set of lines written at an excitation power of 0.69 mW, where the depletion laser is switched on for the lower part of each line. At depletion laser powers above 2.13 mW, the lines become unstable and disconnected. b) The averaged line profile extracted in the area marked by the dashed yellow line reveals a FWHM of 31.2 nm. c) As expected in theory, the achieved FWHM of lines is proportional to the inverse square root of the depletion laser power. Adapted from [139].

laser power, which is 50 % above the writing threshold, the FWHM of a line without depletion is 104 nm. The depletion laser led to a linewidth reduction of 70 %. For comparison, the thinnest lines that could be fabricated using only the excitation laser at powers very close to the writing threshold have a FWHM of around 55 nm. However, employing the depletion laser at such low excitation powers directly led to discontinuous lines without leaving a

excitation only   excitation + depletion

42 nm   51 nm

30 nm

300 nm
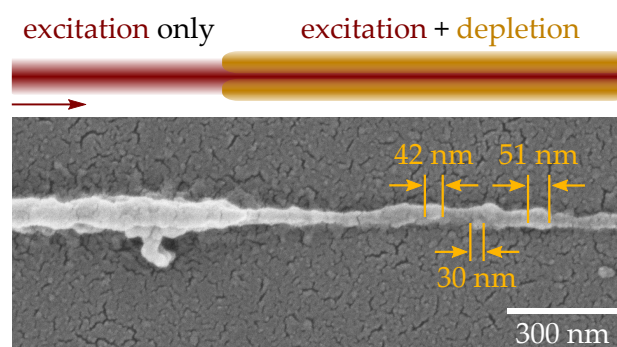
Figure 5.16: Close-up SEM image of a line where the depletion laser was switched on for the right part. The line features small grains with approximate sizes between 30 nm and 50 nm. Adapted from [139].

working window for depletion. Compared to these thinnest lines, the use of depletion led to an linewidth enhancement of almost a factor of 2. For comparison, the best value reported in literature for STED-inspired DLW was a FWHM of 34 nm, achieved by the Klar group using an acrylate resist with DETC as photoinitiator [111].

A further reduction of linewidth was limited by the decreasing stability of thin lines, which, at some point, were not stable enough anymore to withstand the development process leading to collapsing and breakup. Another issue that became apparent at such small linewidths is the inherent graininess of the photoresist. As shown in the close-up SEM image in Figure 5.16, the lines exhibited formation of small grains with diameters on the order of 30–40 nm, *i. e.*, on the same scale as the smallest linewidths observed. This defines an inherent minimum length scale for the achievable linewidths. Possibly, the formation of these microscopic grains is connected to the highly ordered stacking processes of the MC moieties. In literature, formation of microcrystallites on very similar scales was reported for zipper polymerization of SP-functionalized methacrylate copolymers [216].

Assessing the Achievable Resolution

In order to determine the resolution achievable using the STP photoresist, line grating patterns were fabricated with varying laser powers and grating period *a*. Following Equation 2.7, the theoretical diffraction limit for a wave-

length of 820 nm and a numerical aperture of 1.4 is 207 nm. SEM images of a typical set of gratings are depicted in Figure 5.17. Gratings with periods above the diffraction limit could be easily fabricated, as shown in panel a) for $a = 400$ nm. However, the gratings show smaller deteriorations as the individual lines exhibit the graininess mentioned above. In addition, larger flakes with sizes in the range of hundreds of nanometers attached to the lines, potentially having the same origin as the smaller grains. By using only the excitation laser, it was not possible to resolve grating periods below the diffraction limit (*e.g.* 175 nm, panel b)), even when setting the laser power close to the writing threshold. Instead of separated lines, a single block was obtained. When the depletion laser modulated by the phase mask was switched on in addition to the excitation laser, the lines could be resolved again (panel c)). However, it is evident that the quality of the gratings tremendously suffered. Neighboring lines touch each other at numerous positions, either by formation of microbridges or by pattern collapse. Both phenomena are common to high-resolution negative-tone photoresists [178–181] and appeared as well in our experiments on photoenol-based photoresists (see Section 4.3.3). These two photoresist systems are conceptually very similar. Therefore, we draw the same conclusion herein and attribute the formation of these defects to swelling effects occurring during the development process (panel d)). When immersed, toluene swelled both the unused resist and the cross-linked structures. Thereby, the cross-linked networks strongly increased in volume, leading to neighboring lines touching each other. Thereby, some of the MC aggregates were extended by SP and MC forms provided by the neighboring networks. When deswelling of the structures took place in isopropyl alcohol (and even more when drying with nitrogen), some of these connections remained in the form of microbridges. In other parts, the tension during deswelling led to a collapse of neighboring lines, bridging the gap in between.

A direct observation of the swelling behavior of the structures during development proved to be challenging because the contrast in refractive index between cross-linked structures and photoresist was very low. Instead, we performed a study monitoring changes of already developed structures. Figure 5.18 a) shows a grayscale light microscope image of a set of grating structures with periods in the range of 0.7–1.2 µm, *i.e.*, considerably above
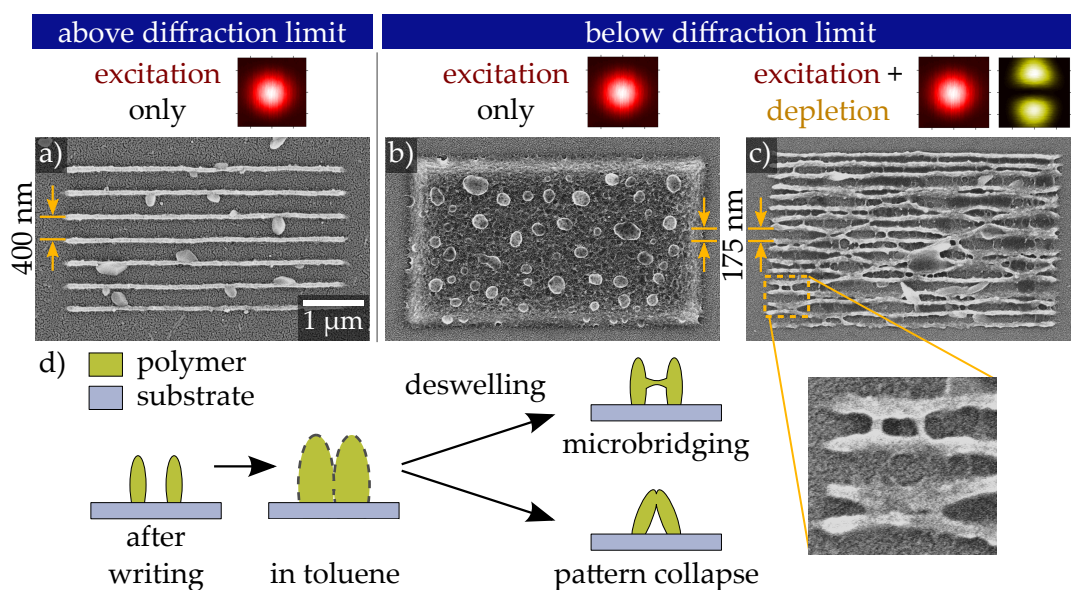
Figure 5.17: SEM images of different attempts to write grating structures. a) Gratings written with lattice constants above the diffraction limit of 207 nm feature clearly separated lines. b) At lattice constants below the diffraction limit, fabrication using only the excitation laser yields a solid block. If the depletion laser is used in addition, the lines can be resolved again, but suffer from microbridging and pattern collapse. Adapted from [139].

the diffraction limit in order to allow monitoring by regular light microscopy. The sample was developed by immersion in toluene and isopropyl alcohol and in a dry state at the time of imaging. After taking the picture, the sample was immersed into DMF, which is a good solvent for the copolymers. After 1 min, the sample was transferred into isopropyl alcohol and dried in a stream of nitrogen. The corresponding image (panel b)) shows pronounced deteriorations of the gratings caused by the strong swelling with DMF. The formation of microbridges cannot be observed unambiguously. However, is is evident that the formerly very straight lines now exhibit a rather wiggly shape and have collapsed in some places.

These effects may be reduced by using shorter copolymer chains with a smaller molecular weight, thereby increasing the degree of cross-linking (see discussion above). Another factor which influences the formation of such defects is the choice of solvents used for development. Therefore, the reso-
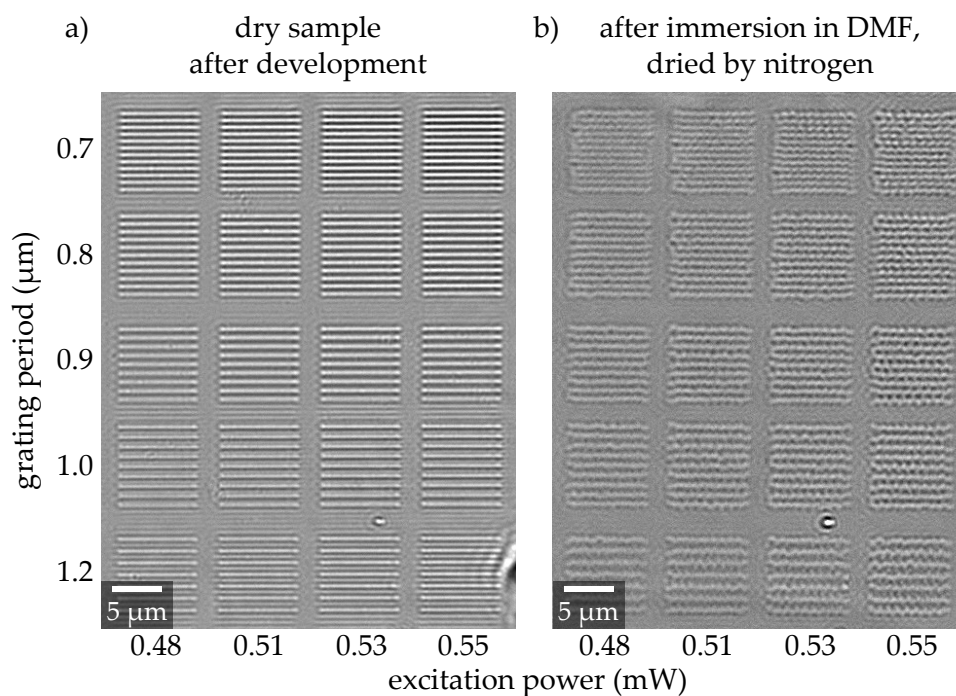
Figure 5.18: a) Grayscale light microscope image of a set of line gratings after regular development in toluene and isopropyl alcohol. After immersion in DMF, followed by isopropyl alcohol and drying in a stream of nitrogen, the structures show wiggles and deteriorations caused by swelling. Adapted from [139].

lution of the copolymers listed in Table 5.3 as well as several combinations of solvents were assessed. However, the using a photoresist based on **STP-1** and the development in toluene/isopropyl alcohol yielded the best results. As an alternative approach, we also explored writing in spin-coated thin films of the STP copolymers with regard to achieving higher cross-linking densities than in solution. Here, writing was possible as well but no considerable depletion effect could be observed (not depicted). Presumably, the conversion of MC forms to STP forms was sterically hindered [223]. In addition, swelling-induced damage was more severe than for liquid photoresists. Thus, the described issues faced when writing grating structures could not be avoided completely, rendering the high-resolution performance of the photoresist poorer compared to typical acrylate photoresists based on free-radical polymerization [6]. For comparison, using an acrylate photoresist

with the photoinitiator DETC, the Klar group achieved a lateral resolution of 120 nm by STED-inspired DLW [111]. Nevertheless, the depletion effect is present and our experiments show clear indications of sub-diffraction resolution.

Final Remarks on Lithography Using Spirothiopyran

In conclusion, the spirothiopyran chromophore proved to be suitable for applications in laser lithography. The presented experiments demonstrated that the thiol-Michael addition of STP to maleimide upon two-photon excitation can be employed for spatially resolved surface functionalization. However, transferring the photoswitching behavior of the chromophore found in solution, especially the light-induced transition from its MC to its STP form, proved to be challenging. The reason is that STP is very sensitive to the chemical environment, *e. g.*, polarity and steric freedom. For surface functionalization, no depletion effect could be observed. A more successful strategy was to employ copolymers bearing STP units as side groups for negative-tone photoresists enabling 3D structures. While the presented two-component resists exhibited a rather bad writing quality, a one-component photoresist which relies on cross-linking by supramolecular interactions showed considerably improved results. Using this photoresist, a reversible depletion effect was demonstrated that allowed linewidth reduction by a factor of 2, down to 31 nm. The resolution could be improved as well by using depletion, allowing fabrication of gratings just below the diffraction limit. However, the results were substantially impeded by defects such as formation of microbridges or collapse of lines which were presumably caused by swelling effects during development. Very similar issues occurred in the photoresist based on the photoenol system discussed in Section 4.3. In the next chapter, I will compare the two photoresist systems in more detail and discuss options for overcoming swelling-induced limitations.

6

Discussion

The two molecular photoswitches presented in this thesis have been described independently in their corresponding chapters. However, one finds many similarities and differences that are worth highlighting. In this last chapter of my thesis, I compare the two systems and describe their common limitations and prospective approaches to tackle those issues. Finally, I provide an outlook on possible new directions of research on diffraction-unlimited 3D laser lithography.

6.1 Comparison of Molecular Photoswitches

Both systems investigated in this thesis, photoenols generated from *ortho*-methylbenzaldehyde and spirothiopyrans, proved to constitute a molecular photoswitch suitable for STED-inspired laser lithography. It was possible to excite the chromophores by a nonlinear two-photon absorption process to induce formation of linkage between separate molecules. In case of the photoenol system, linkage could be suppressed by photoisomerization of long-lived (*Z*)-enols into short-lived (*E*)-enols, depleting the population of reactive species. In case of STP, the population of reactive MC forms was depleted by photoisomerization of MC back into STP. Thus, a pronounced depletion effect could be found in both systems that allowed for writing inhibition, linewidth enhancement and resolution improvement, in some cases beyond the diffraction limit.

Useful depletion laser powers were in the range of 1–10 mW. This is about one order of magnitude below typical depletion powers employed

in STED-inspired 3D laser lithography using stimulated-emission depletion or excited-state absorption (see Section 2.3). In photoinhibitor lithography, on the other hand, depletion powers in the microwatt range are used. Unfortunately, parasitic writing limited the usable depletion power range for both photoenol and STP. As mentioned in the corresponding sections, these effects could be related to residual absorption at the depletion wavelengths. As another origin of unwanted effects, one has to consider that a single chromophore that is simultaneously exposed to both excitation and depletion beam presumably undergoes many cycles between its two states during typical exposure times of $\geq 1\,\mathrm{ms}$ per voxel[1]. Each activation or deactivation involves an absorption process and the absorbed energy has to be dissipated by non-radiative transitions as the electrons and molecules rearrange. Thus, photodegradation processes could occur, leading to loss of a portion of the molecules. Such effects, commonly referred to as photo- or switching fatigue, are well-known in the field of photochromic species [188] and pose a limitation in STED-inspired microscopy [80]. Switching fatigue could partly explain irreversible depletion effects as described in Section 4.2.1. In this regard, stimulated-emission depletion has an advantage over other depletion mechanisms as no additional heat is injected into the material [6].

Comparing between the two investigated systems, the STP chromophore showed to be more sensitive to influences of its chemical environment. It was not possible to achieve a depletion effect in surface functionalization experiments where the chromophore was fixed on the substrate, presumably due to steric hindrance of the transition from the MC to the STP form. In contrast, for the photoenol system, the very same approach allowed to characterize the depletion mechanism in both qualitative and quantitative ways. Furthermore, sub-diffraction feature size down to a FHWM of 60 nm and sub-diffraction resolution of around 100 nm could be demonstrated. Therefore, the surface functionalization approach presented herein can provide deep insights for screening of prospective molecular photoswitches. As the photoswitching and the polymerization are separated, the behavior of the chromophore can be studied very precisely. However, it should always be accompanied by complementary studies because the results cannot necessarily be transferred

---

[1] Assuming a voxel size of $d = 100\,\mathrm{nm}$ and a maximum speed of $v = 100\,\mathrm{\mu m\,s^{-1}}$ yields an exposure time per voxel of $d/v = 1\,\mathrm{ms}$.

to 3D photoresists as seen in the case of STP.

Negative-tone 3D photoresists could be obtained by synthesizing methacrylate copolymers that bear the appropriate chromophores as side groups. In case of *o*-MBA, cross-link formation proceeds *via* dimerization of intermediate-state (Z)-enols which form covalent bonds. For STP, linkage between different copolymers was achieved by supramolecular interactions induced by the open MC form. Although the bonds were non-covalent, stable networks supporting 3D structures could be achieved. In direct comparison, however, the photoenol 3D resist exhibited a better writing performance and allowed fabrication of more complex 3D structures than the STP-based resist. Figure 6.1 a) and b) show a comparison of a nominally identical 3D structure. The structure written using the STP-based resist collapsed as the photoresist softened during development and exhibits small grains agglomerating onto the structure. By employing the depletion beams at the corresponding wavelengths, linewidth enhancement could be achieved in both systems. Here, the thinnest lines had a FWHM of 51 nm (photoenol) and 31 nm (STP). The latter result is competitive to state-of-the-art STED lithography [111]. The lines fabricated using the STP-based photoresist exhibited a grainy structure with grain sizes on the range of 30–50 nm, while the lines achieved using the photoenol resist were more smooth but formed wiggles due to detachment from the substrate (Figure 6.1 c) and d)).

In order to assess the achievable resolution, line grating structures were fabricated. For both photoresists, resolvable grating periods could be considerably reduced by employing depletion. For the STP-based photoresist it was possible to achieve slightly sub-diffraction resolution of 175 nm, while the photoenol-based resist allowed to resolve grating periods just at the diffraction limit or slightly above. Note that the diffraction limits for both systems differ because of the different excitation wavelengths. From Equation 2.7, the critical distances are found to 177 nm (photoenol) and 207 nm (STP). Both materials showed very similar limitations (Figure 6.1 e) and f)). Numerous microbridges were formed between neighboring lines and lines collapsed onto each other at several positions. Presumably, these effects can be traced back to swelling of the structures during development (see also Figures 4.26 and 5.17). Similar effects can be found in many different negative-tone resists across different lithography techniques [178–181]. Unfortunately, ap-
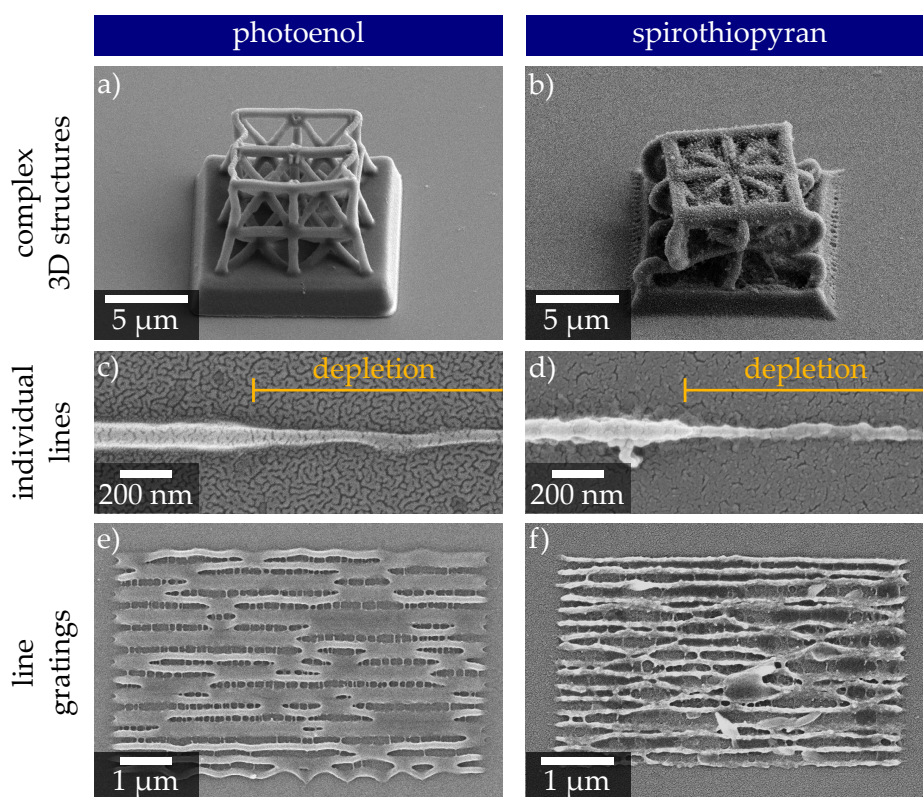
Figure 6.1: Comparison of SEM images of structures fabricated using the photoenol-based photoresist and the spirothiopyran-based photoresist. a) and b) Complex 3D lattice structures. c) and d) Individual lines where the respective depletion lasers were switched on for the right part. e) and f) Line gratings exhibiting numerous sites of microbridges and pattern collapses.

proaches reported in literature to overcome these limitations, *e. g.*, adapting solvents for development, did not provide remedy in our case. Standard DLW photoresists based on free-radical polymerization of acrylates show a better writing performance in that regard, presumably due to a higher degree of cross-linking achieved in the polymer network. Therefore, different copolymer compositions were explored for both STP and photoenol in order to increase the cross-linking density in the written structures. However, the issues remained (see Sections 4.3.1 and 5.4.2).

One part of the composition that was kept equal for all copolymers in

these studies is the choice of methacrylate as the backbone of the copolymers. This choice was made based on feasibility of synthesis and on the fact that methacrylate copolymers are widely used in lithographic applications, even in high-resolution electron beam lithography [173, 174, 227]. However, these materials are usually applied as spin-coated solid resist films and not as liquid solutions as herein. Previous liquid DLW photoresists based on methacrylate copolymers exhibited similar issues of graininess and strong shrinkage [136]. Therefore, future studies should involve different copolymer backbones such as acrylate or styrene. Generally, copolymer-based photoresists have achieved a high level of maturity and success in industrial planar microlithography and possibly many insights on molecular design of photoresists can be transferred to photoresists for STED-inspired 3D laser lithography [174, 227]. A different route is going to small multifunctional molecules instead of copolymer chains. Standard DLW photoresists often consist of rather small tri- or tetrafunctional acrylate monomers such as pentaerythritol triacrylate or multifunctional epoxy monomers (SU-8). Here, some studies performed for e-beam lithography indicate that going to smaller molecules can lead to improved resolution [175].

6.2 Is the Minimum at Zero?

Apart from chemical limitations, the question remains whether the achievable resolution and in particular the minimum feature size might be limited by optics as well. For example, in surface functionalization experiments using the photoenol system, the experimental data on linewidth and resolution were numerically reproduced by adopting a rate equation model (see Section 4.2). Thereby, it was necessary to assume that the minimum of the depletion laser focus was not a perfect zero but there was some finite residual intensity on the order of 1–2 % of the peak intensity. This value was extracted from laser focus measurements by using the technique of scanning gold beads described in Section 3.2.1. However, noise levels in the measurement were on a similar level. Therefore, it is not clear whether the assumed values are correct.

A different example is shown in Figure 6.2. The figure depicts a SEM image of a set of test patterns written using a STP-based photoresist (copolymer

STP-2, 40 wt% in acetophenone) with a fixed excitation laser power. In the central part of each line, the depletion laser modulated by the half-space phase mask was switched on. The depletion laser power increases line to line from left to right. In the left part, the depletion effect leads to decreasing linewidth until at some point the lines become discontinuous and eventually completely disappear. Only at even higher depletion laser powers, in the right part of the image, double line features appear due to parasitic writing effects by the two intensity maxima of the depletion laser.

One possible interpretation is that there was some finite residual intensity in the minimum such that the depletion beam inhibits writing not only at the edges of a line but also in its center. On the other hand, assuming a near-perfect depletion focus, one could argue that there is a minimum linewidth inherent to the photoresist below which the resulting line is not stable enough to withstand the development procedure. The reason is that during development, the solvent strongly swells the structures. Removing the solvent induces tensions that destroys thin fragile lines. Both explanations are reasonable and in fact both effects might contribute to the experimental results.

Thus, one would like to reduce the residual intensity as much as possible. Theoretically, the half-space phase mask leads to a plane of (perfectly) zero intensity in the center of the focus that is even robust against some types of possible misalignments (see Section 3.2.2). In practice, however, the laser beam is directed and reshaped by several other optical elements before and after passing through the phase mask. While all optics were carefully selected, it cannot be ruled out that wavefront errors are introduced, given the collimated laser beam covers an area of several square millimeters.[2]

Therefore, one can only resort to measuring the residual intensity. Within the master thesis of Tobias Messer which was supervised by me, the use of a highly sensitive photon-counting APD was assessed for focus measurements. Using gold beads as scattering particles and confocal detection, the residual intensity in a laser focus generated by a half-space phase mask could be distinguished from the optical and electronic background. Thus, it was

---

[2] If the aberrations were known, they could be compensated for by manipulating the wavefront using a spatial light modulator based on electronically configurable liquid crystals [15].
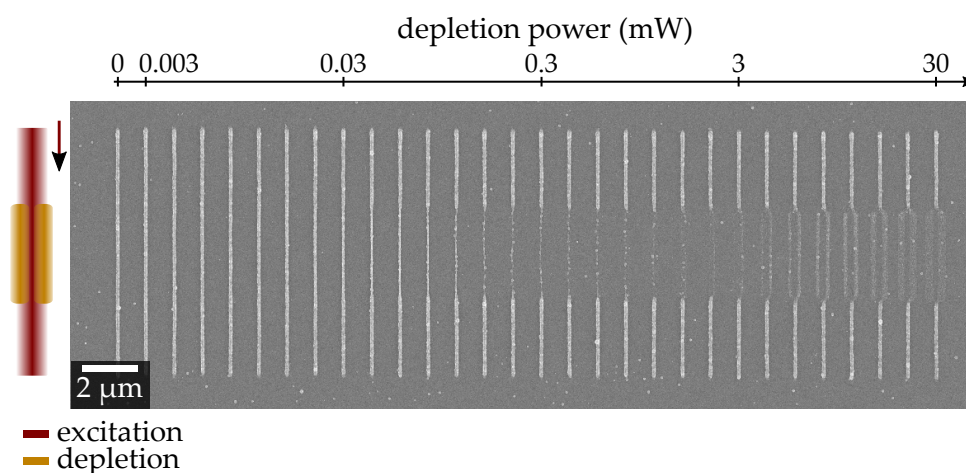
Figure 6.2: SEM image of a series of lines written using copolymer **STP-2** at 40 wt% in acetophenone. The depletion laser was switched on for the central part of each line. Lines become thinner with increasing depletion power and eventually disappear. At high depletion power, parasitic writing by the depletion laser occurs.

possible to quantify the residual intensity in the minimum. However, a careful investigation of the contributions to the background was necessary. Moreover, the alignment procedure necessary to achieve a reliable measurement proved to be too cumbersome for routine operation on a daily basis. Small drifts in the alignment led to strong deviations of the measured focus shape. Therefore, the scheme was not transferred to the regular lithography setup. Still, confocal detection could be used as a "magnifying glass" for the minimum in the laser focus. Instead of gold beads, fluorescent beads or quantum dots were assessed as well. Here, the fluorescence signal can be spectrally separated from the optical background. However, for adjustment of a two-wavelength STED lithography setup, it is necessary to measure both laser foci at the same time. This is not feasible using a single fluorescent particle due to different spectral sensitivities or fluorescence overlapping with one of the wavelengths. Thus, further improvements are necessary in order to be able to quantify the residual intensity in a practicable way.

6.3 NEW DIRECTIONS FOR STED-INSPIRED LITHOGRAPHY

In this final part of my thesis, I discuss a few possible future directions for STED-inspired lithography and beyond. Some of these ideas have already been published as part of a review article [56].

Photoacid Generators

The development of a photoacid generator (PAG) that constitutes a molecular photoswitch, *i.e.*, offers the possibility to evade acid formation by exposure to a second wavelength of light, could open up a wide field of innovations.

Highly developed chemically amplified negative-tone photoresists that are used in industrial microlithography would become accessible for STED-inspired lithography by exchanging the standard PAGs contained in those resists with a potentially STED-capable PAG [227]. An example is the widely used epoxy photoresist SU-8 (Microchem) that relies on cationic polymerization initiated by photogenerated acids. The photoacids act as catalysts of the cross-linking reaction. Therefore, cross-linked networks are generated efficiently. While SU-8 itself does not support highest resolutions, a series of similar multifunctional epoxy monomers could potentially support resolutions in the sub-50 nm range [175].

Moreover, the semiconductor industry has largely moved from negative-tone to positive-tone photoresists for high-resolution patterning due to issues related to swelling-induced damage of the exposed structures during development, very similar to the issues encountered in the work of this thesis (see above) [174]. Chemically amplified positive-tone photoresists usually rely on light-induced polarity changes mediated by photogenerated acids and can be developed in aqueous developer solutions. Therefore, they are conceptually less prone to swelling-related deteriorations.

Recently, the semiconductor industry has put tremendous efforts into establishing extreme-UV lithography in order to achieve higher resolutions by decreasing the exposure wavelength to 13.5 nm. However, at such extreme wavelengths, development of photoresist materials is a challenging task, especially since post-processing usually involves etching steps. Here, adopting a STED-inspired exposure scheme for planar lithography could

146

provide a promising avenue. Potentially, one could stay in the optical wavelength regime where well-established photoresist materials are available and increase the resolution by exploiting depletion effects [228].

Therefore, screening experiments on two interesting PAGs were performed in the course of this thesis. These experiments and their results are described in Section A.2. For one investigated PAG, acid release proceeds *via* photoenolization and could therefore be potentially suppressed by photoisomerization of intermediate photoenols, similar to the *o*-MBA chromophore studied in Chapter 4. The second investigated PAG is a photochromic species, where acid formation proceeds *via* a one of the two isomeric forms of the species, similar to spirothiopyran chromophore described in Chapter 5. Unfortunately, writing inhibition by the depletion laser could not be observed in these preliminary screening experiments. Nevertheless, the development of PAGs suitable for STED-inspired lithography is highly desirable.

A Forgetting Photoresist

As described in Section 2.1.2, photoresists used in DLW usually accumulate consecutive exposures, *i.e.*, possess a "memory". This includes exposure doses below the writing threshold and has a considerable impact on the attainable resolution according to Sparrow's criterion, as shown in Section 2.1.3. In planar mask lithography, this aspect is not as important because the whole sample is exposed simultaneously. In DLW, however, exposures of individual parts are separated in time. Therefore, a photoresist that locally "forgets" previous sub-threshold exposures (before the laser focus comes close again) would allow to sequentially write two lines with arbitrarily small spacing. The resolution would not be limited by optical diffraction and proximity effects would be evaded completely [67, 69, 104].

In literature, one can find a few approaches towards erasing the memory of the photoresist. By adding quencher molecules into the resist, the size of the voxel was reduced as the polymerization reaction was terminated faster and radical diffusion out of the focal volume was suppressed [229, 230]. The concept is similar to photoinhibitor lithography described in Section 2.3.3 but only requires a single laser beam as the quenchers are permanently active. The issue of irreversible consumption of the quencher molecules was addressed by Sakellari *et al.* [231]. Here, writing was performed at very

low scan speeds using a hybrid organic-inorganic photoresist that contains highly mobile quenchers. In this way, quencher molecules could diffuse into the scanned volume as the quenchers were consumed, keeping the quencher concentration nearly constant. Despite the slow scan speed, improved resolution was demonstrated by fabrication of woodpile photonic crystals and, more recently, 3D plasmonic metamaterials [231, 232]. A different approach used a novel cationic PAG that upon two-photon excitation cleaves into two fragments which can initiate cationic polymerization of epoxy photoresists. After around 20 μs, the fragments recombine, reforming the initial PAG. Although a moderate resolution increase was achieved, it remains unclear whether sub-diffraction resolution is truly in reach with this approach.

These approaches could not yet break the diffraction limit and further research is required. Nevertheless, a forgetting photoresist would provide an interesting avenue for lithography.

7 Chapter 7
CONCLUSION

In this thesis, I have investigated two photoswitchable materials that can be employed as molecular photoswitches for STED-inspired laser lithography. For both materials, the application for spatially resolved, potentially sub-diffraction surface functionalization has been assessed and negative-tone photoresists based on methacrylate copolymers have been described and characterized with regard to attaining an enhancement of feature size or resolution by using depletion.

As described in Section 2.2.2, a photoswitch material needs to exhibit an effective behavior as depicted again in Figure 7.1 a). Switching from an unreactive state A into a reactive state B is induced by absorption of light at the excitation wavelength. The reverse switching from B to A takes place upon absorption of light at the depletion wavelength. After a certain lifetime, state B undergoes an irreversible reaction into state C which represents the reaction product. For a potential application in 3D laser lithography, the transition corresponding to the excitation laser needs to follow a nonlinear, multi-photon process in order to allow for fabrication of 3D structures (see Section 2.1.2). In Section 2.3, I have reviewed previously reported materials utilized as molecular photoswitches for STED-inspired lithography.

In Chapter 3, I have described the employed lithography setup that was operated at different laser wavelengths depending on the investigated chromophores. Moreover, fabrication and alignment of the half-space phase masks used for generating the special depletion foci have been presented. The employed foci featured a plane of zero intensity in the center and allowed for confinement of the cross-linking reaction along one lateral direction. In principle, a translation of the results to other depletion foci is

a)

b)

c)
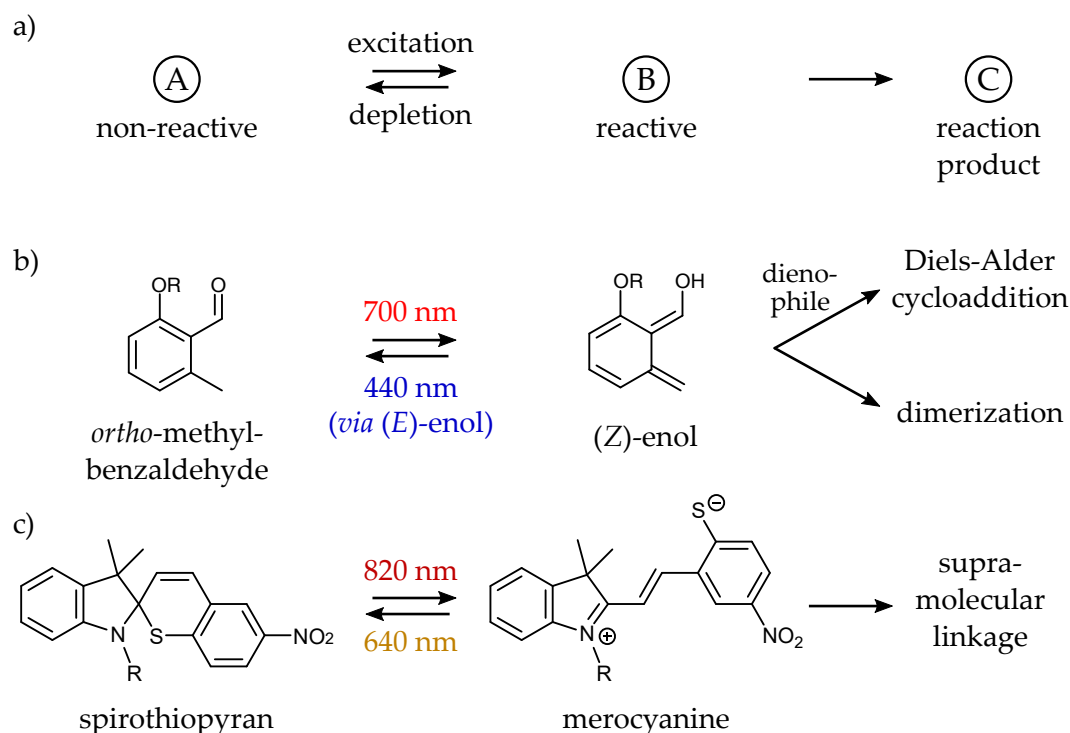
Figure 7.1: Schemes of a) the ideal molecular photoswitch as presented in Section 2.2.2, b) the photoenol molecular photoswitch described in Chapter 4, and c) the spirothiopyran molecular photoswitch investigated in Chapter 5.

possible. Moreover, I have shown the general workflows of sample processing and characterization used for 2D surface functionalization and 3D laser lithography.

In Chapter 4, the molecular photoswitch based on intermediate-state photoenols generated from *ortho*-methylbenzaldehydes has been described. It is again schematically depicted in Figure 7.1 b). Upon two-photon excitation of *ortho*-methylbenzaldehydes at 700 nm, reactive intermediate-state (*E*)- and (*Z*)-enols are generated that differ in lifetime. The short-lived (*E*)-enol rapidly converts back into *ortho*-methylbenzaldehyde by reketonization, while the (*Z*)-enol is more stable with lifetimes on the microsecond scale and can therefore participate in further reactions with different molecules. By simultaneous exposure to the depletion laser light at 440 nm, (*Z*)-enol undergoes photoisomerization into (*E*)-enol which rapidly reketonizes, effectively de-

pleting the population of (Z)-enols. In experiments on surface functionalization, a bromine-carrying maleimide species was utilized as a reaction partner, leading to spatially resolved functionalization of the surface with bromine groups. Here, the use of depletion allowed to confine the functionalized areas, achieving sub-diffraction resolution and feature sizes. By growing polymer brushes from the bromine groups, the functionalization was rendered measurable for AFM. Moreover, I have presented negative-tone photoresists based on methacrylate copolymers bearing *ortho*-methylbenzaldehyde moieties on the side chain. Here, cross-link formation proceeded *via* dimerization of (Z)-enols. Using these photoresists, complex 3D structures were fabricated. Employing depletion led to enhanced feature sizes but issues related to swelling of the cross-linked networks prevented attaining sub-diffraction resolution. Grating structures suffered from formation of microbridges and pattern collapse. Nevertheless, the photoenol system has proved to be an efficient photoswitch for STED-inspired lithography.

In Chapter 5, spirothiopyran has been introduced as a chromophore exhibiting a molecular photoswitching behavior (see Figure 7.1 c)). Belonging to the family of photochromic compounds, spirothiopyran possesses two isomeric forms, ring-closed spirothiopyran and ring-opened merocyanine which is formed upon two-photon excitation at 820 nm. The merocyanine form features a thiolate anion which can potentially undergo thiol-Michael addition with activated dienophiles and moreover is a zwitterionic species. Upon absorption of the depletion laser light at 640 nm, the unreactive spirothiopyran is reformed. In surface functionalization experiments, excitation proved to be efficient but no depletion effect could be observed, presumably due to steric hindrance of the merocyanine forms by the chemical environment. In order to obtain a negative-tone photoresist, methacrylate copolymers bearing spirothiopyran moieties on the side chain were employed. A photoresist composition was identified where cross-linking proceeded *via* non-covalent supramolecular interactions. The photoresist was capable of supporting free-standing 3D structures. By employing the depletion laser, linewidth enhancement was achieved with FWHM linewidths on the order of 35 nm. Grating structures were deteriorated by swelling-induced defects but clear indications of sub-diffraction resolution were found.

Finally, I have compared the two investigated systems in Chapter 6 and

discussed their similarities and differences. Using methacrylate copolymers for obtaining negative-tone photoresists led to similar issues for both, photoenol and spirothiopyran. Potentially, these limitations can be overcome in the future by tailoring the copolymer backbone for high-resolution applications. Furthermore, I have pointed out two avenues which have not been intensively investigated yet and might contribute to achieving higher resolutions in STED-inspired lithography in the future: the development of photoswitchable acid generators and finding ways to eliminate the "memory" of photoresists.

The work presented in this thesis demonstrates that photoisomerization is a suitable mechanism for realizing molecular photoswitches for STED-inspired lithography. Further research towards a better understanding of the microscopic processes effecting the performance of the photoresists might lead to further improvements in the future. Moreover, chemistry still offers a plethora of unexplored materials some of which might prove to provide even more interesting properties. Therefore, I am confident that future research in this interdisciplinary field between physics and chemistry will ultimately make the diffraction limit a tale of the past.

A

APPENDIX

A.1 NUMERICAL METHOD FOR CALCULATING LASER FOCI

When focusing a laser beam with high numerical aperture, the intensity distribution in the focus deviates from the Gaussian distribution obtained in the paraxial approximation as the vectorial nature of the electromagnetic field has to be taken into account. Therefore, a numerical method is used in order to calculate the expected intensity distributions of laser foci in the experimental setup. The method was reported by van de Nes *et al.* [233] and is based on the diffraction theory as formulated by Richards and Wolf [234]. Figure A.1 shows a scheme of the calculation method. The wavefront of the electric field $\vec{E}_0(k_r, k_\Phi)$ with wavelength λ in the back focal plane Ω of the objective lens describes the incoming laser beam. Different phase mask patterns $\psi(k_r, k_\Phi)$ can easily be imposed by multiplication with a phase factor $\exp(-i\psi)$. The objective lens is described as a transformation operator M, mapping $\vec{E}_0$ onto $\vec{E}_1$ which is defined on a spherical shell Ω'. Note that by this rotating transformation, a purely transverse electrical field can generate longitudinal components as well. In order to propagate the electric field towards the focal point, the coordinates k_r and k_Φ are converted into lateral cartesian coordinates k_x and k_y and interpreted as lateral components of wave vectors $\vec{k} = (k_x, k_y, k_z)$ of plane waves originating from the curved surface of Ω' and interfering in the focal region. The electric field $\vec{E}(\vec{r})$ in the focus can then be determined by calculating the diffraction integral

$$\vec{E}(\vec{r}) = \frac{-iR}{2\pi} \iint\limits_{\Omega'} \frac{\vec{E}_1(k_x, k_y)}{\sqrt{k_z k}} \exp\left(i\vec{k}\vec{r}\right) dk_x dk_y \, , \tag{A.1}$$

153
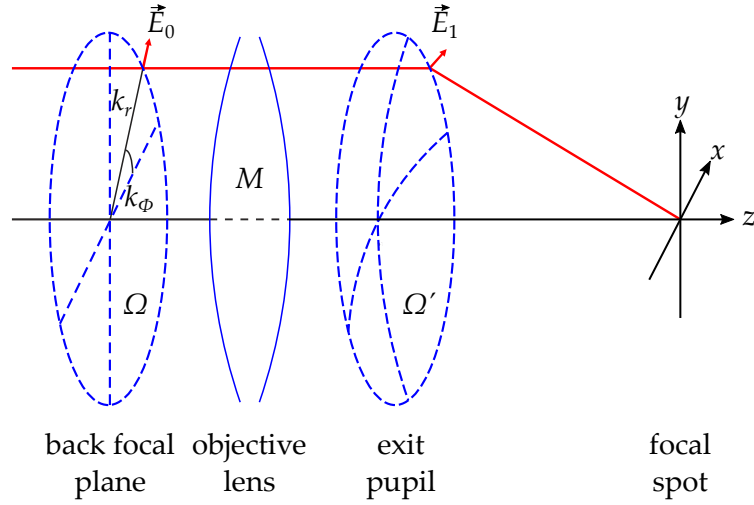
Figure A.1: Scheme of the focus calculation method. The incident electrical field E_0 is defined in the back focal plane. The objective lens is represented by a transformation M, creating the field E_1 defined on the curved surface Ω'. The intensity distribution is calculated in the vicinity of the focal spot. Adapted from [233] with permission.

where R is the distance between Ω' and the focal point, $k = |\vec{k}| = 2\pi n/\lambda$, n is the refractive index of the medium and $\vec{r} = (x, y, z)$ are cartesian coordinates at the focal point. Numerically, this integration can be performed by efficient fast Fourier transform algorithms. Additionally, the calculation method can be extended to layered media with different refractive indices [233]. The algorithm was implemented in Matlab by Joachim Fischer. Details on the implementation can be found in his PhD thesis [71].

A.2 EXPERIMENTS ON PHOTOACID GENERATORS

Apart from the main work presented in this thesis, two specific photoacid generators (PAGs) were investigated in lithography experiments. These PAGs are chemically related to the molecular photoswitches presented in the main part and were expected to provide a similar switching behavior that might be exploited for STED-inspired lithography. However, these experiments have a very preliminary character and should rather be considered screening

experiments than thorough investigations. In both experiments, no depletion effect, *i. e.,* writing inhibition could be observed.

A.2.1 PHOTOACID GENERATION FROM PHOTOENOL

In the work presented in Chapter 4, the chromophore ortho-methylbenzalde-hyde has been employed for generating intermediate-state photoenols. A very similar class of chemical compounds, ortho-alkylphenylketones, can act as a photoremovable protecting group [143]. Thereby, the light-induced deprotection proceeds *via* photoenolization. In fact, the inspiration for using photoenols for STED-inspired laser lithography originally came from reports studying the photorelease of HCl from ortho-alkylphenylketones [163]. Therefore, we investigated whether these species can be used as photoacid generators for DLW and, critically, whether a depletion effect by photoisomerization can be observed.

A suitable commercially available compound, 2-chloro-1-(2,5-dimethyl-phenyl)ethanone (PE-PAG) (Sigma Aldrich), bears a chlorine atom in the α-position and should be capable of releasing HCl. In preliminary experiments this expected photorelease was confirmed by dissolving a small amount of the compound in water. Upon exposure to UV light for 5 min, the pH value of the solution decreased from 7 down to 1, indicating an efficient acid release.

In order to assess the lithographic performance, a photoresist was prepared consisting of 39 mg of poly(hydroxystyrene) ($M_w = 11 \, \text{kg mol}^{-1}$, Sigma Aldrich), 10 mg of hexamethylolmelamine (TCI) as cross-linking agent, and 14 mg of PE-PAG, dissolved in a mixture of 300 μl propylene glycol methyl ether acetate and 100 μl γ-butyrolactone (Figure A.2 a)). This composition is expected to act as a negative-tone photoresist. The photoacid released by the PAG reacts with the melamine cross-linker that subsequently undergoes electrophilic substitution onto the electron-rich styrene ring [174]. As the melamine is tri-functional, it can cross-link between different poly(hydroxystyrene) chains, leading to network formation. The photoresist was spin-coated onto a plasma-activated glass substrate.

Using the same optical configuration as for the photoenol experiments (Figure 3.5), different patterns were written with the excitation laser tuned

a)

PE-PAG   poly(hydroxystyrene)   hexamethylolmelamine

b)

20 µm   20 µm
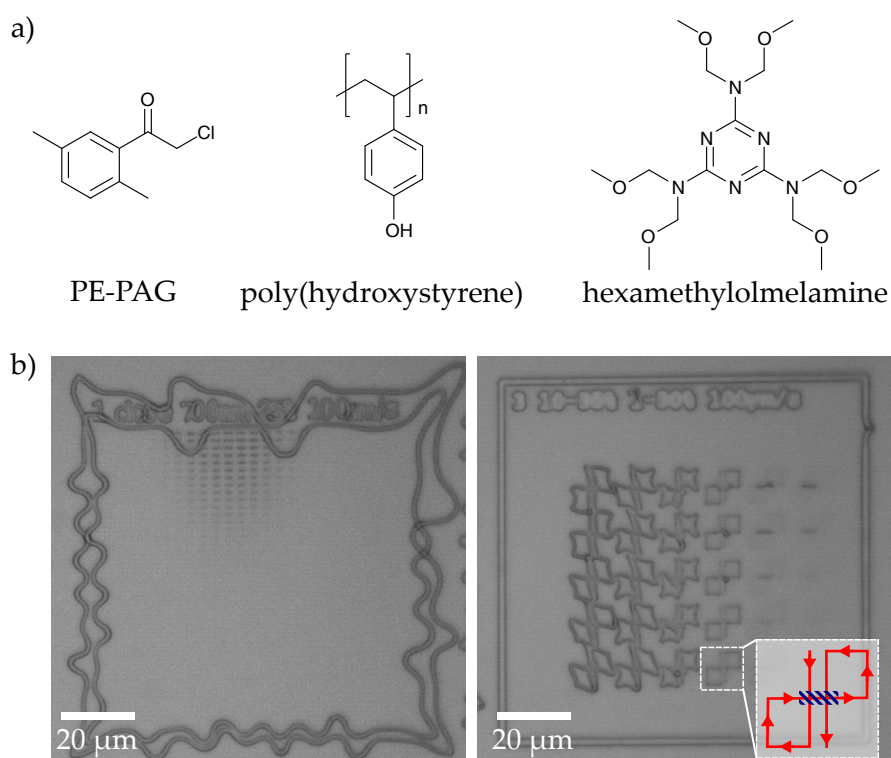
Figure A.2: a) Scheme of molecules included in the photoresist. b) Light micrographs of writing results indicate that no writing inhibition could be obtained by the depletion laser.

to 700 nm and the depletion laser at 440 nm. After writing, the samples were post-baked for 4 min at 125 °C as the cross-linking reaction needs to be thermally activated. Development was performed in an aqueous developer (ma-D 533S, micro resist technology). Light microscope images of the results are shown in Figure A.2 b). Clearly, writing by the femtosecond-pulsed excitation laser is possible, starting from excitation laser powers of about 7 mW, presumably by two-photon absorption. Some of the lines have detached from the glass surface during the development process. However, no writing inhibition by the depletion laser could be observed. Instead, parasitic writing by the depletion laser occurred at powers of about 0.3 mW, probably by one-photon absorption at the depletion wavelength. Employing a more red-shifted depletion laser at 532 nm (picosecond-pulsed) did not lead to an improvement.

Photoresist compositions containing epoxy materials, *e. g.*, poly(glycidyl methacrylate), were also assessed as many commercial photoresists (*e. g.* SU-8) rely on acid-catalyzed cationic polymerization of epoxy groups. However, no writing could be observed for these class of materials. Presumably, the generated photoacid HCl is not efficient for initiating cross-linking of epoxy groups. In literature, photorelease of carboxylic acids from different ortho-alkylphenylketone species has been reported which might provide more efficient initiation for epoxy resists [143].

A.2.2 Photochromic Photoacid Generators

Many commercial high-resolution photoresist formulations rely on onium salt PAGs that can release sulfonic acids upon UV exposure. Examples are epoxy-based negative-tone photoresists (such as SU-8) or chemically amplified positive-tone resists that are used as workhorse photoresists in industrial microelectronic fabrication [174]. Apart from spirothiopyran that was investigated in detail in this thesis, there are other classes of photochromic molecules that offer a similar optical switching mechanism (see Section 5.1.1). In the group of Prof. Kawai (NAIST, Japan), a family of compounds based on photochromic terarylene was developed that can release triflic acid upon UV exposure and could therefore be used as PAG in lithography applications [235, 236]. Very similar to spirothiopyran, the molecule possesses an open and a closed form. Upon UV irradiation, the open form converts into the closed form which features an absorption band in the visible and eventually leads to acid release. For spirothiopryan or the closely related photochromic diarylethenes, exposure to visible light leads to switching of the molecule back into the open form. Therefore, photoacid generation might be suppressed by visible light, offering a depletion channel that could possibly be used for STED-inspired lithography. In particular, such a mechanism could be easily transferred to commercial high-resolution resists by simply exchanging the PAG. To assess this potential application, a cooperation with the Kawai group was initiated. While they supplied the PAG material, I prepared the photoresist and performed lithography experiments.

A photoresist was prepared consisting of 0.5 mg of PAG (species PAGQ-CF$_3$ from [236]), 4.5 mg of poly(glycidyl methacrylate) (M_w = 10–20 kg mol^{-1},

a)

open form · closed form · acid release

b)

width:
131.6 nm

20 µm · 200 nm
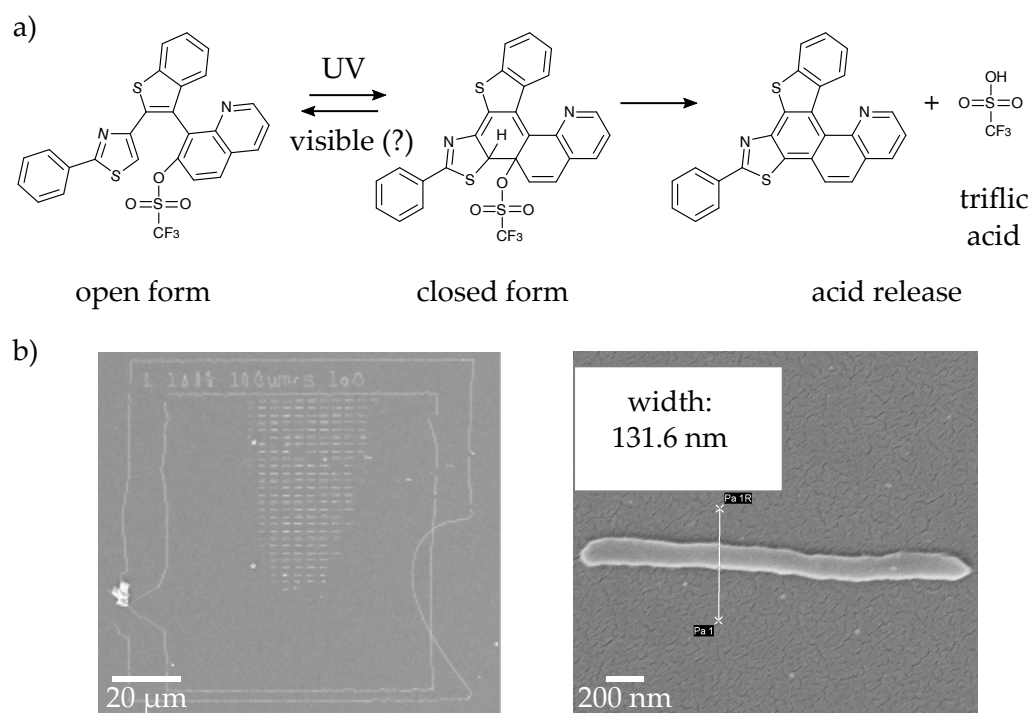
Figure A.3: a) Scheme of the expected photoswitching of the photochromic PAG leading to acid release (according to [236]). b) Electron micrographs of writing results indicate a minimum linewidth of 130 nm.

Sigma Aldrich), and 58 mg of anisole as a solvent (Figure A.3 a)). The epoxy groups of the glycidyl polymer are expected to cross-link with each other by cationic polymerization initiated by the triflic acid. The resist was spin-coated onto a plasma-activated cover glass and baked for 1 min at 60 °C. Then lithography experiments were performed using excitation at 700 nm and depletion at 532 nm (picosecond-pulsed). After writing, a post-exposure bake was performed for 1 min at 60 °C before developing in acetone and isopropyl alcohol. Figure A.3 b) shows SEM images of the results. Writing was possible for laser powers above 1.5 mW, presumably by two-photon absorption. Some parts of the lines detached from the substrate during development. The smallest linewidth observed using only the excitation laser was approximately 132 nm. However, using depletion did not lead to writing inhibition but only to parasitic writing (not depicted). Using other depletion wavelengths, 440 nm or 640 nm, did not lead to an improvement.

Bibliography

[1] G. E. Moore, "Cramming More Components onto Integrated Circuits", Electronics **38**, 114 (1965) (Cited on page 5).

[2] T. Baldacchini, ed., *Three-Dimensional Microfabrication Using Two-Photon Polymerization: Fundamentals, Technology, and Applications*, Micro and Nano Technologies (William Andrew Publishing, Oxford, 2016) (Cited on pages 6, 10).

[3] J. Stampfl, R. Liska, and A. Ovsianikov, eds., *Multiphoton Lithography: Techniques, Materials, and Applications* (Wiley-VCH, Weinheim, Germany, 2016) (Cited on pages 6, 10).

[4] E. Abbe, "Beiträge Zur Theorie Des Mikroskops Und Der Mikroskopischen Wahrnehmung: I. Die Construction von Mikroskopen Auf Grund Der Theorie", Arch. Für Mikrosk. Anat. **9**, 413–418 (1873) (Cited on pages 6, 20).

[5] S. W. Hell and J. Wichmann, "Breaking the Diffraction Resolution Limit by Stimulated Emission: Stimulated-Emission-Depletion Fluorescence Microscopy", Opt. Lett. **19**, 780–782 (1994) (Cited on pages 6, 25, 35).

[6] J. Fischer and M. Wegener, "Three-Dimensional Optical Laser Lithography Beyond the Diffraction Limit", Laser Photonics Rev. **7**, 22–44 (2013) (Cited on pages 6, 22, 30, 33, 35, 36, 39, 40, 137, 140).

[7] S. Maruo, O. Nakamura, and S. Kawata, "Three-Dimensional Microfabrication with Two-Photon-Absorbed Photopolymerization", Opt. Lett. **22**, 132–134 (1997) (Cited on page 10).

[8] S. Maruo and K. Ikuta, "Three-Dimensional Microfabrication by Use of Single-Photon-Absorbed Polymerization", Appl. Phys. Lett. **76**, 2656–2658 (2000) (Cited on pages 11, 18, 96).

[9] M. Thiel, H. Fischer, G. von Freymann, and M. Wegener, "Three-Dimensional Chiral Photonic Superlattices", Opt. Lett. **35**, 166–168 (2010) (Cited on pages 11, 18, 24).

[10] M. Malinauskas, P. Danilevicius, and S. Juodkazis, "Three-Dimensional Micro-/Nano-Structuring Via Direct Write Polymerization with Picosecond Laser Pulses", Opt. Express **19**, 5602–5610 (2011) (Cited on page 11).

[11] M. T. Do, T. T. N. Nguyen, Q. Li, H. Benisty, I. Ledoux-Rak, and N. D. Lai, "Submicrometer 3D Structures Fabrication Enabled by One-Photon Absorption Direct Laser Writing", Opt. Express **21**, 20964–20973 (2013) (Cited on pages 11, 18, 96).

[12] P. Mueller, M. Thiel, and M. Wegener, "3D Direct Laser Writing Using a 405 Nm Diode Laser", Opt. Lett. **39**, 6847–6850 (2014) (Cited on pages 11, 18, 24, 94, 96).

[13] E. Stankevičius, E. Daugnoraitė, A. Selskis, S. Juodkazis, and G. Račiukaitis, "Photo-Polymerization Differences by Using Nanosecond and Picosecond Laser Pulses", Opt. Express **25**, 4819–4830 (2017) (Cited on page 11).

[14] T. Bückmann, N. Stenger, M. Kadic, J. Kaschke, A. Frölich, T. Kennerknecht, C. Eberl, M. Thiel, and M. Wegener, "Tailored 3D Mechanical Metamaterials Made by Dip-in Direct-Laser-Writing Optical Lithography", Adv. Mater. **24**, 2710–2714 (2012) (Cited on pages 11, 13).

[15] J. K. Hohmann, M. Renner, E. H. Waller, and G. von Freymann, "Three-Dimensional μ-Printing: An Enabling Technology", Adv. Opt. Mater. **3**, 1488–1507 (2015) (Cited on pages 11, 19, 24, 144).

[16] J.-I. Kato, N. Takeyasu, Y. Adachi, H.-B. Sun, and S. Kawata, "Multiple-Spot Parallel Processing for Laser Micronanofabrication", Appl. Phys. Lett. **86**, 044102 (2005) (Cited on page 11).

[17] L. Yang, A. El-Tamer, U. Hinze, J. Li, Y. Hu, W. Huang, J. Chu, and B. N. Chichkov, "Parallel Direct Laser Writing of Micro-Optical and Photonic Structures Using Spatial Light Modulator", Opt. Lasers Eng. **70**, 26–32 (2015) (Cited on page 11).

[18] M. Malinauskas, A. Žukauskas, S. Hasegawa, Y. Hayasaki, V. Mizeikis, R. Buividas, and S. Juodkazis, "Ultrafast Laser Processing of Materials: From Science to Industry", Light-Sci. Appl. **5**, e16133 (2016) (Cited on page 11).

[19] K. J. Schafer, J. M. Hales, M. Balu, K. D. Belfield, E. W. Van Stryland, and D. J. Hagan, "Two-Photon Absorption Cross-Sections of Common Photoinitiators", J. Photochem. Photobiol. Chem. **162**, 497–502 (2004) (Cited on pages 12, 63).

[20] Z. Li, N. Pucher, K. Cicha, J. Torgersen, S. C. Ligon, A. Ajami, W. Husinsky, A. Rosspeintner, E. Vauthey, S. Naumov, T. Scherzer, J. Stampfl, and R. Liska, "A Straightforward Synthesis and Structure–Activity Relationship of Highly Efficient Initiators for Two-Photon Polymerization", Macromolecules **46**, 352–361 (2013) (Cited on page 12).

[21] R. Nazir, E. Balčiunas, D. Buczyńska, F. Bourquard, D. Kowalska, D. Gray, S. Maćkowski, M. Farsari, and D. T. Gryko, "Donor–Acceptor Type Thioxanthones: Synthesis, Optical Properties, and Two-Photon Induced Polymerization", Macromolecules **48**, 2466–2472 (2015) (Cited on page 12).

[22] M.-L. Zheng and X.-M. Duan, "Photoinitiators for Multiphoton Absorption Lithography", in *Multiphoton Lithography*, edited by J. Stampfl, R. Liska, and A. Ovsianikov (Wiley-VCH, Weinheim, Germany, 2016), pp. 133–165 (Cited on page 12).

[23] T. Gissibl, S. Thiele, A. Herkommer, and H. Giessen, "Two-Photon Direct Laser Writing of Ultracompact Multi-Lens Objectives", Nat. Photonics **10**, 554–560 (2016) (Cited on pages 12, 13).

[24] N. Lindenmann, G. Balthasar, D. Hillerkuss, R. Schmogrow, M. Jordan, J. Leuthold, W. Freude, and C. Koos, "Photonic Wire Bonding: A Novel Concept for Chip-Scale Interconnects", Opt. Express **20**, 17667–17677 (2012) (Cited on pages 12, 13).

[25] C. Kern, M. Kadic, and M. Wegener, "Experimental Evidence for Sign Reversal of the Hall Coefficient in Three-Dimensional Metamaterials", Phys. Rev. Lett. **118**, 016601 (2017) (Cited on page 13).

[26] T. Erkert, *Press Release: Third Dimension of Specific Cell Cultivation*, (Mar. 21, 2011) `https://www.kit.edu/kit/english/pi_2011_6187.php` (visited on 11/18/2018) (Cited on page 13).

[27] H.-B. Sun, S. Matsuo, and H. Misawa, "Three-Dimensional Photonic Crystal Structures Achieved with Two-Photon-Absorption Photopolymerization of Resin", Appl. Phys. Lett. **74**, 786–788 (1999) (Cited on pages 12, 87).

[28] G. von Freymann, A. Ledermann, M. Thiel, I. Staude, S. Essig, K. Busch, and M. Wegener, "Three-Dimensional Nanostructures for Photonics", Adv. Funct. Mater. **20**, 1038–1052 (2010) (Cited on page 12).

[29] M. Thiel, M. Decker, M. Deubel, M. Wegener, S. Linden, and G. von Freymann, "Polarization Stop Bands in Chiral Polymeric Three-Dimensional Photonic Crystals", Adv. Mater. **19**, 207–210 (2007) (Cited on page 12).

[30] J. Kaschke and M. Wegener, "Optical and Infrared Helical Metamaterials", Nanophotonics **5**, 510–523 (2016) (Cited on page 12).

[31] C. M. Soukoulis and M. Wegener, "Past Achievements and Future Challenges in the Development of Three-Dimensional Photonic Metamaterials", Nat. Photonics **5**, 523–530 (2011) (Cited on page 12).

[32] Y.-S. Chen, A. Tal, D. B. Torrance, and S. M. Kuebler, "Fabrication and Characterization of Three-Dimensional Silver-Coated Polymeric Microstructures", Adv. Funct. Mater. **16**, 1739–1744 (2006) (Cited on page 12).

[33] A. Frölich and M. Wegener, "Spectroscopic Characterization of Highly Doped ZnO Films Grown by Atomic-Layer Deposition for Three-Dimensional Infrared Metamaterials [Invited]", Opt. Mater. Express **1**, 883–889 (2011) (Cited on page 12).

[34] M. Hermatschweiler, A. Ledermann, G. A. Ozin, M. Wegener, and G. von Freymann, "Fabrication of Silicon Inverse Woodpile Photonic Crystals", Adv. Funct. Mater. **17**, 2273–2277 (2007) (Cited on pages 12, 87).

[35] A. Frölich, J. Fischer, T. Zebrowski, K. Busch, and M. Wegener, "Titania Woodpiles with Complete Three-Dimensional Photonic Bandgaps in the Visible", Adv. Mater. **25**, 3588–3592 (2013) (Cited on pages 12, 37, 87).

[36] S. C. Ligon, J. Kumpfmüller, N. Pucher, J. Stampfl, and R. Liska, "Fabrication of Waveguides and Other Optical Elements by Multiphoton Lithography", in *Multiphoton Lithography* (Wiley-VCH, Weinheim, Germany, 2016), pp. 265–296 (Cited on page 12).

[37] T. Gissibl, S. Thiele, A. Herkommer, and H. Giessen, "Sub-Micrometre Accurate Free-Form Optics by Three-Dimensional Printing on Single-Mode Fibres", Nat. Commun. **7**, 11763 (2016) (Cited on page 12).

[38] M. F. Schumann, S. Wiesendanger, J. C. Goldschmidt, B. Bläsi, K. Bittkau, U. W. Paetzold, A. Sprafke, R. B. Wehrspohn, C. Rockstuhl, and M. Wegener, "Cloaked Contact Grids on Solar Cells by Coordinate Transformations: Designs and Prototypes", Optica **2**, 850–853 (2015) (Cited on page 12).

[39] M. F. Schumann, B. Fritz, R. Eckstein, U. Lemmer, G. Gomard, and M. Wegener, "Cloaking of Metal Grid Electrodes on Lambertian Emitters by Free-Form Refractive Surfaces", Opt. Lett. **43**, 527–530 (2018) (Cited on page 12).

[40] A. Ovsianikov, J. Viertl, B. Chichkov, M. Oubaha, B. MacCraith, I. Sakellari, A. Giakoumaki, D. Gray, M. Vamvakaki, M. Farsari, and C. Fotakis, "Ultra-Low Shrinkage Hybrid Photosensitive Material for Two-Photon Polymerization Microfabrication", ACS Nano **2**, 2257–2262 (2008) (Cited on page 12).

[41] M. Farsari, M. Vamvakaki, and B. N. Chichkov, "Multiphoton Polymerization of Hybrid Materials", J. Opt. **12**, 124001 (2010) (Cited on page 12).

[42] C. N. LaFratta, T. Baldacchini, R. A. Farrer, J. T. Fourkas, M. C. Teich, B. E. A. Saleh, and M. J. Naughton, "Replication of Two-Photon-Polymerized Structures with Extremely High Aspect Ratios and Large Overhangs", J. Phys. Chem. B **108**, 11256–11258 (2004) (Cited on page 12).

[43] T. Frenzel, M. Kadic, and M. Wegener, "Three-Dimensional Mechanical Metamaterials with a Twist", Science **358**, 1072–1074 (2017) (Cited on page 13).

[44] X. Yu, J. Zhou, H. Liang, Z. Jiang, and L. Wu, "Mechanical Metamaterials Associated with Stiffness, Rigidity and Compressibility: A Brief Review", Prog. Mater. Sci. **94**, 114–173 (2018) (Cited on page 13).

[45] J. Qu, M. Kadic, A. Naber, and M. Wegener, "Micro-Structured Two-Component 3D Metamaterials with Negative Thermal-Expansion Coefficient from Positive Constituents", Sci. Rep. **7**, 40643 (2017) (Cited on page 13).

[46] F. Bragheri, R. Martinez Vazquez, and R. Osellame, "Chapter 12.3 - Microfluidics", in *Three-Dimensional Microfabrication Using Two-Photon Polymerization*, edited by T. Baldacchini, Micro and Nano Technologies (William Andrew Publishing, Oxford, 2016), pp. 310–334 (Cited on page 13).

[47] S. Taniguchi and S. Maruo, "Chapter 12.2 - Remotely Driven Micromachines Produced by Two-Photon Microfabrication", in *Three-Dimensional Microfabrication Using Two-Photon Polymerization*, edited by T. Baldacchini, Micro and Nano Technologies (William Andrew Publishing, Oxford, 2016), pp. 293–309 (Cited on page 14).

[48] A. M. Greiner, B. Richter, and M. Bastmeyer, "Micro-Engineered 3d Scaffolds for Cell Culture Studies", Macromol. Biosci. **12**, 1301–1314 (2012) (Cited on page 14).

[49] L. Jonušauskas, S. Rekštytė, E. Skliutas, S. Butkus, and M. Malinauskas, "3D Microfabrication of Complex Structures for Biomedical Applications Via Combination of Subtractive/Additive Direct Laser Writing and 3D Printing", in 11th International Conference BIOMDLORE 2016 (Oct. 28, 2016) (Cited on page 14).

[50] X. Sun, S. Das, J. T. Fourkas, and W. Losert, "Chapter 12.4 - Cell Motility and Nanolithography", in *Three-Dimensional Microfabrication Using Two-Photon Polymerization*, edited by T. Baldacchini, Micro and Nano Technologies (William Andrew Publishing, Oxford, 2016), pp. 335–344 (Cited on page 14).

[51] E. D. Lemma, B. Spagnolo, M. De Vittorio, and F. Pisanello, "Studying Cell Mechanobiology in 3D: The Two-Photon Lithography Approach", Trends Biotechnol. (2018) `10.1016/j.tibtech.2018.09.008` (Cited on page 14).

[52] F. Klein, B. Richter, T. Striebel, C. M. Franz, G. von Freymann, M. Wegener, and M. Bastmeyer, "Two-Component Polymer Scaffolds for Controlled Three-Dimensional Cell Culture", Adv. Mater. **23**, 1341–1345 (2011) (Cited on page 14).

[53] B. Richter, T. Pauloehrl, J. Kaschke, D. Fichtner, J. Fischer, A. M. Greiner, D. Wedlich, M. Wegener, G. Delaittre, C. Barner-Kowollik, and M. Bastmeyer, "Three-Dimensional Microscaffolds Exhibiting Spatially Resolved Surface Chemistry", Adv. Mater. **25**, 6117–6122 (2013) (Cited on pages 14, 62, 69).

[54] A. I. Ciuciu and P. J. Cywiński, "Two-Photon Polymerization of Hydrogels – Versatile Solutions to Fabricate Well-Defined 3d Structures", RSC Adv. **4**, 45504–45516 (2014) (Cited on page 14).

[55] D. Serien and S. Takeuchi, "Fabrication of Submicron Proteinaceous Structures by Direct Laser Writing", Appl. Phys. Lett. **107**, 013702 (2015) (Cited on page 14).

[56] C. Barner-Kowollik, M. Bastmeyer, E. Blasco, G. Delaittre, P. Müller, B. Richter, and M. Wegener, "3D Laser Micro- and Nanoprinting: Challenges for Chemistry", Angew. Chem. Int. Ed. **56**, 15828–15845 (2017) (Cited on pages 14, 41, 146).

[57] S. Shukla, X. Vidal, E. P. Furlani, M. T. Swihart, K.-T. Kim, Y.-K. Yoon, A. Urbas, and P. N. Prasad, "Subwavelength Direct Laser Patterning of Conductive Gold Nanostructures by Simultaneous Photopolymerization and Photoreduction", ACS Nano **5**, 1947–1957 (2011) (Cited on page 14).

[58] E. Blasco, J. Müller, P. Müller, V. Trouillet, M. Schön, T. Scherer, C. Barner-Kowollik, and M. Wegener, "Fabrication of Conductive 3D Gold-Containing Microstructures Via Direct Laser Writing", Adv. Mater. **28**, 3592–3595 (2016) (Cited on page 14).

[59] Q. Guo, S. Xiao, A. Aumann, M. Jaeger, M. Chakif, R. Ghadiri, C. Esen, M. Ma, and A. Ostendorf, "Using Laser Microfabrication to Write Conductive Polymer/SWNTs Nanocomposites.", J. Laser Micro. Nanoen. **7** (2012) (Cited on page 14).

[60] S. Ushiba, S. Shoji, K. Masui, P. Kuray, J. Kono, and S. Kawata, "3D Microfabrication of Single-Wall Carbon Nanotube/Polymer Composites by Two-Photon Polymerization Lithography", Carbon **59**, 283–288 (2013) (Cited on page 14).

[61] E. Blasco, B. Yameen, A. S. Quick, P. Krolla-Sidenstein, A. Welle, M. Wegener, and C. Barner-Kowollik, "Designing π-Conjugated Polymeric Nano- and Microstructures Via Light Induced Chemistry", Macromolecules **48**, 8718–8728 (2015) (Cited on pages 14, 62).

[62] M. M. Zieger, P. Mueller, A. S. Quick, M. Wegener, and C. Barner-Kowollik, "Cleaving Direct-Laser-Written Microstructures on Demand", Angew. Chem. Int. Ed. **56**, 5625–5629 (2017) (Cited on page 14).

[63] M. M. Zieger, P. Müller, E. Blasco, C. Petit, V. Hahn, L. Michalek, H. Mutlu, M. Wegener, and C. Barner-Kowollik, "A Subtractive Photoresist Platform for Micro- and Macroscopic 3D Printed Structures", Adv. Funct. Mater. **28**, 1801405 (2018) (Cited on pages 14, 90).

[64] D. Gräfe, A. Wickberg, M. M. Zieger, M. Wegener, E. Blasco, and C. Barner-Kowollik, "Adding Chemically Selective Subtraction to Multi-Material 3D Additive Manufacturing", Nat. Commun. **9**, 2788 (2018) (Cited on page 14).

[65] D. Martella, S. Nocentini, D. Nuzhdin, C. Parmeggiani, and D. S. Wiersma, "Photonic Microhand with Autonomous Action", Adv. Mater. **29**, 1704047 (2017) (Cited on page 14).

[66] Y.-H. Lee, D. Franklin, F. Gou, G. Liu, F. Peng, D. Chanda, and S.-T. Wu, "Two-Photon Polymerization Enabled Multi-Layer Liquid Crystal Phase Modulator", Sci. Rep. **7**, 16260 (2017) (Cited on page 14).

[67] G. de Miguel, G. Vicidomini, B. Harke, and A. Diaspro, "Chapter 8 - Linewidth and Writing Resolution", in *Three-Dimensional Microfabrication Using Two-Photon Polymerization*, edited by T. Baldacchini, Micro and Nano Technologies (William Andrew Publishing, Oxford, 2016), pp. 190–220 (Cited on pages 15, 30, 35, 147).

[68] S. Lee, J. Byers, K. Jen, P. Zimmerman, B. Rice, N. J. Turro, and C. G. Will-son, "An Analysis of Double Exposure Lithography Options", in Optical Microlithography XXI, Vol. 6924 (2008), 69242A (Cited on page 15).

[69] E. H. Waller and G. von Freymann, "Spatio-Temporal Proximity Characteristics in 3D μ-Printing via Multi-Photon Absorption", Polymers **8**, 297 (2016) (Cited on pages 15, 147).

[70] M. Thiel, J. Fischer, G. Von Freymann, and M. Wegener, "Direct Laser Writing of Three-Dimensional Submicron Structures Using a Continuous-Wave Laser at 532 Nm", Appl. Phys. Lett. **97**, 221102–221102 (2010) (Cited on pages 16, 96).

[71] J. Fischer, "Three-Dimensional Optical Lithography Beyond the Diffraction Limit", PhD Thesis (Karlsruhe Institute of Technology (KIT), 2012) (Cited on pages 17, 154).

[72] J. Fischer, J. B. Mueller, J. Kaschke, T. J. Wolf, A.-N. Unterreiner, and M. Wegener, "Three-Dimensional Multi-Photon Direct Laser Writing with Variable Repetition Rate", Opt. Express **21**, 26244–26260 (2013) (Cited on pages 18, 44, 94, 96).

[73] Z. Tomova, N. Liaros, S. A. Gutierrez Razo, S. M. Wolf, and J. T. Fourkas, "In Situ Measurement of the Effective Nonlinear Absorption Order in Multiphoton Photoresists", Laser Photonics Rev. **10**, 849–854 (2016) (Cited on page 18).

[74] A. Pikulin and N. Bityurin, "Spatial Resolution in Polymerization of Sample Features at Nanoscale", Phys. Rev. B **75**, 195430 (2007) (Cited on pages 19, 96).

[75] A. Pikulin and N. Bityurin, "Spatial Confinement of Percolation: Monte Carlo Modeling and Nanoscale Laser Polymerization", Phys. Rev. B **82**, 085406 (2010) (Cited on pages 19, 96).

[76] A. V. Pikulin and N. M. Bityurin, "Fluctuation Limitations on the Voxel Minimal Size at Laser Nanopolymerization", Tech. Phys. **57**, 697–705 (2012) (Cited on pages 19, 96).

[77] S. Wang, Y. Yu, H. Liu, K. T. P. Lim, B. M. Srinivasan, Y. W. Zhang, and J. K. W. Yang, "Sub-10-Nm Suspended Nano-Web Formation by Direct Laser Writing", Nano Futures **2**, 025006 (2018) (Cited on pages 19, 39).

166

[78] C. Mack, *Fundamental Principles of Optical Lithography: The Science of Microfabrication*, 1st edition (Wiley-Interscience, Chichester, England, 2007), 534 pp. (Cited on pages 20, 24).

[79] C. M. Sparrow, "On Spectroscopic Resolving Power", Astrophys. J. **44**, 76 (1916) (Cited on page 21).

[80] H. Blom and J. Widengren, "Stimulated Emission Depletion Microscopy", Chem. Rev. **117**, 7377–7427 (2017) (Cited on pages 24, 28, 30, 140).

[81] M. J. Rust, M. Bates, and X. Zhuang, "Sub-Diffraction-Limit Imaging by Stochastic Optical Reconstruction Microscopy (STORM)", Nat. Methods **3**, 793–796 (2006) (Cited on page 24).

[82] E. Betzig, G. H. Patterson, R. Sougrat, O. W. Lindwasser, S. Olenych, J. S. Bonifacino, M. W. Davidson, J. Lippincott-Schwartz, and H. F. Hess, "Imaging Intracellular Fluorescent Proteins at Nanometer Resolution", Science **313**, 1642–1645 (2006) (Cited on page 24).

[83] S. W. Hell, "Toward Fluorescence Nanoscopy", Nat. Biotechnol. **21**, 1347–1355 (2003) (Cited on pages 25, 26).

[84] T. A. Klar and S. W. Hell, "Subdiffraction Resolution in Far-Field Fluorescence Microscopy", Opt. Lett. **24**, 954–956 (1999) (Cited on page 25).

[85] S. W. Hell, "Microscopy and Its Focal Switch", Nat. Methods **6**, 24–32 (2009) (Cited on page 26).

[86] S. W. Hell and M. Kroug, "Ground-State-Depletion Fluorscence Microscopy: A Concept for Breaking the Diffraction Resolution Limit", Appl. Phys. B **60**, 495–497 (1995) (Cited on page 26).

[87] M. Bossi, J. Fölling, M. Dyba, V. Westphal, and S. W. Hell, "Breaking the Diffraction Resolution Barrier in Far-Field Microscopy by Molecular Optical Bistability", New J. Phys. **8**, 275 (2006) (Cited on pages 26, 106).

[88] J. Fölling, V. Belov, R. Kunetsky, R. Medda, A. Schönle, A. Egner, C. Eggeling, M. Bossi, and S. W. Hell, "Photochromic Rhodamines Provide Nanoscopy with Optical Sectioning", Angew. Chem. Int. Ed. **46**, 6266–6270 (2007) (Cited on pages 26, 106).

[89] M. Hofmann, C. Eggeling, S. Jakobs, and S. W. Hell, "Breaking the Diffraction Barrier in Fluorescence Microscopy at Low Light Intensities by Using Reversibly Photoswitchable Proteins", Proc. Natl. Acad. Sci. U.S.A. **102**, 17565–17569 (2005) (Cited on pages 26, 106).

[90] K. I. Willig, A. C. Stiel, T. Brakemann, S. Jakobs, and S. W. Hell, "Dual-Label STED Nanoscopy of Living Cells Using Photochromism", Nano Lett. **11**, 3970–3973 (2011) (Cited on pages 26, 106).

[91] T. Grotjohann, I. Testa, M. Leutenegger, H. Bock, N. T. Urban, F. Lavoie-Cardinal, K. I. Willig, C. Eggeling, S. Jakobs, and S. W. Hell, "Diffraction-Unlimited All-Optical Imaging and Writing with a Photochromic GFP", Nature **478**, 204–208 (2011) (Cited on pages 26, 106, 107).

[92] P. Dedecker, G. C. H. Mo, T. Dertinger, and J. Zhang, "Widely Accessible Method for Superresolution Fluorescence Imaging of Living Systems", Proc. Natl. Acad. Sci. U.S.A. **109**, 10909–10914 (2012) (Cited on pages 26, 106).

[93] S. Hell, S. Jakobs, and L. Kastrup, "Imaging and Writing at the Nanoscale with Focused Visible Light through Saturable Optical Transitions", Appl. Phys. A **77**, 859–860 (2003) (Cited on pages 26, 30).

[94] B. Harke, J. Keller, C. K. Ullal, V. Westphal, A. Schönle, and S. W. Hell, "Resolution Scaling in STED Microscopy", Opt. Express **16**, 4154–4162 (2008) (Cited on pages 26, 30).

[95] V. Westphal and S. W. Hell, "Nanoscale Resolution in the Focal Plane of an Optical Microscope", Phys. Rev. Lett. **94**, 143903 (2005) (Cited on pages 27, 49).

[96] E. Rittweger, K. Y. Han, S. E. Irvine, C. Eggeling, and S. W. Hell, "STED Microscopy Reveals Crystal Colour Centres with Nanometric Resolution", Nat. Photonics **3**, 144–147 (2009) (Cited on page 28).

[97] K. I. Willig, B. Harke, R. Medda, and S. W. Hell, "STED Microscopy with Continuous Wave Beams", Nat. Methods **4**, 915–918 (2007) (Cited on page 28).

[98] T. A. Klar, E. Engel, and S. W. Hell, "Breaking Abbe's Diffraction Resolution Limit in Fluorescence Microscopy with Stimulated Emission Depletion Beams of Various Shapes", Phys. Rev. E **64**, 066613 (2001) (Cited on pages 28, 82).

[99] D. Wildanger, J. Bückers, V. Westphal, S. W. Hell, and L. Kastrup, "A STED Microscope Aligned by Design", Opt. Express **17**, 16100–16110 (2009) (Cited on page 30).

[100] M. Reuss, J. Engelhardt, and S. W. Hell, "Birefringent Device Converts a Standard Scanning Microscope into a STED Microscope That Also Maps Molecular Orientation", Opt. Express **18**, 1049–1058 (2010) (Cited on page 30).

[101] L. Li, R. R. Gattass, E. Gershgoren, H. Hwang, and J. T. Fourkas, "Achieving $\lambda/20$ Resolution by One-Color Initiation and Deactivation of Polymerization", Science **324**, 910–913 (2009) (Cited on pages 30, 35, 37, 39).

[102] T. F. Scott, B. A. Kowalski, A. C. Sullivan, C. N. Bowman, and R. R. McLeod, "Two-Color Single-Photon Photoinitiation and Photoinhibition for Subdiffraction Photolithography", Science **324**, 913–917 (2009) (Cited on pages 30, 38).

[103] T. A. Klar, R. Wollhofen, and J. Jacak, "Sub-Abbe Resolution: From STED Microscopy to STED Lithography", Phys. Scr. **2014**, 014049 (2014) (Cited on pages 30, 35).

[104] J. T. Fourkas, "STED-Inspired Approaches to Resolution Enhancement", in *Multiphoton Lithography* (John Wiley & Sons, Ltd, 2016), pp. 111–131 (Cited on pages 30, 35, 147).

[105] J. Fischer, G. von Freymann, and M. Wegener, "The Materials Challenge in Diffraction-Unlimited Direct-Laser-Writing Optical Lithography", Adv. Mater. **22**, 3578–3582 (2010) (Cited on pages 35, 38, 39).

[106] J. Fischer and M. Wegener, "Ultrafast Polymerization Inhibition by Stimulated Emission Depletion for Three-Dimensional Nanolithography", Adv. Mater. **24**, OP65–OP69 (2012) (Cited on pages 35, 36, 75, 99, 129).

[107] B. Harke, W. Dallari, G. Grancini, D. Fazzi, F. Brandi, A. Petrozza, and A. Diaspro, "Polymerization Inhibition by Triplet State Absorption for Nanoscale Lithography", Adv. Mater. **25**, 904–909 (2013) (Cited on pages 35, 38).

[108] T. J. A. Wolf, J. Fischer, M. Wegener, and A.-N. Unterreiner, "Pump–Probe Spectroscopy on Photoinitiators for Stimulated-Emission-Depletion Optical Lithography", Opt. Lett. **36**, 3188–3190 (2011) (Cited on pages 36, 38).

[109] J. Fischer and M. Wegener, "Three-Dimensional Direct Laser Writing Inspired by Stimulated-Emission-Depletion Microscopy (Invited)", Opt. Mater. Express **1**, 614–624 (2011) (Cited on pages 36, 37).

[110] J. Kaschke and M. Wegener, "Gold Triple-Helix Mid-Infrared Metamaterial by STED-Inspired Laser Lithography", Opt. Lett. **40**, 3986–3989 (2015) (Cited on pages 36, 37).

[111] R. Wollhofen, J. Katzmann, C. Hrelescu, J. Jacak, and T. A. Klar, "120 Nm Resolution and 55 Nm Structure Size in STED-Lithography", Opt. Express **21**, 10831–10840 (2013) (Cited on pages 36, 134, 138, 141).

[112] J. Fischer, T. Ergin, and M. Wegener, "Three-Dimensional Polarization-Independent Visible-Frequency Carpet Invisibility Cloak", Opt. Lett. **36**, 2059–2061 (2011) (Cited on page 37).

[113] M. Thiel, J. Ott, A. Radke, J. Kaschke, and M. Wegener, "Dip-in Depletion Optical Lithography of Three-Dimensional Chiral Polarizers", Opt. Lett. **38**, 4252–4255 (2013) (Cited on page 37).

[114] J. Kaschke, L. Blume, L. Wu, M. Thiel, K. Bade, Z. Yang, and M. Wegener, "A Helical Metamaterial for Broadband Circular Polarization Conversion", Adv. Opt. Mater. **3**, 1411–1417 (2015) (Cited on page 37).

[115] B. Buchegger, J. Kreutzer, B. Plochberger, R. Wollhofen, D. Sivun, J. Jacak, G. J. Schütz, U. Schubert, and T. A. Klar, "Stimulated Emission Depletion Lithography with Mercapto-Functional Polymers", ACS Nano **10**, 1954–1959 (2016) (Cited on page 37).

[116] R. Wollhofen, B. Buchegger, C. Eder, J. Jacak, J. Kreutzer, and T. A. Klar, "Functional Photoresists for Sub-Diffraction Stimulated Emission Depletion Lithography", Opt. Mater. Express **7**, 2538–2559 (2017) (Cited on page 37).

[117] E. Murtezi, S. Puthukodan, J. Jacak, and T. A. Klar, "Biofunctionalization of Sub-Diffractionally Patterned Polymer Structures by Photobleaching", ACS Appl. Mater. Interfaces **10**, 31850–31854 (2018) (Cited on page 37).

[118] A. G. Vitukhnovsky, D. A. Chubich, S. P. Eliseev, V. V. Sychev, D. A. Kolymagin, and A. S. Selyukov, "Advantages of STED-Inspired 3D Direct Laser Writing for Fabrication of Hybrid Nanostructures", J. Russ. Laser Res. **38**, 375–382 (2017) (Cited on page 37).

[119] J. Fischer, J. B. Mueller, A. S. Quick, J. Kaschke, C. Barner-Kowollik, and M. Wegener, "Exploring the Mechanisms in STED-Enhanced Direct Laser Writing", Adv. Opt. Mater. **3**, 221–232 (2015) (Cited on pages 37, 44).

[120] B. Harke, P. Bianchini, F. Brandi, and A. Diaspro, "Photopolymerization Inhibition Dynamics for Sub-Diffraction Direct Laser Writing Lithography", ChemPhysChem **13**, 1429–1434 (2012) (Cited on page 38).

[121] M. Elmeranta, G. Vicidomini, M. Duocastella, A. Diaspro, and G. de Miguel, "Characterization of Nanostructures Fabricated with Two-Beam DLW Lithography Using STED Microscopy", Opt. Mater. Express **6**, 3169 (2016) (Cited on page 38).

[122] Y. Cao, Z. Gan, B. Jia, R. A. Evans, and M. Gu, "High-Photosensitive Resin for Super-Resolution Direct-Laser-Writing Based on Photoinhibited Polymerization", Opt. Express **19**, 19486 (2011) (Cited on pages 38, 40).

[123] Z. Gan, Y. Cao, R. A. Evans, and M. Gu, "Three-Dimensional Deep Sub-Diffraction Optical Beam Lithography with 9 Nm Feature Size", Nat. Commun. **4**, 2061 (2013) (Cited on page 38).

[124] D. L. Forman, M. C. Cole, and R. R. McLeod, "Radical Diffusion Limits to Photoinhibited Superresolution Lithography", Phys. Chem. Chem. Phys. **15**, 14862–14867 (2013) (Cited on page 39).

[125] Z. Gan, M. D. Turner, and M. Gu, "Biomimetic Gyroid Nanostructures Exceeding Their Natural Origins", Sci. Adv. **2**, e1600084 (2016) (Cited on page 40).

[126] R. Menon and H. I. Smith, "Absorbance-Modulation Optical Lithography", J. Opt. Soc. Am. A **23**, 2290–2294 (2006) (Cited on page 41).

[127] T. L. Andrew, H.-Y. Tsai, and R. Menon, "Confining Light to Deep Subwavelength Dimensions to Enable Optical Nanopatterning", Science **324**, 917–921 (2009) (Cited on pages 41, 107).

[128] N. Brimhall, T. L. Andrew, R. V. Manthena, and R. Menon, "Breaking the Far-Field Diffraction Limit in Optical Nanopatterning via Repeated Photochemical and Electrochemical Transitions in Photochromic Molecules", Phys. Rev. Lett. **107**, 205501 (2011) (Cited on page 41).

[129] A. Majumder, X. Wan, F. Masid, B. J. Pollock, T. L. Andrew, O. Soppera, and R. Menon, "Reverse-Absorbance-Modulation-Optical Lithography for Optical Nanopatterning at Low Light Levels", AIP Advances **6**, 065312 (2016) (Cited on pages 41, 107).

[130] P. Cantu, N. Brimhall, T. L. Andrew, R. Castagna, C. Bertarelli, and R. Menon, "Subwavelength Nanopatterning of Photochromic Diarylethene Films", Appl. Phys. Lett. **100**, 183103 (2012) (Cited on pages 41, 107).

[131] J. B. Pendry, "Negative Refraction Makes a Perfect Lens", Phys. Rev. Lett. **85**, 3966–3969 (2000) (Cited on page 41).

[132] D. Lu and Z. Liu, "Hyperlenses and Metalenses for Far-Field Super-Resolution Imaging", Nat. Commun. **3**, 1205 (2012) (Cited on page 41).

[133] P. Gao, X. Li, Z. Zhao, X. Ma, M. Pu, C. Wang, and X. Luo, "Pushing the Plasmonic Imaging Nanolithography to Nano-Manufacturing", Opt. Commun. **404**, 62–72 (2017) (Cited on page 41).

[134] J. Sun and N. M. Litchinitser, "Toward Practical, Subwavelength, Visible-Light Photolithography with Hyperlens", ACS Nano **12**, 542–548 (2018) (Cited on page 41).

[135] S. K. Gupta and A. Kumar, *Reaction Engineering of Step Growth Polymerization*, The Plenum Chemical Engineering Series (Springer US, 1987) (Cited on pages 42, 96).

[136] A. S. Quick, H. Rothfuss, A. Welle, B. Richter, J. Fischer, M. Wegener, and C. Barner-Kowollik, "Fabrication and Spatially Resolved Functionalization of 3D Microstructures via Multiphoton-Induced Diels–Alder Chemistry", Adv. Funct. Mater. **24**, 3571–3580 (2014) (Cited on pages 44, 62, 67, 87, 90, 143).

[137] B. H. Ong, X. Yuan, and S. C. Tjin, "Adjustable Refractive Index Modulation for a Waveguide with SU-8 Photoresist by Dual-UV Exposure Lithography", Appl. Opt. **45**, 8036–8039 (2006) (Cited on page 50).

[138] P. Mueller, M. M. Zieger, B. Richter, A. S. Quick, J. Fischer, J. B. Mueller, L. Zhou, G. U. Nienhaus, M. Bastmeyer, C. Barner-Kowollik, and M. Wegener, "Molecular Switch for Sub-Diffraction Laser Lithography by Photoenol Intermediate-State Cis–Trans Isomerization", ACS Nano **11**, 6396–6403 (2017) (Cited on pages 53, 56, 64, 69, 71, 74, 76–78, 80, 81, 83, 84, 86).

[139] P. Müller, R. Müller, L. Hammer, C. Barner-Kowollik, M. Wegener, and E. Blasco, "STED-Inspired Laser Lithography Based on Photoswitchable Spirothiopyran Moieties", Chem. Mater. (2019) 10.1021/acs.chemmater.8b04696 (Cited on pages 54, 59, 111, 118, 119, 121, 123–125, 127, 128, 131, 133, 134, 136, 137).

[140] K. Matyjaszewski, "Atom Transfer Radical Polymerization (ATRP): Current Status and Future Perspectives", Macromolecules **45**, 4015–4039 (2012) (Cited on page 57).

[141] C. Rodriguez-Emmenegger, C. M. Preuss, B. Yameen, O. Pop-Georgievski, M. Bachmann, J. O. Mueller, M. Bruns, A. S. Goldmann, M. Bastmeyer, and C. Barner-Kowollik, "Controlled Cell Adhesion on Poly(Dopamine) Interfaces Photopatterned with Non-Fouling Brushes", Adv. Mater. **25**, 6123–6127 (2013) (Cited on pages 57, 69).

[142] P. G. Sammes, "Photoenolisation", Tetrahedron **32**, 405–422 (1976) (Cited on pages 62, 66).

[143] J. Sankaranarayanan, S. Muthukrishnan, and A. D. Gudmundsdottir, "Photoremovable Protecting Groups Based on Photoenolization", Adv. Phys. Org. Chem. **43**, 39–77 (2009) (Cited on pages 62, 76, 155, 157).

[144] P. Klán, T. Šolomek, C. G. Bochet, A. Blanc, R. Givens, M. Rubina, V. Popik, A. Kostikov, and J. Wirz, "Photoremovable Protecting Groups in Chemistry and Biology: Reaction Mechanisms and Efficacy", Chem. Rev. **113**, 119–191 (2013) (Cited on page 62).

[145] E. Blasco, M. Wegener, and C. Barner-Kowollik, "Photochemically Driven Polymeric Network Formation: Synthesis and Applications", Adv. Mater. **29**, 1604005 (2017) (Cited on page 62).

[146] M. A. B. Meador, M. A. Meador, L. L. Williams, and D. A. Scheiman, "Diels-Alder Trapping of Photochemically Generated Dienes with a Bismaleimide: A New Approach to Polyimide Synthesis", Macromolecules **29**, 8983–8986 (1996) (Cited on page 62).

[147] T. Gruendling, K. K. Oehlenschlaeger, E. Frick, M. Glassner, C. Schmid, and C. Barner-Kowollik, "Rapid UV Light-Triggered Macromolecular Click Conjugations via the Use of o-Quinodimethanes", Macromol. Rapid Commun. **32**, 807–812 (2011) (Cited on page 62).

[148] K. K. Oehlenschlaeger, J. O. Mueller, N. B. Heine, M. Glassner, N. K. Guimard, G. Delaittre, F. G. Schmidt, and C. Barner-Kowollik, "Light-Induced Modular Ligation of Conventional RAFT Polymers", Angew. Chem. Int. Ed. **52**, 762–766 (2013) (Cited on page 62).

[149] T. Pauloehrl, G. Delaittre, V. Winkler, A. Welle, M. Bruns, H. G. Börner, A. M. Greiner, M. Bastmeyer, and C. Barner-Kowollik, "Adding Spatial Control to Click Chemistry: Phototriggered Diels–Alder Surface (Bio)Functionalization at Ambient Temperature", Angew. Chem. Int. Ed. **51**, 1071–1074 (2012) (Cited on pages 62, 69).

[150] T. K. Claus, B. Richter, V. Hahn, A. Welle, S. Kayser, M. Wegener, M. Bastmeyer, G. Delaittre, and C. Barner-Kowollik, "Simultaneous Dual Encoding of Three-Dimensional Structures by Light-Induced Modular Ligation", Angew. Chem. Int. Ed. **55**, 3817–3822 (2016) (Cited on page 62).

[151] B. Richter, V. Hahn, S. Bertels, T. K. Claus, M. Wegener, G. Delaittre, C. Barner-Kowollik, and M. Bastmeyer, "Guiding Cell Attachment in 3D Microscaffolds Selectively Functionalized with Two Distinct Adhesion Proteins", Adv. Mater. **29**, 1604342 (2017) (Cited on page 62).

[152] L. Fruk, A. Kerbs, P. Mueller, M. Kaupp, I. Ahmed, A. S. Quick, D. Abt, M. Wegener, C. M. Niemeyer, and C. Barner-Kowollik, "Photo-Induced Click Chemistry for DNA Surface Structuring via Direct Laser Writing", Chem. Eur. J. **23**, 4990–4994 (2017) (Cited on page 62).

[153] M. Kaupp, K. Hiltebrandt, V. Trouillet, P. Mueller, A. S. Quick, M. Wegener, and C. Barner-Kowollik, "Wavelength Selective Polymer Network Formation of End-Functional Star Polymers", Chem. Commun. **52**, 1975–1978 (2016) (Cited on pages 62, 90).

[154] A. D. Walsh, "The Absorption Spectra of Furfuraldehyde and Benzaldehyde in the Vacuum Ultra-Violet", Trans. Faraday Soc. **42**, 62–65 (1946) (Cited on page 63).

[155] J. P. Menzel, B. B. Noble, A. Lauer, M. L. Coote, J. P. Blinco, and C. Barner-Kowollik, "Wavelength Dependence of Light-Induced Cycloadditions", J. Am. Chem. Soc. **139**, 15812–15820 (2017) (Cited on page 63).

[156] A. P. Pellicciöli, P. Klán, M. Zabadal, and J. Wirz, "Photorelease of HCl from O-Methylphenacyl Chloride Proceeds through the Z-Xylylenol", J. Am. Chem. Soc. **123**, 7931–7932 (2001) (Cited on pages 64, 68).

[157] S. M. Mellows and P. G. Sammes, "Stereoselective Trapping of a Photo-Enol", J. Chem. Soc. D **0**, 21–22 (1971) (Cited on page 64).

[158] W. R. Roth, M. Biermann, H. Dekker, R. Jochems, C. Mosselman, and H. Hermann, "Das Energieprofil des o-Chinodimethan-Benzocyclobuten-Gleichgewichtes", Chem. Ber. **111**, 3892–3903 (1978) (Cited on page 65).

[159] C. Petit, L. D. Bangert, M. Abbasi, M. Wilhelm, A. S. Goldmann, and C. Barner-Kowollik, "Stability of Diels–Alder Photoadducts in Macromolecules", Polym. Chem. **9**, 3850–3854 (2018) (Cited on page 66).

[160] H. C. Kolb, M. G. Finn, and K. B. Sharpless, "Click Chemistry: Diverse Chemical Function from a Few Good Reactions", Angew. Chem. Int. Ed. **40**, 2004–2021 (2001) (Cited on pages 66, 109).

[161] W. H. Binder and R. Sachsenhofer, "'Click' Chemistry in Polymer and Materials Science", Macromol. Rapid Commun. **28**, 15–54 (2007) (Cited on pages 66, 109).

[162] T. Krappitz, F. Feist, I. Lamparth, N. Moszner, H. John, J. P. Blinco, T. R. Dargaville, and C. Barner-Kowollik, "Polymer Networks Based on Photo-Caged Diene Dimerization", Mater. Horiz. **6**, 81–89 (2019) (Cited on pages 66, 88, 93, 96).

[163] J. C. Netto-Ferreira and J. C. Scaiano, "A Laser Flash Photolysis Study of the Mechanism of the Photocyclization of α-Chloro-o-Methylacetophenones", J. Am. Chem. Soc. **113**, 5800–5803 (1991) (Cited on pages 66, 155).

[164] J. Fischer, B. Richter, A. Quick, J. Mueller, M. Bastmeyer, C. Barner-kowollik, and M. Wegener, "Highly Resolved Photochemistry Below the Diffraction Limit by Means of Switchable Photo-Enolization", pat. 20180149972 (United States) (Karlsruher Institut für Technologie (Karlsruhe, DE), May 31, 2018) (Cited on page 68).

[165] A. S. Quick, "Functional Microstructures via Direct Laser Writing", PhD thesis (Karlsruhe, 2015) (Cited on pages 68, 87).

[166] P. Mueller, B. Richter, A. Quick, J. Fischer, J. B. Mueller, L. Zhou, G. U. Nienhaus, M. Bastmeyer, C. Barner-Kowollik, and M. Wegener, "Photoenol Laser Lithography Using Intermediate-State Cis-Trans Isomerization for Writing Inhibition", in Conference on Lasers and Electro-Optics (2016) (June 5, 2016), SW4L.3 (Cited on page 69).

[167] D. M. Jones and W. T. S. Huck, "Controlled Surface-Initiated Polymerizations in Aqueous Media", Adv. Mater. **13**, 1256–1259 (2001) (Cited on page 70).

[168] D. M. Jones, A. A. Brown, and W. T. S. Huck, "Surface-Initiated Polymerizations in Aqueous Media: Effect of Initiator Density", Langmuir **18**, 1265–1269 (2002) (Cited on page 70).

[169] R. W. Redmond and J. C. Scaiano, "Photoenol Biradicals as Singlet Oxygen Sensitizers", J. Phys. Chem. **93**, 5347–5349 (1989) (Cited on page 74).

[170] W.-K. Lee, M. Patra, P. Linse, and S. Zauscher, "Scaling Behavior of Nanopatterned Polymer Brushes", Small **3**, 63–66 (2007) (Cited on page 81).

[171] T. Wu, K. Efimenko, and J. Genzer, "Combinatorial Study of the Mushroom-to-Brush Crossover in Surface Anchored Polyacrylamide", J. Am. Chem. Soc. **124**, 9394–9395 (2002) (Cited on page 81).

[172] K. M. Ho, C. T. Chan, C. M. Soukoulis, R. Biswas, and M. Sigalas, "Photonic Band Gaps in Three Dimensions: New Layer-by-Layer Periodic Structures", Solid State Commun. **89**, 413–416 (1994) (Cited on page 87).

[173] A. C. F. Hoole, M. E. Welland, and A. N. Broers, "Negative PMMA as a High-Resolution Resist - the Limits and Possibilities", Semicond. Sci. Technol. **12**, 1166–1170 (1997) (Cited on pages 87, 143).

[174] U. Okoroanyanwu, *Chemistry and Lithography* (SPIE Press, Hoboken, N.J. : Bellingham, Wash., USA, 2011), 861 pp. (Cited on pages 87, 143, 146, 155, 157).

[175] R. A. Lawson, L. M. Tolbert, T. R. Younkin, and C. L. Henderson, "Negative-Tone Molecular Resists Based on Cationic Polymerization", in Advances in Resist Materials and Processing Technology XXVI (2009) (Apr. 1, 2009), 72733E (Cited on pages 93, 126, 143, 146).

[176] J. B. Müller, "Exploring the Mechanisms of Three-Dimensional Direct Laser Writing by Multi-Photon Polymerization", PhD Thesis (Karlsruhe Institute of Technology (KIT), 2015) (Cited on page 96).

[177] L. J. Jiang, Y. S. Zhou, W. Xiong, Y. Gao, X. Huang, L. Jiang, T. Baldacchini, J.-F. Silvain, and Y. F. Lu, "Two-Photon Polymerization: Investigation of Chemical and Mechanical Properties of Resins Using Raman Microspectroscopy", Opt. Lett. **39**, 3034–3037 (2014) (Cited on page 97).

[178] W. Limm, D. Stanton, G. P. Dimnik, M. A. Winnik, and B. A. Smith, "Solvent Penetration and Photoresist Dissolution: A Fluorescence Quenching and Interferometry Study", J. Appl. Polym. Sci. **35**, 2099–2116 (1988) (Cited on pages 104, 135, 141).

[179] T. Tanaka, M. Morigami, and N. Atoda, "Mechanism of Resist Pattern Collapse during Development Process", Jpn. J. Appl. Phys. **32**, 6059 (1993) (Cited on pages 104, 135, 141).

[180] K. Nakazawa, E. Shiobara, M. Asano, Y. Sato, S. Tanaka, and Y. Oonishi, "Characterization of Microbridges Generated on Negative Resist Patterns", Jpn. J. Appl. Phys. **38**, 1569 (1999) (Cited on pages 104, 135, 141).

[181] K. Matsunaga, H. Oizumi, K. Kaneyama, G. Shiraishi, K. Matsumaro, J. J. Santillan, and T. Itani, "Development of Resist Material and Process for Hp-2x-Nm Devices Using EUV Lithography", in Extreme Ultraviolet (EUV) Lithography, Vol. 7636 (Mar. 20, 2010), 76360S (Cited on pages 104, 135, 141).

[182] S. Yasin, D. G. Hasko, and H. Ahmed, "Fabrication of <5 Nm Width Lines in Poly(Methylmethacrylate) Resist Using a Water:Isopropyl Alcohol Developer and Ultrasonically-Assisted Development", Appl. Phys. Lett. **78**, 2760–2762 (2001) (Cited on page 104).

[183] M. J. Rooks, E. Kratschmer, R. Viswanathan, J. Katine, R. E. F. Jr, and S. A. MacDonald, "Low Stress Development of Poly(Methylmethacrylate) for High Aspect Ratio Structures", J. Vac. Sci. Technol. B (2002) (Cited on page 104).

[184] S. Yasin, D. G. Hasko, and H. Ahmed, "Comparison of MIBK/IPA and Water/IPA as PMMA Developers for Electron Beam Nanolithography", Microelectron. Eng. **61-62**, 745–753 (2002) (Cited on page 104).

[185] J. C. Crano and R. J. Guglielmetti, eds., *Organic Photochromic and Thermochromic Compounds: Main Photochromic Families*, Topics in Applied Chemistry (Springer US, 1999) (Cited on page 106).

[186] A. Bianco, S. Perissinotto, M. Garbugli, G. Lanzani, and C. Bertarelli, "Control of Optical Properties through Photochromism: A Promising Approach to Photonics", Laser Photonics Rev. **5**, 711–736 (2011) (Cited on page 106).

[187] U. Böhm, S. W. Hell, and R. Schmidt, "4Pi-RESOLFT Nanoscopy", Nat. Commun. **7**, 10504 (2016) (Cited on page 106).

[188] R. Klajn, "Spiropyran-Based Dynamic Materials", Chem. Soc. Rev. **43**, 148–184 (2014) (Cited on pages 107, 108, 112, 140).

[189] M. Bertoldo, S. Nazzi, G. Zampano, and F. Ciardelli, "Synthesis and Photochromic Response of a New Precisely Functionalized Chitosan with "Clicked" Spiropyran", Carbohydrate Polymers **85**, 401–407 (2011) (Cited on page 107).

[190] M. Hirano, A. Miyashita, and H. Nohira, "Synthesis and Metastable Structure of New Photochromic Spiroindolinobenzothiopyrans", Chem. Lett. **20**, 209–212 (1991) (Cited on page 108).

[191] M. Bletz, U. Pfeifer-Fukumura, U. Kolb, and W. Baumann, "Ground- and First-Excited-Singlet-State Electric Dipole Moments of Some Photochromic Spirobenzopyrans in Their Spiropyran and Merocyanine Form", J. Phys. Chem. A **106**, 2232–2236 (2002) (Cited on page 108).

[192] M.-Q. Zhu, L. Zhu, J. J. Han, W. Wu, J. K. Hurst, and A. D. Q. Li, "Spiropyran-Based Photochromic Polymer Nanoparticles with Optically Switchable Luminescence", J. Am. Chem. Soc. **128**, 4303–4309 (2006) (Cited on page 108).

[193] K. Ichimura and M. Sakuragi, "A Spiropyran-Iodonium Salt System as a Two Photon Radical Photoinitiator", J. Polym. Sci. C Polym. Lett. **26**, 185–189 (1988) (Cited on page 108).

[194] S. K. Lee and D. C. Neckers, "Two-Photon Radical-Photoinitiator System Based on Iodinated Benzospiropyrans", Chem. Mater. **3**, 858–864 (1991) (Cited on page 108).

[195] M. Irie, T. Iwayanagi, and Y. Taniguchi, "Photoresponsive Polymers. 7. Reversible Solubility Change of Polystyrene Having Pendant Spirobenzopyran Groups and Its Application to Photoresists", Macromolecules **18**, 2418–2422 (1985) (Cited on page 109).

[196] V. A. Krongauz and E. S. Goldburt, "Quasi-Crystals from Irradiated Photochromic Dyes in an Applied Electric Field", Nature **271**, 43–45 (1978) (Cited on pages 109, 124).

[197] M. Piech, M. C. George, N. S. Bell, and P. V. Braun, "Patterned Colloid Assembly by Grafted Photochromic Polymer Layers", Langmuir **22**, 1379–1382 (2006) (Cited on pages 109, 110, 124).

[198] N. S. Bell and M. Piech, "Photophysical Effects between Spirobenzopyran-Methyl Methacrylate-Functionalized Colloidal Particles", Langmuir **22**, 1420–1427 (2006) (Cited on pages 109, 124).

[199] M. C. George, A. Mohraz, M. Piech, N. S. Bell, J. A. Lewis, and P. V. Braun, "Direct Laser Writing of Photoresponsive Colloids for Microscale Patterning of 3D Porous Structures", Adv. Mater. **21**, 66–70 (2009) (Cited on pages 109, 110, 124, 125).

[200] Y. Shiraishi, K. Tanaka, E. Shirakawa, Y. Sugano, S. Ichikawa, S. Tanaka, and T. Hirai, "Light-Triggered Self-Assembly of Gold Nanoparticles Based on Photoisomerization of Spirothiopyran", Angew. Chem. Int. Ed. **52**, 8304–8308 (2013) (Cited on page 109).

[201] Z. Liu, T. Liu, Q. Lin, C. Bao, and L. Zhu, "Sequential Control over Thiol Click Chemistry by a Reversibly Photoactivated Thiol Mechanism of Spirothiopyran", Angew. Chem. Int. Ed. **54**, 174–178 (2015) (Cited on page 109).

[202] H. Zhang, F. Gao, X. Cao, Y. Li, Y. Xu, W. Weng, and R. Boulatov, "Mechanochromism and Mechanical-Force-Triggered Cross-Linking from a Single Reactive Moiety Incorporated into Polymer Chains", Angew. Chem. Int. Ed. **55**, 3040–3044 (2016) (Cited on page 109).

[203] H. Vijayamohanan, E. F. Palermo, and C. K. Ullal, "Spirothiopyran-Based Reversibly Saturable Photoresist", Chem. Mater. **29**, 4754–4760 (2017) (Cited on page 109).

[204]   S. O. Konorov, D. A. Sidorov-Biryukov, I. Bugar, D. Chorvat, D. Chorvat, and A. M. Zheltikov, "Quantum-Controlled Color: Chirp- and Polarization-Sensitive Two-Photon Photochromism of Spiropyrans in the Solid Phase", Chem. Phys. Lett. **381**, 572–578 (2003) (Cited on page 110).

[205]   K. Matczyszyn, J. Olesiak-Banska, K. Nakatani, P. Yu, N. A. Murugan, R. Zaleśny, A. Roztoczyńska, J. Bednarska, W. Bartkowiak, J. Kongsted, H. Ågren, and M. Samoć, "One- and Two-Photon Absorption of a Spiropyran–Merocyanine System: Experimental and Theoretical Studies", J. Phys. Chem. B **119**, 1515–1522 (2015) (Cited on page 110).

[206]   L. Lin, Z. Zhang, Z. Lu, Y. Guo, and M. Liu, "Two-Photon-Induced Isomerization of Spiropyran/Merocyanine at the Air/Water Interface Probed by Second Harmonic Generation", J. Phys. Chem. A **120**, 7859–7864 (2016) (Cited on page 110).

[207]   M.-Q. Zhu, G.-F. Zhang, C. Li, M. P. Aldred, E. Chang, R. A. Drezek, and A. D. Q. Li, "Reversible Two-Photon Photoswitching and Two-Photon Imaging of Immunofunctionalized Nanoparticles Targeted to Cancer Cells", J. Am. Chem. Soc. **133**, 365–372 (2011) (Cited on pages 110, 129).

[208]   P. Mueller, L. Hammer, R. Mueller, E. Blasco, C. Barner-Kowollik, and M. Wegener, "STED-Inspired Laser Lithography Based on Spirothiopyran Chromophores", in Conference on Lasers and Electro-Optics (2018) (May 13, 2018), SM4O.5 (Cited on pages 111, 121).

[209]   L. Hammer, "Spirothiopyrans as a Platform for Potential STED Lithography and the Formation of SCNPs", Master thesis (Karlsruhe Institute of Technology (KIT), Karlsruhe, 2017) (Cited on pages 112, 114, 115, 118).

[210]   C. Reichardt and T. Welton, eds., *Solvents and Solvent Effects in Organic Chemistry*, 4th Edition (Wiley-VCH, Weinheim, Germany, 2011) (Cited on pages 113, 114).

[211]   K. Herodes, I. Leito, I. Koppel, and M. Rosés, "Solute–Solvent and Solvent–Solvent Interactions in Binary Solvent Mixtures. Part 8. The ET(30) Polarity of Binary Mixtures of Formamides with Hydroxylic Solvents", J. Phys. Org. Chem. **12**, 109–115 (1999) (Cited on page 114).

[212]   J. M. Galvin and G. B. Schuster, "Preparation and Characterization of Mixed Thin Films Containing Spiropyrans and Long Chain Alkyl Silanes: Towards a Command Surface for Liquid Crystal Realignment", Supramol. Sci. **5**, 89–100 (1998) (Cited on page 117).

[213] R. Rosario, D. Gust, M. Hayes, F. Jahnke, J. Springer, and A. A. Garcia, "Photon-Modulated Wettability Changes on Spiropyran-Coated Surfaces", Langmuir **18**, 8062–8069 (2002) (Cited on page 117).

[214] R. Rosario, D. Gust, M. Hayes, J. Springer, and A. A. Garcia, "Solvatochromic Study of the Microenvironment of Surface-Bound Spiropyrans", Langmuir **19**, 8801–8806 (2003) (Cited on page 117).

[215] S.-i. Tamura, N. Asai, and J. Seto, "Photochromic Properties of a New Spirobenzothiopyran Compound", Bull. Chem. Soc. Jpn. **62**, 358–361 (1989) (Cited on pages 118, 130).

[216] V. A. Krongauz, "Quasi-Crystals", Isr. J. Chem. **18**, 304–311 (1979) (Cited on pages 124, 134).

[217] V. D. Arsenov, A. A. Parshutkin, V. S. Marevtsev, and M. I. Cherkashin, "Association of Photochromic 6-Nitroindolinospiropyrans in a Nonpolar Solvent", Bull. Acad. Sci. USSR **33**, 1799–1806 (1984) (Cited on page 124).

[218] V. D. Arsenov, V. S. Marevtsev, and M. I. Cherkashin, "Complexation of the Thermally Induced Colored Form of 6-Nitrospiropyrans in a Polar Solvent", Bull. Acad. Sci. USSR **33**, 1806–1809 (1984) (Cited on page 124).

[219] V. Krongauz, J. Kiwi, and M. Grätzel, "Laser Photolysis Studies of the Light-Induced Formation of Spiropyran—Merocyanine Complexes in Solution", J. Photochem. **13**, 89–97 (1980) (Cited on page 124).

[220] E. Goldburt, F. Shvartsman, S. Fishman, and V. Krongauz, "Intramolecular Interactions in Photochromic Spiropyran-Merocyanine Polymers", Macromolecules **17**, 1225–1230 (1984) (Cited on page 124).

[221] E. Goldburt, F. Shvartsman, and V. Krongauz, ""Zipper"Crystallization of Polymers with Spiropyran Side Groups", Macromolecules **17**, 1876–1878 (1984) (Cited on page 124).

[222] I. Cabrera and V. Krongauz, "Physical Cross-Linking of Mesomorphic Polymers Containing Spiropyran Groups", Macromolecules **20**, 2713–2717 (1987) (Cited on page 124).

[223] Y. Kalisky and D. J. Williams, "Laser Photolysis Studies of Photoinduced Aggregation in Polymers Containing Spiropyran Units", Macromolecules **17**, 292–296 (1984) (Cited on pages 124, 126, 137).

[224] A. V. Lyubimov, V. S. Marevtsev, V. D. Ermakova, and M. I. Cherkashin, "Photochromic Properties of 1,3,3-Trimethyl-6′-Nitrospiro (Indolino-2,2′-[2H-1] Benzothiopyran) in Polymeric Films", Bull. Acad. Sci. USSR **34**, 1380–1383 (1985) (Cited on pages 125, 130).

[225] R. S. Becker and J. Kolc, "Photochromism. Spectroscopy and Photochemistry of Pyran and Thiopyran Derivatives", J. Phys. Chem. **72**, 997–1001 (1968) (Cited on page 129).

[226] N. L. Zaichenko, A. V. Lyubimov, V. S. Marevtsev, and M. I. Cherkashin, "Inversion of Configuration in the Closed Form of Spirothiopyran Molecules", Bull. Acad. Sci. USSR **36**, 1543–1544 (1987) (Cited on page 129).

[227] H. Ito, "Chemical Amplification Resists for Microlithography", in *Microlithography · Molecular Imprinting*, Advances in Polymer Science 172 (Springer Berlin Heidelberg, 2005), pp. 37–245 (Cited on pages 143, 146).

[228] J. T. Fourkas and J. S. Petersen, "2-Colour Photolithography", Phys. Chem. Chem. Phys. **16**, 8731–8750 (2014) (Cited on page 147).

[229] K. Takada, H.-B. Sun, and S. Kawata, "Improved Spatial Resolution and Surface Roughness in Photopolymerization-Based Laser Nanowriting", Appl. Phys. Lett. **86**, 071122 (2005) (Cited on page 147).

[230] W.-E. Lu, X.-Z. Dong, W.-Q. Chen, Z.-S. Zhao, and X.-M. Duan, "Novel Photoinitiator with a Radical Quenching Moiety for Confining Radical Diffusion in Two- Photon Induced Photopolymerization", J. Mater. Chem. **21**, 5650–5659 (2011) (Cited on page 147).

[231] I. Sakellari, E. Kabouraki, D. Gray, V. Purlys, C. Fotakis, A. Pikulin, N. Bityurin, M. Vamvakaki, and M. Farsari, "Diffusion-Assisted High-Resolution Direct Femtosecond Laser Writing", ACS Nano **6**, 2302–2311 (2012) (Cited on pages 147, 148).

[232] I. Sakellari, X. Yin, M. L. Nesterov, K. Terzaki, A. Xomalis, and M. Farsari, "3D Chiral Plasmonic Metamaterials Fabricated by Direct Laser Writing: The Twisted Omega Particle", Adv. Opt. Mater. **5**, 1700200 (2017) (Cited on page 148).

[233] A. Van de Nes, L. Billy, S. Pereira, and J. Braat, "Calculation of the Vectorial Field Distribution in a Stratified Focal Region of a High Numerical Aperture Imaging System", Opt. Express **12**, 1281–1293 (2004) (Cited on pages 153, 154).

[234] B. Richards and E. Wolf, "Electromagnetic Diffraction in Optical Systems. II. Structure of the Image Field in an Aplanatic System", Proc. Math. Phys. Eng. Sci. **253**, 358–379 (1959) (Cited on page 153).

[235] R. Li, T. Nakashima, R. Kanazawa, O. Galangau, and T. Kawai, "Efficient Self-Contained Photoacid Generator System Based on Photochromic Terarylenes", Chem. Eur. J. **22**, 16250–16257 (2016) (Cited on page 157).

[236] R. Li, T. Nakashima, and T. Kawai, "A Self-Contained Photoacid Generator for Super Acid Based on Photochromic Terarylene", Chem. Commun. **53**, 4339–4341 (2017) (Cited on pages 157, 158).

Acknowledgments